High-Precision Abundance Study for the Milky Way Halo Stars with Kinematics and Asteroseismology

Tadafumi Matsuno

January 6, 2020

Abstract

Galaxy mergers play a significant role in galaxy formation. The Milky Way is a special galaxy for which we are able to observe individual stars in the stellar halo, fossil records of the mergers. Recent advents of space missions enabled us to dig into farther stars from us with stellar kinematics from astrometry and stellar masses from asteroseismology. This thesis demonstrates the effectiveness of the combination of chemical abundances, which are obtained from ground-based high-resolution stellar spectroscopy, with kinematics and asteroseismology to extract information about the merging history from halo stars. I verify that results from asteroseismic measurements can be consistently interpreted in classical framework of galaxy evolution, and can be used to constrain formation time of halo stellar populations when combined with chemical abundances. I also show that chemical abundances provide robust evidence that a kinematically identified stellar population is a signature of a past galaxy accretion. The results obtained in this thesis navigate future large spectroscopic surveys in the era with new satellite missions.

Executive summary

Stars record galaxy formation processes in their chemical abundance, kinematics, and age. The Milky Way is the only disk galaxy in which we can measure all these quantities for individual stars. The Galactic archaeology aims to reconstruct the formation history of the Milky Way to understand galaxy formation processes in general by studying its stellar contents.

While precise measurements of stellar kinematics and stellar ages have been limited to the solar neighbourhood until recently, space missions are revolutionizing this situation. The Gaia mission is measuring positions of stars with high precision, providing distance and proper motion over a large volume. These provide velocities of stars in the three-dimensional space with a help of radial velocity measurements by spectroscopy. This information enables us to search for signatures of past galaxy accretions.

Recent long-term photometric monitoring of stars by the space missions, *Kepler* or *CoRoT*, enables us to obtain power spectra of stellar oscillations. Since stellar oscillations depend on stellar structure, fundamental information about stars, such as stellar mass or evolutionary status, can be extracted from oscillation frequencies. This approach is called asteroseismology. Asteroseismology with data from the space missions provides mass estimates for a large number of red giants, which are otherwise almost inaccessible. From these mass estimates, stellar ages have been estimated for a large number of stars beyond the Solar neighbourhood for the first time.

Thanks to the novel observational data from the space missions and ground-based large spectroscopic surveys of stars, new stellar populations are revealed. Some of them seem to challenge our understanding of the galaxy formation, and others might provide new insights about the Milky Way formation history. The detailed property of the newly identified populations needs to be investigated in either case. Chemical abundance allows us further investigations since it should reflect the past star formation in the population and sometimes contains information about the evolution of the observed stars.

Chemical abundances are usually measured from high-resolution spectra obtained with ground-based telescopes. Efforts to measure chemical abundances of individual stars in the past decades have accumulated data for a large sample of Milky Way stars. Through such studies, the power of high-precision abundances is being recognized. One way to achieve high-precision in abundance analysis is to focus on relative abundance between stars with similar spectral types. In the analysis of high quality spectra, the largest source of uncertainties is stellar model atmospheres and atomic data. Since these affect abundances similarly between stars with similar spectral types, the relative abundance difference between them can be measured with high precision without being affected by model atmospheres or atomic data.

In this thesis, I report on observational studies about the Milky Way

halo stellar populations and the Milky Way formation history by combining precise stellar chemical abundances with kinematics and asteroseismology, which become available very recently. Previous studies have revealed two major halo populations with different α-element abundances, low-α and high-α populations. The low-α population is now considered to be an accreted dwarf galaxy, Gaia Enceladus. Although the two populations are well characterized in the solar neighbourhood, we aim to explore their properties beyond the solar neighbourhood. In addition, we aim to study recently identified halo stellar populations besides the two major ones. These studies constrain past galaxy mergers that have shaped the Milky Way.

This thesis starts by confirming our standard understanding about the chemical evolution and the asteroseismology. Recent combination of asteroseismology and chemical abundances identifies a peculiar stellar population having a high [α/Fe] ratio and relatively high mass, called "young α-rich stars". Existence of these stars is not expected in standard chemical evolution models. We obtained high-precision abundances of multi-elements, including neutron capture elements, for 14 young α-rich stars. We show that they have abundance patterns similar to typical old α-rich stars in almost all the elements studied. Comparison of our radial velocities with previous measurements confirms the high fraction of young α-rich stars showing radial velocity variation. The lack of abundance anomaly and the presence of radial velocity variation support the hypothesis that these stars are indeed a part of the old stellar population in the Galactic disk but gained mass as a result of binary interaction. This work demonstrates the validity of the standard framework of chemical evolution and asteroseismology. It also shows the ability of high-precision abundance in constraining the origin of peculiar stellar populations.

With this confirmation of our understanding of the chemical evolution, this thesis then moves on to the interpretation of chemical abundances of a halo stellar population. Analyses of stellar kinematics using the recent Gaia data pointed out an excess of stars on highly retrograde orbit with high orbital energy (high-E retrograde halo). While previous studies suggested its relation to Gaia Enceladus (or the low-α halo population) or to the globular cluster ω Centauri, it could be independent from both of them. We select candidate member stars of this high-E retrograde halo from a database of chemical abundances to investigate its chemical property. We suggest that the member candidates of the high-E retrograde halo have low Na, Mg, and Ca abundances than stars belonging to Gaia Enceladus. In addition, the high-E retrograde halo stars do not show Ba abundance anomalies, such as those seen in ω Centauri. These results indicate that the high-E retrograde halo is caused by an accretion event that is independent from Gaia Enceladus or ω Centauri. Moreover, lower α-element abundances indicate that the progenitor galaxy experienced slower star formation and hence had lower mass than Gaia Enceladus.

The final part of this thesis adds another type of information, stellar mass and age from asteroseismology, into the analysis. We attempt to constrain formation of the two major halo populations by combining all of stellar chemical abundances, kinematics, and stellar age (mass) for red giants. This was made possible by the *Kepler* observation and large spectroscopic surveys and is the first attempt of such studies for a large number of halo red giant stars beyond the solar neighbourhood. We study 26 halo stars for this purpose. Since halo stars are metal-poor, we first investigate the reliability of asteroseismology at low-metallicity, which has been debated in previous studies. We find that mass of our program stars is systematically over-estimated despite the use of theoretical correction in a scaling relation of asteroseismology. Although there is a systematic offset, masses of less evolved giants seem consistently measured in terms of a relative scale. There is no significant scatter in the measured masses among 15 less evolved stars with an upper limit of mass dispersion of $0.05\,M_{\odot}$. This provides a constraint on the timescale of star formation as $\lesssim 2\,$Gyr for the entire stellar halo.

Precise chemical abundance of the program stars enables us to separate our sample into low-α and high-α halo stellar populations. These two populations show chemical abundance differences consistent with previous studies of nearby halo turn-off stars. The chemical abundances indicate that the low-α population formed within a timescale of $100 - 300\,$Myr while the high-α population has even shorter timescale. Asteroseismology additionally constrains their age difference as $< 4\,$Gyr, indicating their formation epochs are not very different.

In summary, we obtained the following results by combining three stellar properties, that is, stellar chemical abundances, kinematics, and asteroseismology: i) we confirm the binary origin of the so-called young α-rich stars whose existence is unexpected in standard chemical evolution. This result ensures our current understanding of chemical evolution. ii) There was a galaxy accretion event that was independent from Gaia-Enceladus or from ω Centauri. It has highly retrograde orbit with high orbital energy and very low α-element abundances. The abundance indicates its long star formation timescale, indicating its low mass. iii) Asteroseismology opens a new window to investigate relative age difference or dispersion among halo stars beyond the solar neighbourhood. The halo high-α and low-α stellar populations have short star formation timescales with the low-α having longer timescale than the other. Their formation epochs are shown to be not significantly different.

These three results demonstrate that the combination of precise chemical abundances with stellar kinematics and ages is a powerful approach to reveal the nature of stellar populations in the Milky Way halo, and ultimately constrains the Milky Way formation history.

Acknowledgements

I would like to thank Wako Aoki for supervising me and for his patience over the last five years. I learned so many things from Wako, not only about abundance analysis but also about the way I should do science. I am sure that things I learned from Wako remain to be the basis throughout my career as an astronomer. Without your supervising, the way to here would have been much harder.

My gratitude also goes to my co-supervisors, Takuji Tsujimoto, Yutaka Komiyama and Nobuo Arimoto. All of you provided me with opportunities to broaden my scientific background. I would also like to thank Toshikazu Shigeyama for supervising me over my undergraduate project and for introducing Wako to me.

Many thanks to the collaborators. It is impossible to list all the people I collaborated with, but I have been working closely with Miho N. Ishigaki, Takuma Suda, Haining Li, Zhao Gang, and David Yong. Working with you has always been exciting experience. I thank David Yong, Luca Casagrande and Evan Kirby for kindly hosting my visits. The opportunities I had with you are full of lessons, which are necessary for me to complete this thesis.

Thesis reviewing committee provides me with comments, which helps to improve the manuscript. I especially thank Yoichi Takeda for his detailed review.

Among all the kind and friendly people who I met while travelling, I would like to particularly thank Thomas Nordlander and Aldo Mura, with whom I enjoyed my stay in Canberra. The three months in Canberra in 2017 was my first time to spend more than a few weeks outside of Japan. I was barely able to speak English and was very nervous at the beginning of the stay. You made me feel relaxed through drinks and jokes. The success of my visits was thanks to you.

I am most fortunate that I am blessed with friends. Not only I enjoyed talking with friends in NAOJ over science, there has always been a fun in my Ph.D. daily life thanks to you. My thanks also goes to those whom I enjoyed playing soccer with in NAOJ, Mount Stromlo, and Caltech. I am grateful to old friends and teachers from astronomy clubs in the high school and in the university, where I found my passion for astronomy. I have started studying astronomy thanks to the nights when we went out together

for stargazing. Special thanks goes to Satoshi Kikuta. We have shared time in the astronomy club in the university and later in the office in NAOJ as Ph.D. students. I have full of good memories with you about science and about other fun things.

I am thankful to all the people who work for NAOJ as secretaries. In particular, Subaru secretaries have always provided me with generous supports and sometimes cleaned up my mistakes in paper works.

This thesis contains data taken with Subaru and Keck telescopes. I appreciate supports from support astronomers, telescope operators, and all the people who work at the telescopes. They supported my observations with their detailed knowledge about the telescopes and instruments.

I am most fortunate to take data with telescopes on Mauna Kea. I recognize the role of the mountain among the indigenous culture and appreciate the understandings of indigenous people.

I have financially been supported by NAOJ, Sokendai, and JSPS. NAOJ provided me with a research fund each year and Sokendai supported my travels abroad. I have been supported by Grant-in-Aid for JSPS Fellows (Grant number 18J11326). I acknowledge that NAOJ and Sokendai also provide me with the research environment for my Ph.D..

I would like to express my gratitude to my parents, sister, and grand parents, who have been supportive to my decision to pursue Ph.D. I appreciate the opportunities my parents have offered to me to pursue my dream.

At last but not least, thank you to my wife, Tomoko, for her continuous supports and love. Even though we both are astronomers, you give me so much laugh and happiness outside of work. I am not sure if you have noticed it by yourself, but you have always cheered me up. Thank you.

Contents

Chapter 1

Introduction

1.1 From the Big Bang to galaxy mergers

In this section, I review the evolutionary path from the birth of the Universe to formation of galaxies. The contents of this section is a basis for researches in the field of Galactic archaeology. Although they might not be directly related to the specific research topics that I deal with later in this thesis, having these knowledge is necessary to put our researches in the context of the evolution of the Universe.

1.1.1 Big Bang

Evidence of expansion Universe (Slipher, 1917; Hubble, 1929) lead to the idea of the Big Bang as the beginning of the Universe (Lemaître, 1927, 1931). Alpher et al. (1948) explored nucleosynthesis under the very hot and dense environment shortly after the Big Bang. Cosmic microwave background (CMB) radiation was naturally predicted as a relic of this "fire ball" (Alpher & Herman, 1948). This is the beginning of the concept of the Big Bang nucleosynthesis (BBN).

Standard BBN models predict the primordial abundance with well-accepted particle physics, cosmology, and general relativity, under assumption of an isotropic and homogeneous Universe. Here we summarize standard BBN (Fields, 2011; Cyburt et al., 2016; Fields et al., 2019). When the Universe cools down to $T \sim 1\,\mathrm{MeV}$, weak interactions become slower than the speed of the expansion of the Universe, and thus neutron-to-proton ratio becomes fixed. Until it cools to $T \sim 0.07\,\mathrm{MeV}$, deuterium production via $p(n,\gamma)d$ is suppressed due to the black-body radiation of the Universe. Once this reaction starts, subsequent reactions, such as $d(p,\gamma)^3\mathrm{He}$, $d(d,\gamma)^4\mathrm{He}$, start to operate. In standard BBN models, only D, ^{3}He, ^{4}He, and ^{7}Li are produced with significant amounts (Wagoner et al., 1967) and baryon-to-photon ratio η is the only free parameter to determine the resultant primordial abundance (see Figure 2 of Fields et al., 2019).

Observations of these light elements' abundance have been providing a constraint on η and BBN models (Schramm & Turner, 1998). To avoid effects of chemical evolution, we have to measure their abundances from the environment as primordial as possible. The observed values are, then, extrapolated to zero-metallicity. Deuterium abundance is precisely determined from distant metal-poor absorption systems in the line of sight toward quasars (Adams, 1976; Burles & Tytler, 1998a,b; Balashev et al., 2016; Cooke et al., 2014, 2016; Riemer-Sørensen et al., 2015, 2017; Cooke et al., 2018; Zavarygin et al., 2018). ^{4}He abundance is determined from emission lines of nearby metal-poor galaxies (Peimbert & Torres-Peimbert, 1974; Kunth, 1981; Izotov et al., 2014; Aver et al., 2015; Peimbert et al., 2016; Fernández et al., 2018, 2019; Valerdi et al., 2019), though the determination has suffered from large uncertainties due to many free parameters (Olive & Skillman, 2004; Izotov et al., 2007; Peimbert et al., 2007). ^{7}Li abundance is determined from metal-poor stars in the Local Universe (Spite & Spite, 1982a,b; Meléndez et al., 2010), though the interpretation has been debated (Michaud et al., 1984; Ryan et al., 1999; Piau et al., 2006; Fields, 2011; Fu et al., 2015; Takeda, 2019). Matsuno et al. (2017a,b) discuss the Li problems, although they are not included in this thesis.

Precise CMB anisotropy measurements have provided another way to estimate η. Coc et al. (2002) pointed out that, once CMB measurements by BOOMERANG, DASI and MAXIMA are taken into account, observed abundances of Li and D are only marginally consistent. After higher precision CMB measurements by Wilkinson Microwave Anisotropy Probe and Planck observations (Spergel et al., 2003; Planck Collaboration et al., 2016), it has been realized that D and ^{4}He abundances are consistent with η estimates from CMB measurements. On the other hand, the observed ^{7}Li abundance is lower than the prediction from CMB measurements, which has been known as Li problem. Solution to this problem has been investigated from the point of star formation (Piau et al., 2006), stellar evolution (Michaud et al., 1984; Richard et al., 2005; Fu et al., 2015), and abundance measurements (Takeda, 2019). The most recent estimates based on the recent CMB observations by the *Planck* and reaction rates are provided by Fields et al. (2019).

1.1.2 First stars

After the first nucleosynthesis, the Universe keeps cooling and density fluctuation keeps growing. The next event we consider is birth and death of first stars.

Formation of first stars can be summarized as follows (Bromm, 2013). Once an overdense region becomes more massive than a certain critical mass (Jeans mass) above which the cooling time is shorter than the dynamical time, it can collapse to form a star. This occurs in $2-3\sigma$ overdense regions at

$z \sim 20-30$ having typical mass of $\sim 10^6\,\mathrm{M}_\odot$, called mini-halo. In the absence of any metal (elements heavier than helium) in the Universe, cooling by hydrogen molecules helps further contraction until hydrostatic core emerges. Although the mass of the initial hydrostatic core is almost the same as in current star formation, protostellar accretion rate is believed to be much higher than that in the present Universe due to higher temperature, which is a result of higher CMB temperature and absence of metals. Therefore, the resultant initial mass function (IMF) differs significantly from today.

IMF of first stars is expected to be top-heavy compared to the present day IMF. Three-dimensional simulations of first stars formation have shown that the typical mass of the central star is a few tens to a few hundreds of solar masses (e.g., Stacy et al., 2016; Susa et al., 2014; Hirano et al., 2014; Hosokawa et al., 2016; Greif et al., 2011; Stacy & Bromm, 2013). As a result of an investigation of 100 star forming clouds in the 2D simulation (Hirano et al., 2014), the mass of the first star at the center of the primordial star forming clouds is typically a few $\times 10\,\mathrm{M}_\odot$ with the minimum mass of $\sim 10\,\mathrm{M}_\odot$, while some might exceed $10^3\,\mathrm{M}_\odot$. Fragmentation in circumstellar disks complicate the mass spectrum since the fragments can be as low mass as $< 1\,\mathrm{M}_\odot$ and might survive without merging to the primary star (Clark et al., 2011a,b; Turk et al., 2009). The nature and the consequence of the fragmentation have been investigated in recent years (e.g., Susa, 2019; Hirano & Bromm, 2017; Stacy et al., 2016).

In any cases, it is clear that the peak of the mass function of first stars is located around a few $\times 10 M_\odot$. These massive stars end their lives with supernova explosion ejecting significant amounts of metals. These first metals have changed star formation (Section 1.1.3).

Another important aspect of the first stars is that they could have been rotating fast (Stacy et al., 2011, 2013; Hirano & Bromm, 2018). Rapid rotation should change the structure of the stars and properties of supernova explosions, which result in changes in nucleosynthesis (Takahashi et al., 2014; Maeder et al., 2015).

Direct observations of first stars are still difficult. Future observations with next generation telescopes, such as ELTs or James Webb Space Telescope, may be able to capture their light from the distant Universe. Low-mass metal-free stars have not yet been found so far, though this fact itself is a constraint on the mass function of first stars at low-mass end (Ishiyama et al., 2016; Magg et al., 2019).

Chemical abundances of second generation stars, which are observed as metal-poor stars, have been one of the important tools to study the nature of first stars. Assuming chemical abundance of second generation stars reflect nucleosynthesis by first stars, Ishigaki et al. (2018) and Choplin et al. (2019), respectively, explored mass and rotation velocity distribution of first stars from chemical abundance of extremely metal-poor stars. Most of the abundances of metal-poor stars have been explained by mixing and

fallback model of supernova explosions of first stars (Umeda & Nomoto, 2003; Iwamoto et al., 2005; Nomoto et al., 2013; Tominaga et al., 2014) or by nucleosynthesis in rapidly rotating first stars (Maeder et al., 2015). Although different models reach different conclusion, Takahashi et al. (2014) incorporate rapid rotation in the mixing and fallback model. They showed that abundance patterns of extremely metal-poor stars are explained by the yield from a few $\times 10\,\mathrm{M}_\odot$ first stars. The discovery of the signature of very massive first stars ($> 100\,\mathrm{M}_\odot$) could be another constraint on the mass function of the first stars (Aoki et al., 2014).

1.1.3 Formation and evolution of metal-poor stars

Supernovae of first stars provide with metals and blow out the surrounding gas. Second generation stars are formed under this environment. Since the metal content in the Universe is still small, the second generation stars are extremely metal-poor. At this time, the halo has grown to $\sim 10^8\,\mathrm{M}_\odot$, which is called as atomic cooling halo since its virial temperature is higher than $\sim 10^4\,\mathrm{K}$.

The most important change from first stars formation to second-generation stars formation would be the change in IMF. Because of the presence of metals, gas is now possible to fragment into small pieces. IMF of metal-poor stars is believed to be more like present day, i.e., bottom heavy. Therefore a number of low mass stars which can survive over 13 Gyr are formed.

Two paths are suggested for the formation of second generation stars, and each has a critical metallicity. One is efficient cooling thanks to fine structure lines of C II and O I. Motivated by the fact that most of ultra iron-poor stars [Fe/H] < -4.0 [1] have enhanced carbon abundance, Frebel et al. (2007) suggested $D_{\mathrm{trans}} \equiv \log(10^{[\mathrm{C/H}]} + 0.3 \times 10^{[\mathrm{O/H}]})$ should be larger than $D_{\mathrm{trans,crit}} \simeq -3.5$. Indeed, most of the metal-poor stars with [Fe/H] < -4.0 satisfy this criterion. This can be understood as second generation stars start to form from the region where $D_{\mathrm{trans}} > D_{\mathrm{trans,crit}}$ and as some regions have high carbon abundance compared to iron due to an unique yield from a first star (Iwamoto et al., 2005; Maeder et al., 2015).

However, there are stars which do not satisfy the criterion. After the discovery of an ultra metal-poor star with normal carbon abundance, SDSS J102915+172927 (Caffau et al., 2011), formation of second generation stars

[1] Throughout this paper, following traditional expressions are used for chemical abundances

$$\log \epsilon(X) \equiv \log(N_{\mathrm{X}}/N_{\mathrm{H}}) + 12 \tag{1.1}$$

$$[\mathrm{X/Y}] \equiv \log(N_{\mathrm{X}}/N_{\mathrm{Y}}) - \log(N_{\mathrm{X}}/N_{\mathrm{Y}})_{\mathrm{Sun}}, \tag{1.2}$$

where N_{X} is the number density of the element X. Since elemental abundances are often described in [X/Y], i.e., relative to the Sun, the solar abundance is important. We adopt photospheric abundance of Asplund et al. (2009) for the solar chemical abundance.

via dust cooling has been regarded as an important path (Klessen et al., 2012; Schneider et al., 2012b). Dust in this model is assumed to be formed in supernova remnants of first stars. Although the critical metallicity depends on the size distribution of the dust (Schneider et al., 2012a), dust cooling can account for the formation of stars which can not be explained via fine structure cooling (Ji et al., 2014). Different modes of star formation among second generation stars are also discussed in Chiaki et al. (2017) from the point of the dust grain size.

Since the second generation stars formed in the very early Universe, only those less massive than $\sim 0.8\,\mathrm{M}_{\odot}$ can survive until now. Surviving low mass stars are now observed as extremely metal-poor stars in the Local Universe.

1.1.4 Formation and merging of galaxies

First galaxies start to form after the formation of first stars once dark matter halos can sustain ionized gas in their potential. Galaxies continue to evolve under the influence of feedback from the massive first stars and eventually re-ionize the Universe. The Universe starts to show more complexity from this epoch due to various feedback processes such as energy injection by supernova explosions, strong ionizing radiation from massive stars, or radiation and outflows from active galactic nuclei. Galaxies start to differ significantly depending on the mass or the environments.

Galaxy-mergers play a significant role in the subsequent galaxy evolution in the Λ CDM (cold dark matter) model. Dark matter halos grow in their mass through mergers, and the baryonic content of galaxies also increases accordingly. Dark matter halos of Milky Way-mass galaxies on average increase their mass by a factor of 2 from $z \sim 1.5$ to 0 and by a factor of 10 from $z \sim 4$ (e.g., van den Bosch, 2002; Rodriguez-Gomez et al., 2016; Stewart et al., 2008). However, there is a diversity in mass assembly history even among galaxies with similar mass. As we see below, since galaxy evolution heavily depends on the properties of merging processes, understanding the merging history is the key to understand the evolution of a galaxy.

When two galaxies with comparable masses merge, the merger is called major merger. These major mergers cause drastic changes to the galaxies. Structures of the progenitor galaxies are disrupted because of the strong interaction between them, leaving an elliptical galaxy as the product (Toomre & Toomre, 1972). If the progenitors contain significant amount of gas, the gas is feed into the central part triggering starburst and activity of the central black hole (e.g., Noguchi, 1988; Mihos & Hernquist, 1996; Di Matteo et al., 2005). These major mergers are frequently seen at high redshift (e.g., Gottlöber et al., 2001; Lotz et al., 2011).

If one of the merging galaxies is significantly smaller than the other, the merger is called minor merger, which happens more frequently than major mergers. Structures of the larger central galaxy basically remains un-

changed, although they might be perturbed (e.g., Laporte et al., 2018). On the other hand, the smaller satellite galaxy gets disrupted as it approaches to and orbits around the central galaxy. Firstly the gas of the satellite is removed due to the central galaxy probably because of ram pressure stripping (Wetzel et al., 2015; Emerick et al., 2016). Additionally, its stellar and dark matter components suffer from tidal force from the central if the satellite is large and it comes close to the central. This tidal force also removes kinetic energy of the satellite, making it sink in the potential of the central galaxy. These mergers are often referred to as accretion of a satellite galaxy to the central.

The signature of minor mergers can be observed even after the merging process. Tidally-stripped stars form stellar streams for a while, which can be found in photometric observations of galaxies (e.g., Ibata et al., 1994; Belokurov et al., 2006; Grillmair, 2006; Bernard et al., 2016). Although spatial signatures of the merger could be too diffuse to be detected as time passes, kinematic signatures remain for a much longer time scale since stripped stars experience little dynamically interactions with objects other than the central galaxy (see next section). The merging history of a galaxy can be constrained by studying these signatures. Since there should be no preferred direction in these accretion processes in the Λ CDM model, these minor mergers make up a diffuse spheroidal component of stars around galaxies (stellar halo), which can extend up to $\gtrsim 100\,\mathrm{kpc}$.

Unless galaxies strongly interact with others, the gas component looses its kinematic energy due to the viscosity and forms a disk preserving the initial angular momentum. Stars continuously form from this gas, which makes up the stellar disk. The star formation in the gaseous disk is self-regulating, and hence the star formation rate shows a tight correlation with gas surface density of the galaxy (Kennicutt–Schmidt law Schmidt, 1959; Kennicutt, 1998). Normal disk galaxies are considered to be in this phase.

Disk galaxies are more or less axisymmetric. However, more than half of disk galaxies possess a bar in the central part because of, e.g., the instability of the disk (e.g., Sheth et al., 2008; Nair & Abraham, 2010). The presence of the bar then breaks the axisymmetry and enables resonance orbits. Kinematics of stars and gas, and hence star formation or stellar populations in the galaxy, could be affected by the bar. These bars are sometimes referred to as "pseudo-bulge", since they could look spherical. Disentangling the pseudo-bulge, which is a result of secular evolution, and the bulge, which is a product of major mergers in the past, is of great importance to understand the merging history of a galaxy.

In summary, galaxies are shaped depending on the past mergers. Understanding the merging history for a galaxy is a key to understand the formation and the evolution of the galaxy. Cosmological models could be tested through a statistical comparison of the prediction with merging histories of galaxies inferred from observations.

1.2 Galactic Archaeology

Galactic archaeology is a field of research in which astronomers study nearby galaxies instead of high-redshift universe trying to understand the history of the Universe. Although the definition of nearby universe varies depending on the context, galactic archaeologists usually observe galaxies for which we can resolve individual stars. Much effort has been particularly devoted for stars in and around the Milky Way.

In this section, I explain the importance of the Milky Way by describing the information available from observations of stars. There are several types of information, but its combination over a wide volume has been limited until recently.

I then review the current understandings of the formation of the Milky Way with a special focus on its merging history in order to put following chapters in the context. This chapter also includes questions that will be answered in the rest of the thesis. These questions are highlighted in the text and discussed in detail later in this thesis.

1.2.1 Why do we study Milky Way?

The study of the Milky Way has two aspects; we aim to understand both properties that is common as other galaxies and that is unique to the Milky Way.

Since a large portion of galaxies in the current Universe are disk galaxies (e.g., Conselice, 2014), it is of a great importance to understand their formation histories. The Milky Way is a typical disk galaxy in many aspects in the local low-density environment (e.g., mass, star formation rate, or baryon fraction; Bland-Hawthorn & Gerhard, 2016). At the same time, the Milky Way is special because we live inside of it. Since every object in the Galaxy is much closer to the Earth than any objects outside of it, we can carry out deepest observations for its components with the highest spatial resolution. As we see throughout this thesis, individual stars contain rich information about the history of the Galaxy.

The Milky Way is also special in some aspects. For example, the Milky Way has two satellite galaxies, large and small Magellanic clouds (LMC and SMC), which are star-forming and massive for satellite galaxies. Only 3.5% of Milky Way analogs host two satellites similar to Magellanic clouds (Liu et al., 2011). Understanding the peculiarities of the Milky Way is necessary in order to put the Galaxy in the context of galaxy formation in general. Besides scientific aspects, since humans have been trying to understand the environment in which we live, it is natural for us humans to try to understand the specific property of the Milky Way.

Although the Milky Way provides an unique opportunity, there are difficulties in observations of the Galaxy that are not present when we observe

other galaxies. They are mainly caused by the fact that we are unable to look at it from outside, which makes it harder for us to depict the global property of the Milky Way, such as morphology or its mass. In order to investigate the global property, we need to capture three-dimensional distribution of objects, which is not trivial since measurements of distance require very precise astrometry. A recent revolutionary progress in distance measurements is made by the Gaia mission (Gaia Collaboration et al., 2016a). Recent findings that Gaia has made possible are included in this section.

1.2.2 Observation of stars

Stars serve as relics of the Galaxy formation. Information about the history of the Galaxy is recorded in stellar kinematics, chemical composition, and ages. I briefly review what kind of information each property retains.

kinematics

Kinematics of stars have information about their birth place. Since dynamical interactions between stars are usually negligible in the Galaxy [2], orbits of stars are predominantly determined by the gravitational potential of the Galaxy. In such a condition, motion of stars inside the Galaxy can be traced back with the equation of motion.

One of the most important pieces of information we can get from stellar kinematics is the accretion history of the Milky Way. Signatures of past galaxy accretions can be searched for from stellar kinematics (e.g., Helmi et al., 1999; Smith et al., 2009; Klement et al., 2009; Helmi et al., 2017; Myeong et al., 2018a). Stars accreted from the same galaxy have almost the same initial condition, i.e., almost the same velocity and position relative to the Galactic center. If the accretion occurred quite recently, they show a clustering in the spatial distribution (e.g., Ibata et al., 1994; Belokurov et al., 2006; Grillmair, 2006; Bernard et al., 2016). However, if we try to find ancient accretion signatures or if we look for accretion signatures in the inner Galaxy like solar neighbourhood, we need to investigate spaces of integrals of motion. As the integrals of motion are constants along an orbit[3], those of stars from the same galaxy remain almost the same. Therefore, accretion signatures appear as over-densities in the space of stellar kinematics. Over-densities found from observational data are candidates of past accretion signatures and some times referred to as kinematic substructures.

If the Galactic potential is static and spherical, there are four integrals: orbital energy and three components of the angular momentum. A more

[2]Typically gravitational radius GM/v^2 is $\lesssim 1\,\mathrm{au}$, which is much smaller than the distance between stars. Only exceptions are inside stellar clusters.

[3]An integral of motion has to be a function of position and velocity and must not include time in its expression.

realistic assumption is axisymmetry of the potential, in which case there are three integrals. Although two of them are orbital energy and angular momentum around the symmetric axis, no analytical form for the "third" integral has been known for general cases. In the Stäckel potential (see the next chapter), the third integral is known and some studies have estimated the integral approximating the Galactic potential with a Stäckel potential (Chiba & Beers, 2000). In some other cases, $L_\perp = \sqrt{L^2 - L_z^2}$, where L is the total angular momentum and L_z is the angular momentum around the symmetric axis, has been used as an approximate form of the third integral (e.g., Helmi et al., 1999).

In reality, the Galactic potential changes slowly with time and shows deviation from axisymmetry, e.g., due to the Galactic bar. In such cases, action variables are expected to be better places to search for accretion signatures, since action variables of stars remain unchanged under slow change of the gravitational potential. One of the action variables in the axisymmetric potential is the angular momentum around the symmetric axis, and thus easy to estimate. Other actions are usually calculated with the Stäckel approximation. Search for accretion signatures from action space has been conducted in Myeong et al. (2018b).

The origin of kinematic substructures is clarified through chemical abundances and/or ages. The metallicity spread of member stars reveals if the progenitor is a globular cluster or a dwarf galaxy. Once detailed abundance ratio is measured, kinematic substructures having different progenitor galaxies might be separated. This is important since different accreted galaxies can overlap in the space of kinematics and a single accretion can create multiple kinematic substructures in observational data (Gómez & Helmi, 2010; Jean-Baptiste et al., 2017). Information about the star formation history in the progenitor can also be discussed through chemical abundances as we see below. *In particular, kinematic substructures recently found from the Gaia data await the characterization by chemical abundances (Chapter 4).*

Chemical abundances

Chemical abundance of stars also tells us about the history of the Galaxy and gives independent information from stellar kinematics (e.g., Freeman & Bland-Hawthorn, 2002; Frebel & Norris, 2015). This is made possible by the fact that surface abundances of most of the elements are unchanged throughout the stellar evolution. Therefore, the chemical composition of, for example, a 10 Gyr old star is basically the same as the chemical composition of the Galaxy 10 Gyr ago. Since the Universe began with the Big Bang, which only produces limited light elements, all the other elements ("metal" in the astronomical context) are synthesized later directly or indirectly by stars. The chemical composition of the Galaxy reflects all the past star formation activities in the Galaxy, and hence stars retain information about

star formation prior to the formation of the star.

The amount of metals, called metallicity, is a fundamental parameter when we analyse stellar chemical abundances since it is roughly an age indicator. Metallicity is represented by the iron content of a star as [Fe/H]. Since the Universe started without metals, [Fe/H] was initially $-\infty$. Subsequent nucleosynthesis events produce metals including iron keeping [Fe/H] increasing. Therefore, metal-poor stars are generally older than metal-rich stars.

Although abundance of each element is roughly scaled to the iron abundance in most stars, detailed abundance ratios between different elements contain rich information about the past star formation activity because different types of astronomical events produce different elements with different timescales (see Appendix A for details). Let us assume that one type of astronomical events, A, starts to happen shortly after star formation with production of element X, and another type of event, B, that produces element Y needs much longer time until it starts to happen after star formation. In the earliest phase of galaxy evolution, chemical abundance is determined only by chemical yields of massive stars that can almost instantaneously enrich the galaxy with metals. If a system has bursty star formation for a short period, there would be no time for the event B to occur. Therefore, we expect high [X/Y] for stars formed in the system. To the contrary, a system with prolonged star formation history would have low [X/Y].

For example, the abundance ratio between α-elements and iron has been used as an indicator of star formation timescale. As we see below, the Milky Way disk has two components, thick and thin disks. The higher [α/Fe] of the thick disk is interpreted as a result of its shorter star formation timescale than the thin disk. In other words, the thick disk formed in bursty star formation, while thin disk formed through steady star formation. The α-element abundances are also used to identify stars having formed in satellite dwarf galaxies since the more massive Milky Way evolves with a shorter timescale and enriches faster.

Chemical abundances of stars are measured from spectra of stars. Molecules and atoms in stellar atmosphere absorb light that comes from deeper layers and change their energy state. The energy difference between the two states corresponds to the energy of the absorbed light. Absorption forms a spectral line if both states are bound, from which we measure chemical abundances. As we see in the next Chapter, the strengths of an absorption line depends on the abundance of the element in the stellar atmosphere, the structure of the atmosphere, and the property of the transition (e.g., transition probability, or excitation energy). Chemical abundances of stars are measured by incorporating models of stellar atmosphere and experimental data about the atom or the molecule. Stellar spectra are full of absorption lines, so high-resolution spectroscopy is applied to resolve individual lines and to determine abundances of many elements.

Combination of many elements is a key to obtain information about the galaxy evolution. As summarised in Appendix A, there are several nucleosynthesis processes/sites in the Universe. Multiple nucleosynthesis processes provide information about the chemical evolution over multiple dimensions. In addition, most of the elements are synthesized by more than one process (see Jennifer Johnson's astronomical periodic table[4]). Having many element abundances enables us to extract the information for a single nucleosynthesis process.

Ages

Stellar age is an important parameter in understanding the Milky Way formation history since it is the most direct estimate of the formation epoch of a star or that of the stellar population that the star belongs to.

Stellar ages for populations in the Galaxy constrain the formation epoch and/or the origin of the population. For example, stellar age is proposed to be the most fundamental and the best parameter for separating thin and thick disk stars (e.g., Bensby et al., 2014; Buder et al., 2019). The age gap between the two disks is suggested, which might indicate a presence of an event that has shaped the two disks, such as a major merger. The evolution of the Galactic disk, including radial migration, is also investigated using stellar ages (e.g., Casagrande et al., 2016; Anders et al., 2017; Silva Aguirre et al., 2018).

Stellar ages for halo stars also provide us with invaluable information. Since halo stars, including stars in globular clusters, are metal-poor, they are expected to be the oldest stars in the Milky Way. Before the advent of the precision observational cosmology by CMB observations, halo stars had been used to constrain the age of the Universe. These ages have been obtained through isochrone fitting for color-magnitude diagrams of globular clusters (Krauss & Chaboyer, 2003) or through abundances of radio active nuclei (Th and/or U; Cayrel et al., 2001).

Although precise age of the Universe can now be obtained from an alternative method, stellar ages still play an important role in understanding the formation of the Milky Way halo. Carollo et al. (2016) studied a large scale age structure and revealed an age gradient over a $\sim 100\,\mathrm{kpc}$ in the halo. This indicates that properties of accreted progenitor galaxies change as a function of Galactocentric distance. Another example is Schuster et al. (2012), who compared ages of the two halo stellar populations in the solar neighbourhood which were originally identified through stellar chemical abundances in Nissen & Schuster (2010). They revealed the age difference between the two components in particularly at the high metallicity end, providing a support for the interpretation that their chemical abundance difference is due to different star formation timescales.

[4] http://blog.sdss.org/2017/01/09/origin-of-the-elements-in-the-solar-system/

As we discussed, stellar ages contain rich information about stellar populations in the Milky Way. However, their estimates are not as easy as those of chemical abundances or stellar kinematics. The age estimates have been mostly limited to stars in the following evolutionary status (Soderblom, 2010).

- White dwarfs: White dwarfs continue to cool down after they formed. The temperature and luminosity are expected to depend on the age (e.g., Winget & Kepler, 2008; Salaris et al., 2009; Kilic et al., 2017, 2019).

- Blue horizontal branch (BHB) stars: These stars are evolved stars burning helium in the center. They are more luminous and bluer than main-sequence halo stars. Their color depends on metallicity and the mass, which provides age estimates (e.g., Preston et al., 1991; Santucci et al., 2015; Carollo et al., 2016; Das et al., 2016).

- Turn-off stars: Stars move across the color-magnitude diagram (CMD). In particular, when stars exhaust hydrogen in the core, they start to change temperature and luminosity dramatically. This makes a turn-off point in CMDs. Location of stars on the CMD is most sensitive to the age around the turn-off point. Comparison of the location with theoretical stellar evolutionary tracks gives age estimates for stars (e.g., Edvardsson et al., 1993; Bensby et al., 2014; Lin et al., 2018). Note that for red giant branch stars, stars with different masses (and hence ages) occupy a similar region, and hence this method does not provide precise age.

- Red giant branch stars: Since stars with a convective envelope, including red giant branch stars, oscillate depending on their internal structure, stellar fundamental properties including stellar mass are inferred by analysing the light-curves obtained by space missions (Asteroseismology; Aerts et al., 2010; Chaplin & Miglio, 2013). Once the mass of a red giant is obtained, it is straightforward to infer the age of the star since the time spent on the red giant branch is almost negligible compared to that on the main-sequence phase, which is predominantly determined by the stellar mass.

In this study we focus on mass or age estimates of red giant branch stars from asteroseismology since it has advantages over other methods. Abundance measurements for white dwarfs and BHB stars are technically limited because of their high surface temperature, which limits the combination of stellar ages and chemical abundance; turn-off stars and white dwarfs are faint, which limits our survey volume. On the other hand, red giants are intrinsically luminous and contain many absorption lines in their spectra, from which we can measure chemical abundances for many elements.

Asteroseismology is a relatively new field that started to be widely explored after the recent emergence of space missions that carried out long-term monitoring of luminosity variation of stars with high-precision, such as *Kepler* (Koch et al., 2010) and CoRoT (Auvergne et al., 2009). Mass of a large number of red giants are estimated from their light curves (Kallinger et al., 2010a,b; Hekker et al., 2011; Stello et al., 2013; Pinsonneault et al., 2014; Mathur et al., 2016; Yu et al., 2018; Pinsonneault et al., 2018), which is otherwise almost inaccessible (however see also Feuillet et al., 2016; Martig et al., 2016; Ness et al., 2016).

These stellar ages obtained through asteroseismology have revealed the evolution of the Galactic disk (e.g., Casagrande et al., 2016; Anders et al., 2017; Silva Aguirre et al., 2018). *However, several studies revealed the existence of an unexpected stellar population in the Galactic disk (Chiappini et al., 2015; Martig et al., 2015), whose chemical abundance is typical of old stars while whose mass from asteroseismology is massive indicating young age. The population challenges our current understandings of the galactic chemical evolution. Its property needs to be clarified. (Chapter 3)*

Although asteroseismology has been applied to stars in the Galactic disk, *application to low-metallicity halo stars has been limited. It is necessary to confirm the reliability of this approach for low metallicity stars. (Chapter 5)*

1.2.3 Current understandings of the Milky Way

In this section, I review the current understandings of the Milky Way. Covering several stellar populations that are found in disk galaxies, I provide discussions for each of the components. In total, the Milky Way contains $\sim 5 \times 10^{10}\,\mathrm{M}_\odot$ stellar mass and $\sim 1 \times 10^{12}\,\mathrm{M}_\odot$ dark matter mass within the virial radius.

The bulge contains $\sim 1.5 \times 10^{10}\,\mathrm{M}_\odot$ stellar mass. Observation of stars suggests that the bulge is dominated by a rotating bar (Binney et al., 1991; Blitz & Spergel, 1991). The contribution of a classical bulge component is minor, indicating galaxy mergers played little role in the formation of the Milky Way bulge (Kormendy & Kennicutt, 2004). Metal-poor stars in the bulge show weaker rotation signal, which might trace the very early phase of the Milky Way formation (Ness et al., 2013; Arentsen et al., 2020).

Most of the Milky Way stellar mass is in the disk with $\sim 3.5 \times 10^{10}\,\mathrm{M}_\odot$ and $6 \times 10^{9}\,\mathrm{M}_\odot$ in the thin and thick disk respectively. Thin disk has short scale height, longer scale length, younger age, higher metallicity, and lower [α/Fe] at a given [Fe/H] than the thick disk (see Figures 1.1 and 1.2). The [α/Fe] bimodality and the stellar age distribution suggest that thin and thick disk formation epochs are separated, which might indicate a presence of events that heated up stars to form thick disk, such as mergers (Villalobos & Helmi, 2008; Qu et al., 2011; Belokurov et al., 2018; Helmi et al., 2018), or that halted and changed star formation process (Noguchi, 2018). After the

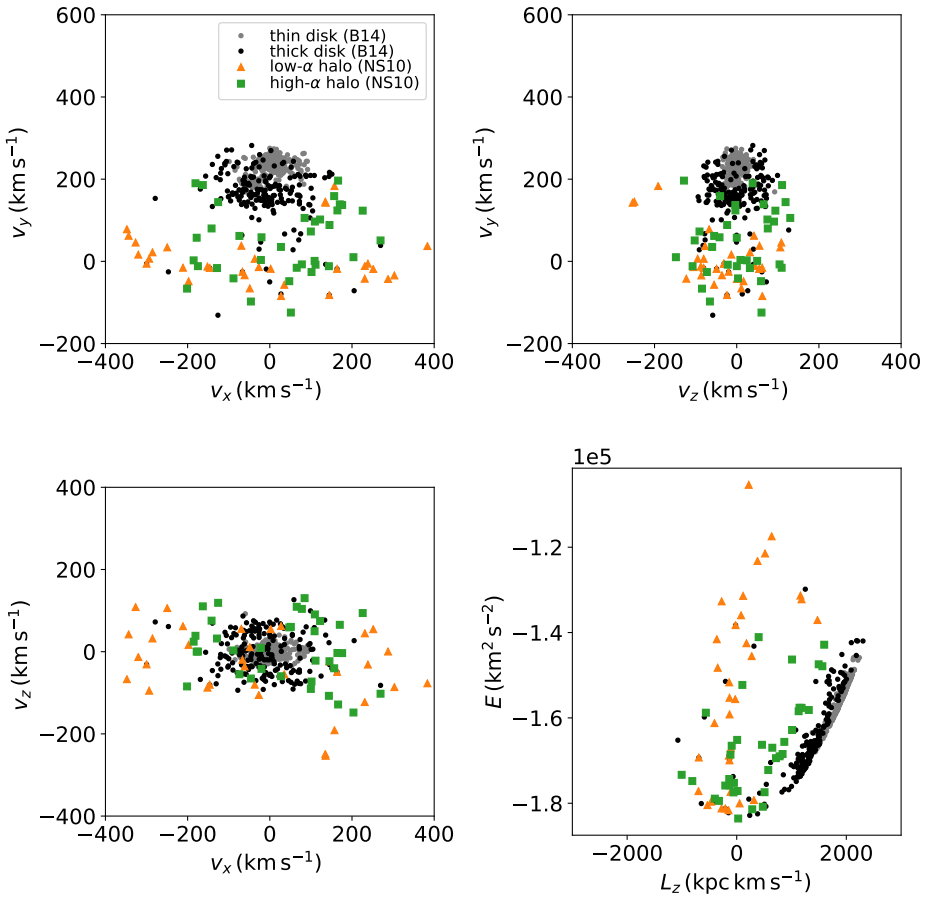

Figure 1.1 Velocities, angular momentum, and orbital energy of major populations in the solar neighbourhood. Data are from Bensby et al. (2014, B14) and Nissen & Schuster (2010, NS10). Note that v_x and v_y are positive toward the Galactic center and in the Galactic rotation direction, respectively.

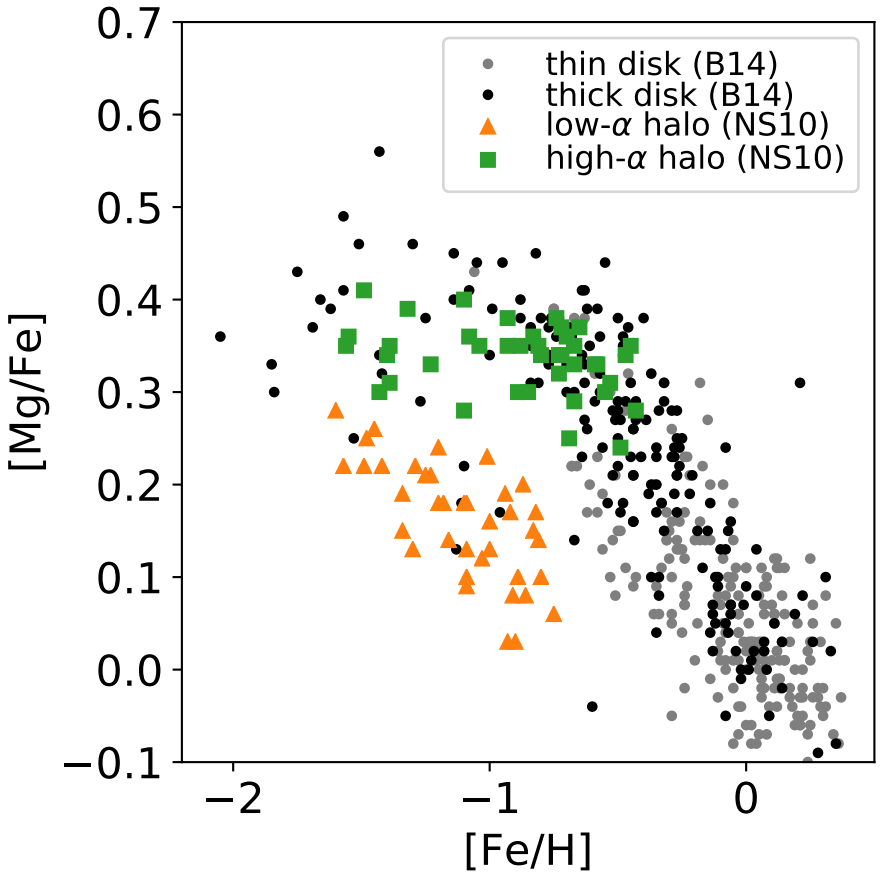

Figure 1.2 Same as Figure 1.1, but for Mg abundance.

thick disk formation, the Milky Way is considered to have had a quiescent accretion history since it currently has the thin disk. The last major merger is estimated to have occurred at $z \gtrsim 2$ (e.g., Kruijssen et al., 2018).

There is a signature of recent dynamical interactions with satellite galaxies in the disk. Several over-densities of stars in the sky are now shown to be composed of stars with similar properties to disk stars and considered to be a part of the Galactic disk (e.g., Momany et al., 2004; Li et al., 2017; Sheffield et al., 2018). Since they have offset from the Galactic plane, general interpretation is that the Galactic disk is perturbed. Simulations show that the Sagittarius dwarf spheroidal galaxy could be the cause of the perturbation (Laporte et al., 2018).

Previous studies also have suggested the existence of the metal-weak thick disk stars (Chiba & Beers, 2000; Carollo et al., 2019). While the metallicity distribution of thick disk peaks at [Fe/H]~ -0.6, metal-weak thick disk seems to extend down to at least [Fe/H]~ -1.7. In addition, recent studies indicate that many of the ultra metal-poor stars known to date show disk-like kinematics (Sestito et al., 2019). These stars are expected to be almost as old as the Galaxy, and would contain information about the very early phase of the Milky Way formation. The metal-weak disk or ultra metal-poor disk might be related to very early galaxy mergers in this Galaxy.

Although the halo is estimated to contain only $\sim 5 \times 10^8\,M_\odot$ stellar mass, it provides rich information about the merging history. Stellar streams in outer halos have been observed, some of which are considered to have been formed by accretion of a galaxy [5] (e.g., Ibata et al., 1994; Belokurov et al., 2006; Grillmair, 2006; Bernard et al., 2016). Among these streams, the most visible one is the Sagittarius stream, which is considered to be a dwarf galaxy with a stellar mass of $\sim 10^7\,M_\odot$ being disrupted.

Previous studies have been providing evidence for the existence of two major components in the halo through analyses of chemical abundances and stellar kinematics (e.g., Chiba & Beers, 2000; Carollo et al., 2007; Nissen & Schuster, 2010, see Figures 1.1 and 1.2). One population has high α-element abundances, flattened distribution around the disk, and net prograde motion. This component has been interpreted as an in-situ halo in the majority of the literatures. The other population has low α-element abundances and net retrograde motion, which has been regarded as an accreted component. The two populations also differ in stellar ages (Schuster et al., 2012), supporting the suggested origins. *Note that the combination of chemical abundances and ages for halo stars has been limited to the solar neighbourhood. It needs to be extended to a larger volume considering the spatial volume of the halo (Chapter 5).*

Thanks to the Gaia mission (Gaia Collaboration et al., 2016b), under-

[5] Other streams would have been formed through dynamical disruption of globular clusters or would be perturbed stellar disk.

standings of these populations become clearer. Based on Gaia DR1 and SDSS catalogs, Belokurov et al. (2018) showed that there is a population of halo stars with highly eccentric orbit (Gaia Sausage), suggesting the presence of a past major accretion. Gaia DR2 revealed that there is a blob in the orbital energy–angular momentum space, which corresponds to the Gaia Sausage (Koppelman et al., 2018). Helmi et al. (2018) showed that the chemical abundance of the Gaia Sausage or the blob is consistent with the previously known low-α halo population. They conclude that the low-α population corresponds to a relatively massive dwarf galaxy accreted to the Galaxy, naming it as Gaia Enceladus. Although a number of studies reached the similar conclusion (e.g., Fernández-Alvar et al., 2018; Mackereth et al., 2019; Kruijssen et al., 2018; Myeong et al., 2018c; Deason et al., 2018; Haywood et al., 2018), its mass is still debated. On the other hand, a number of studies interpret the high-α population as a group of stars formed in disk and later heated to halo-like orbits (e.g., Bonaca et al., 2017; Haywood et al., 2018; Di Matteo et al., 2018; Belokurov et al., 2019).

There are certainly galaxy accretions aside from Gaia Enceladus and Sagittarius stream, but the knowledge about their properties are limited.

- The so-called Helmi stream found in Helmi et al. (1999) shows a clear clumping in the space of stellar kinematics. It has a broad metallicity distribution, suggesting a dwarf galaxy origin (Koppelman et al., 2019b), but no abundance anomalies have been detected (Roederer et al., 2010).

- Stars with a large retrograde motion seem to need an independent progenitor (Chapter 4; Matsuno et al., 2019; Myeong et al., 2019, 2018d).

- The globular cluster ω Centauri seems to have been a nucleus of a dwarf galaxy. It has a broad metallicity distribution; their Ba enhancements resemble dwarf galaxies around the Milky Way, such as Fornax dwarf spheroidal galaxy.

There are also new kinematic substructures being found at the time of writing (e.g., Yuan et al., 2019). Some of them would also turn out to be accreted galaxies. Globular clusters other than ω Centauri might also have been once a nucleus of dwarf galaxy.

Stellar populations discussed in this thesis are summarised in Table 1.1. Kinematic and chemical properties of major populations are visualized in Figures 1.1 and 1.2.

Table 1.1. Milky Way Stellar populations

Components	Name	Other names	Notes	Chapters
disk	thin disk	...	short scale height, α-poor, young	Not discussed
	thick disk	...	large scale height, α-rich, old	3
halo	high-α pop.	heated disk, splash disk	One of the two major populations	(4), 5
	low-α pop.	Gaia Enceladus, Gaia Sausage	One of the two major populations	4, 5
	Sequoia	high-E retrograde halo, highly retrograde halo		4
	ω Cen		Likely nucleus of a galaxy	4

1.3 This thesis

In this thesis, I combine all the three types of information obtained from observations of stars (chemical abundance from high-resolution spectroscopy, stellar kinematics, and ages from asteroseismology). By answering specific questions about the Milky Way stellar populations, I will show the effectiveness of the combination. Here I summarise specific questions I have highlighted in this chapter.

- What is the origin of the stellar population with chemical abundance consistent with being old and with asteroseismic mass estimates that indicate young age? Does it really challenge our understandings of the chemical evolution and that of asteroseismology? (Chapter 3)
- What is the origin of the kinematic substructure recently found from the Gaia data? Does it have a different origin from widely known halo stellar populations? (Chapter 4)
- Is the asteroseismology applicable to low metallicity stars? If so, what are the star formation timescales of halo stellar populations? Are they different from those of nearby turn-off halo stars? (Chapter 5)

This thesis consists of six chapters. The following chapter, Chapter 2, introduces analysis methods used throughout this study. It will describe how physical quantities are obtained from observations. Basic assumptions adopted in the analysis are also described. Each of Chapter 3 to 5 answers a specific question, based on a publication or a draft of a publication. Each chapter has a short introduction section, where the context of our research and the importance in this thesis are described. I conclude this thesis and provide future outlooks in Chapter 6.

Chapter 2

Methods

This chapter summarises basics of the methods and tools used throughout this thesis. I clarify where I used tools that have been developed by others and where I developed our own tools.

2.1 High-resolution spectroscopy

2.1.1 Basics

In this section, I describe the basis of abundance analysis mostly following Gray (2008). The following knowledge are essential to obtain abundances from high resolution spectra.

Formation of absorption lines

Optical depth is defined as

$$\tau_\lambda \equiv \int_\infty^z \kappa_\lambda \rho(-dz'), \tag{2.1}$$

where κ is the absorption coefficient per unit mass, ρ is the density, and z is the distance from the center of the star. Integration is from the observer to an arbitrary point in the line of sight.

Approximately, we see the light from the layer where $\tau_\lambda \sim 1$. At the wavelength that corresponds to the energy difference between two energy states of an element, κ_λ is larger due to the line opacity. Therefore we see regions closer to the surface at this wavelength. Since the local flux is approximately represented by the black body radiation with the local temperature of T, and since the local temperature in a photosphere decreases outward, the observed flux in this wavelength is smaller. This is the reason why we see absorption lines in stellar spectra. If the line absorption coefficient is too large, we cannot even see the photosphere; instead, we see the chromosphere, where the temperature increases outward. Thus, the flux

at this wavelength can be larger than the surroundings. Such emission features appear at the core of very strong absorption lines, such as Ca II HK lines. The analysis of this study is made for absorption lines formed in the photosphere.

Abundances are usually determined by analysis of equivalent widths of absorption lines. Let us consider two energy states and the transition between them. Here I define N_l as the number density of the atom in the lower energy state, χ_l, gf and λ as the excitation energy of the lower state, the statistical weight times the oscillator strength, and the wavelength, respectively, N as the total number density of the atom at the same ionization state, and A as the abundance of the element. EW denotes the equivalent width of the line. We also define θ as $5040\,\mathrm{K}/T$. Note that N_l is expressed as $N_l \propto N\exp(-\chi/k_BT) = N10^{-\chi\theta}$ in the Boltzmann distribution.

For weak lines, the shape of absorption lines approximately follows Gaussian. In this phase, the equivalent width is roughly proportional to N_l. This part is called as the linear part and the equivalent width can be approximated as

$$\log(EW/\lambda) = \log N + \log gf - \chi\theta + \mathrm{const.} \tag{2.2}$$

As the absorption line becomes stronger, the line begins to saturate. In this phase, EW is roughly proportional to $\ln N_l$. This part is called as the flat part of curve of growth since line strength is insensitive to the abundance of the species. The strength of this part is mostly dominated by the microturbulent velocity, which has been installed to explain strengths of different absorption lines for the same element using one-dimensional model atmospheres.

If the line further gets stronger, EW becomes roughly proportional to $\sqrt{N_l}$. This part is called the damping part, where the strength also depends on the damping constant.

In most cases, abundances are derived from individual lines and then averaged over. On the one hand we want to increase the number of lines to achieve high precision, but on the other hand we want to limit our analysis within the linear part to avoid using lines that are not very sensitive to the abundance. Therefore, we need to optimize the line list for the analysis depending on spectral types of the target stars.

Stellar atmospheres

In order to actually measure abundances, we need to rely on atmospheric models. In particular, temperature and pressure need to be given as a function of optical depth. These quantities together with input chemical abundance are used to calculate the number density of atoms in each ionization/excitation state. For elements that can form molecules, we also need to consider how abundant each molecule is by solving equations for chemical equilibrium.

Although model atmospheres can, in principle, be constructed by solving for equations that describe equilibria of stellar interior, we usually make use of available grids of model atmospheres. There are two grids of model atmospheres widely used in the study of abundance analysis, ATLAS (Castelli & Kurucz, 2003) and MARCS (Gustafsson et al., 2008a). Usually, these model atmospheres are in one dimension, and adopt plane-parallel approximation or spherical symmetry. They differ in some assumptions or approximations, but for most of the spectral types the difference is small enough not to affect the final abundance significantly (see e.g., Bonifacio et al., 2012).

Model atmospheres are characterized by global parameters of stars. The first parameter is the effective temperature ($T_{\rm eff}$) of the star, defined by $4\pi R^2 \sigma T_{\rm eff}^4 = L$, where R is the radius, L is the luminosity, and σ is Stefan Boltzmann constant. The second one is the surface gravity in cgs unit and in logarithmic scale ($\log g$). The third one is the chemical composition. Abundance of each element is usually scaled to the solar chemical abundance for standard models, while α-elements enhancement is taken into account for metal-poor model atmospheres considering chemical evolution.

These three parameters are needed for atmospheric model selection and microturbulent velocity is needed to create synthetic spectra. Therefore, these four parameters, which we call stellar parameters, are needed to measure abundances from absorption lines. However, stellar parameters depend on or are determined using measured abundances. Therefore, chemical abundance analysis needs an iterative process in most cases. Not only is the high-S/N of the spectra necessary, but precise determination of the stellar parameters is also a key to achieve high precision abundance measurement.

There are several ways to determine stellar parameters. One can determine all of the four stellar parameters from high-resolution spectra. In this case, effective temperature is determined by requiring all the lines of a species (usually neutral iron) to have the same derived abundance regardless of the excitation potential of the lower energy state (excitation balance), and surface gravity is by requiring abundances of an element from different ionization stages (usually neutral and singly ionized iron) to be the same (ionization balance). Microturbulent velocity is determined by a similar procedure as effective temperature but abundances are required to be independent of the line strengths instead of the excitation potential. The input abundance is determined through iterative processes.

It is obvious that stellar parameters determined spectroscopically are not independent. For example, ionization balance also depends on the temperature not only on surface gravity. Another example is determinations of effective temperature and microturbulent velocity. Since there can be a correlation between excitation potential and strengths of the lines, correlations between abundances and excitation potential and those between abundances and line strengths are not independent. Therefore, we need to find a solution simultaneously. See the appendix of Chapter 3 for a statistical treatment of

this effect.

If one is able to estimate some of stellar parameters through an independent method, the process becomes simpler. Methods to determine effective temperature include interferometric observations, photometric temperature determination, and Balmer line fitting. Interferometric observation directly provides the angular diameter of stars, with which the effective temperature is obtained. This method relies on few assumptions and thus gives most accurate temperature estimates. Photometric temperature determination uses the fact that color of stars are dependent on the effective temperature, although abundances also have some impact on stellar colors. The shape of Balmer lines is mainly controlled by the effective temperature. The dependence of the shape on other stellar parameters is also present but not significant. More severe difficulty lies in the process of getting a line shape from observations. Balmer lines are usually so broad that normalization becomes nontrivial and we need a work-around as adopted by, e.g., Barklem et al. (2002), and Matsuno et al. (2017a,b).

Surface gravity can also be constrained by several methods from, e.g., isochrone, luminosity, or asteroseismology. Since theoretical calculation predicts paths of stars in the effective temperature–surface gravity space, it is possible to estimate surface gravity once effective temperature is determined. However, this surface gravity is model-dependent and the degeneracy between effective temperature and surface gravity remains. On the other hand, surface gravity estimates based on luminosity have less model dependency and less degeneracy with effective temperature. In this method, surface gravity is estimated through the equation $g = M/R^2 = \frac{M}{L/\sigma T_{\rm eff}^4}$. Luminosity is usually obtained by using the distance to the star from astrometric measurements. This estimate requires mass and temperature but their values do not significantly impact the estimated surface gravity since what we need is $\log g$ not g. For asteroseismic surface gravity estimates, readers may refer the asteroseismology section in this chapter.

Microturbulent velocity has to usually be constrained spectroscopically since the value itself varies depending on spectral synthesis code and assumptions on the line broadening. However, as long as one sticks to a single synthesis code, the microturbulent velocity is known to correlate with effective temperature or surface gravity (see e.g., Holtzman et al., 2018). Therefore, one may self-calibrate microturbulent velocity as a function of other parameters.

Attempts to better precision

In the simplest case of the analysis of absorption lines, it is assumed that the atmosphere is static and that thermodynamic equilibrium is locally achieved. These are just approximations and real stellar atmospheres deviate to a certain extent.

In a real atmosphere, radiation can change ionization and excitation states. This effect is called as non-local thermodynamic equilibrium effect (NLTE effect). NLTE effect becomes larger for metal-poor stars since radiation transport is efficient due to small opacity. In addition, this effect is larger for the minority species of the element. For example, since large fraction of Fe is ionized in most of stars we study, NLTE effect is larger for Fe I than for Fe II.

Another important effect is three-dimensional velocity field in the atmosphere (3D effect) due to convection. The 3D effect obviously alters line shapes, and thus should be taken into account appropriately when we try to get information from the line shape. Convection has a velocity field and also causes temperature fluctuation at a fixed radius. In addition, 3D atmospheres have cool spots in the deep photosphere, which are the bubble carried by convection from the cool upper layer. As a result, abundances of molecules are enhanced compared to the corresponding 1D atmosphere.

NLTE/3D effects should be ideally taken into account for higher precision or accuracy. However, calculations including both effects are computationally heavy. Several studies have computed corrections for various type of stars to bring abundances obtained through LTE/1D analysis to the scale of NLTE/3D analysis (e.g., Amarsi et al., 2016b, 2019). By interpolating over a pre-computed grid of corrections, it is possible to obtain abundances from LTE/1D spectral synthesis in a consistent scale as NLTE/3D analysis.

An alternative approach is to carry out line-by-line analysis. Within a limited range of stellar parameters, NLTE/3D effects act in a similar manner for the same line. By deriving the relative abundance for each line, the abundance difference can be measured almost free from NLTE/3D effects. This technique is also able to cancel out the effect of incomplete atomic data (see Equation 2.2). Therefore this approach remains effective even when NLTE/3D corrections are applied or even when NLTE/3D analysis was carried out. A caution of this approach is that the high-precision is retained only among the sample studied and that one needs to consider systematic uncertainties in addition when they compare the results with other studies. In particular, the stellar parameters and abundances of the standard star have impact on derived parameters/abundances. These effects are investigated in Appendix of Chapter 5.

Another approach is to carry out data-driven spectral analysis (e.g., Ness et al., 2015; Ting et al., 2019). Firstly, we measure abundances for a small sub-sample with high accuracy, desirably in NLTE/3D analysis. Then we train an algorithm using this small sub-sample so that it can learn how sensitive each part of spectra is to stellar parameters or abundances. Finally we use this algorithm for the whole sample to obtain chemical abundances from their spectra. This approach is very powerful especially for large survey data, where a large training set can be constructed. Advantages of this approach is that once it is trained, we don't need long computational time

and that the algorithm can utilize features in stellar spectra which current physically-motivated calculations cannot model. A disadvantage is that it cannot deal with peculiar stars that fall outside of the parameter range spanned by the training set.

2.1.2 Tools

There are several abundance analysis tools including `turbospectrum` (Plez, 2012), `MOOG` (Sneden, 1973), `sptool` (developed by Y. Takeda[6]), and `SME` (Valenti & Piskunov, 1996). Most of these tools create synthetic spectra taking model atmospheres and line data as inputs. Observed spectra or measured equivalent widths are compared to those from synthetic ones to derive abundances. In this study I basically use `MOOG` or a private abundance analysis code that has originally been developed by T. Tsuji and has been used by e.g., W. Aoki (Aoki et al., 2009), which I call `MPSP` for convenience. Note, however, this naming is only within this thesis and should not be interpreted as the name of the code.

These codes are written in a medium level language such as `Fortran` for fast computation. On the other hand, a high level language, `Python`, is becoming the most popular programming language in astronomy. Therefore, there exist `Python` wrappers of these abundance analysis code. One of them is `q2` (Ramírez et al., 2014), which is a `Python` wrapper of `MOOG`. Its main feature is to derive stellar parameters and abundances based on measured equivalent widths using `MOOG`. It also has a capability to carry out a line-by-line differential abundance analysis.

I use `q2` extensively in Chapter 3 and 5 with modifications. The modifications I made are the followings:

- `MPSP` can also be selected as an abundance analysis tool
- Markov chain Monte Carlo (MCMC) methods can be used for stellar parameter determination
- (Combined with above methods) a prior on stellar parameters can be applied. This is particularly effective when asteroseismic or astrometric measurements are available.
- Measurement errors in abundance ratios of elements can be estimated more realistically
- Direct spectral fitting can be carried out from Python
- Abundances can be measured from molecules
- Line-by-line NLTE corrections can be made during stellar parameter determination using the grid provided by Amarsi et al. (2016b)

[6] `http://www2.nao.ac.jp/~takedayi/sptool/`

The revised code will be made public on `GitHub`[7] if the original author of `q2` agrees and when documents are ready.

2.1.3 Data

The high-resolution spectra used in this study are obtained with Echelle spectrographs by submitting proposals to the Subaru telescope. In Chapter 3 and 5, I was the PI of the proposals. The High Resolution Echelle Spectrometer (HIRES; Vogt et al., 1994) on Keck I telescope and the High Dispersion Spectrograph (HDS; Noguchi et al., 2002) on Subaru telescope were used to obtain spectra for Chapter 3 and 5, respectively.

Reduction pipelines are available for both instruments. `MAKEE`[8] is a pipeline for HIRES written in Fortran, and `hdsql`[9] is a `cl` script for HDS data reduction. These pipelines are used to carry out basic reduction including e.g. baseline subtraction, flat fielding, aperture extraction, cosmic ray rejection, and wavelength calibration (see each chapter for details.). `IRAF`[10] is then used to trace the continuum and to normalize observed spectra by dividing them with the continuum.

Equivalent widths are measured by fitting a Gaussian or Voigt profile to an absorption line using the normalized spectra. I made visual inspection for each fitting result. Synthesis spectra and observed spectra are also compared using the normalized spectra. In this process, I use a `Fortran` program written by W. Aoki (for Gaussian fitting) or a `Python` program I develop myself (for Voigt profile fitting).

Radial velocities are measured by cross-correlating template spectra with observed spectra using `IRAF` or by comparing laboratory measurements of wavelength of transitions with observed wavelengths of absorption lines.

2.2 Asteroseismology

In this section, I review basics about how we extract information from stellar oscillations using asteroseismology following Chaplin & Miglio (2013) and Aerts et al. (2010).

Stars with convective envelope oscillate depending on their internal properties. These oscillations are observed as slight luminosity or radial velocity variations. Therefore, we can get an access to the information of the stellar interior by measuring frequencies of oscillations from photometric or spectroscopic observations.

[7] `https://github.com/tadmatsuno`

[8] `http://www.astro.caltech.edu/~tb/makee/`

[9] `https://www.subarutelescope.org/Observing/Instruments/HDS/hdsql-e.html`

[10] IRAF is distributed by the National Optical Astronomy Observatory, which is operated by the Association of Universities for Research in Astronomy (AURA) under a cooperative agreement with the National Science Foundation

In this thesis, I mainly make use of stellar oscillation frequencies that have already been measured in literatures from photometric observations by space telescopes, such as those by Kepler (Gilliland et al., 2010; Koch et al., 2010) or CoRoT (Auvergne et al., 2009). In particular, I use two frequencies that characterize stellar oscillations, the large frequency separation ($\Delta\nu$) and the frequency at which oscillation power becomes maximum ($\nu_{\rm max}$), to deduce stellar properties.

In stars there are two modes of oscillation, pressure mode (p-mode) or gravity mode (g-mode), depending on the restoring force. The p-mode and the g-mode are sensitive to the region near the surface and to the core of the stars, respectively. Therefore, oscillations we observe are p-modes in most cases.

The frequencies of p-mode oscillations are approximated as

$$\nu_{n\,l} \simeq (n + l/2 + \alpha)\Delta\nu - \Delta\nu^2 \frac{Al(l+1) - B}{\nu_{n\,l}}, \tag{2.3}$$

where $\Delta\nu$ is defined as

$$\Delta\nu = (2\int_0^R \frac{dr}{c})^{-1} \tag{2.4}$$

with c being the sound speed and R being the radius. A is

$$A = (4\pi^2\Delta\nu)^{-1}(\frac{c(R)}{R} - \int_0^R \frac{dc}{dr}\frac{dr}{r}), \tag{2.5}$$

and B is a constant.

The observed large frequency separation is not exactly the same as the $\Delta\nu$ in Equation 2.4 but rather $\Delta\nu_{n\,l} = \nu_{n\,l} - \nu_{n-1\,l}$. However, if we neglect the second term of the Equation 2.3, we obtain $\Delta\nu_{n\,l} \simeq \Delta\nu$. Since $c^2 \propto \frac{GM}{R}$ according to the virial theorem, we get (Ulrich, 1986)

$$\Delta\nu \simeq \Delta\nu_{n\,l} \propto M^{1/2}R^{-3/2} \propto \sqrt{\bar{\rho}}. \tag{2.6}$$

On the other hand, $\nu_{\rm max}$ has been indicated to be proportional to the acoustic cut off frequency $\nu_{\rm ac}$ (Brown et al., 1991), which is proportional to c/H, where H is the density scale height. Since $H \propto T/g$ in hydrostatic equilibrium, where g is the gravity (Kjeldsen & Bedding, 1995),

$$\nu_{\rm max} \propto \nu_{\rm ac} \propto \frac{c}{T_{\rm eff}/g} \propto \frac{g}{T_{\rm eff}^{0.5}} = M\,R^{-2}\,T_{\rm eff}^{-0.5}. \tag{2.7}$$

Equations 2.6 and 2.7 are often referred to as scaling relations of asteroseismology. Although these equations have observationally been shown to be fine (e.g., Huber et al., 2012; Brogaard et al., 2016; Gaulme et al., 2016), several observations have pointed out needs for revisions (e.g., Epstein et al., 2014), which is not unexpected considering the simplicity of

the approximations. In particular, since $\nu_{n\,l}$ can be calculated using stellar structure models, theoretically motivated corrections to the Equation 2.6 have been proposed (Rodrigues et al., 2017; Sharma et al., 2016). In this thesis, `Asfgrid` (Sharma et al., 2016) is used for the correction.

Important quantities we can obtain from Equations 2.6 and 2.7 are mass and radius of stars. The mass of red giants obtained from asteroseismology are particularly important since it is almost inaccessible from other methods and since it is easily converted to stellar ages through stellar evolution model.

Another important quantity is the surface gravity. As we saw in the previous section, it is one of the parameters needed for atmospheric model selection for abundance analysis. Since Equation 2.7 contains surface gravity in linear form, it gives very precise $\log g$. Therefore, many spectroscopic surveys have observed stars with asteroseismic surface gravity constraints for a calibration purpose (Pinsonneault et al., 2014, 2018; De Cat et al., 2015; Zong et al., 2018; Martell et al., 2017; Buder et al., 2018).

2.3 Stellar kinematics

It is necessary to obtain the current location of a star in the six-dimensional space (three for the position and the other three for the velocity) to fully characterize its kinematics. The position is described by the location of the star on the sky and the distance to the star, and the velocity is described by the motion of the star on the sky (proper motion) and the radial velocity. Each of the location on the sky and proper motion needs two variables to be uniquely described. Among the six parameters, the location on the sky is easily measured with sufficient precision; human beings have been measuring it for more than 2000 years. Other parameters require dedicated observations.

The radial velocity is provided by spectroscopic observations. Large spectroscopic surveys have provided radial velocity measurements for a large number of stars.

The proper motion measurements require precise astrometric monitoring of stars. The distance can be provided by several ways, but the most model-independent way is to measure parallax, which also needs astrometric observations. Since very precise astrometric measurements are needed, these measurements have been quite limited. Dedicated space missions, Hipparcos (Perryman et al., 1997; van Leeuwen, 2007) and Gaia (Gaia Collaboration et al., 2016a), have provided parallax and proper motion measurements for a large number of stars. In particular, recent data releases from Gaia have been revolutionizing the study of the Galactic archaeology (Gaia Collaboration et al., 2016b, 2018; Lindegren et al., 2018).

Distance estimates from parallax are not as simple as it looks. In the absence of measurement errors, distance is just an inverse of parallax. How-

ever, if the parallax measurement has significant uncertainties, we need to be careful since the inverse of the parallax tends to be larger than the actual distance (Bailer-Jones, 2015). In order to avoid this bias, it is necessary to introduce an appropriate distance prior based on the knowledge of the Galactic structure. Bailer-Jones et al. (2018) have provided distance estimates based on Gaia DR2 parallax measurements using a distance prior. Although their distance estimates are unbiased for the majority of stars in the solar neighbourhood, different distance prior has to be considered when one studies a minority stellar population.

While the above measurements are relative to the solar system, coordinate transformation provides the 3D position and 3D velocity of stars relative to the Galactic center. In this process, one needs a knowledge about the position and velocity of the sun relative to the Galactic center. These have been constrained through proper motion measurements of the central super massive black hole (Reid & Brunthaler, 2004), a precise distance estimate from gravitational redshift measurements of a star close to the black hole (Gravity Collaboration et al., 2018), and study of stellar populations in the Solar neighbourhood (e.g., Schönrich et al., 2010). See also Bland-Hawthorn & Gerhard (2016) for a recent review.

Orbits of stars in the Galaxy can be integrated using the current 6D information as the initial condition. We can trace back the origin of the stars using the calculated orbits. It is essential to have a realistic Galactic potential to understand orbits of stars. For example, the mass of the Milky Way dark matter halo is one of the important parameters. If the mass is too small, many of the stars are estimated to be unbound, which is unlikely (Kim et al., 2019). The current constraint lies between around $M_{200} = 0.8 - 1.6 \times 10^{12}\,\mathrm{M}_{\odot}$.

Although orbits of stars tell us a lot about the origin of the stars, there are quantities that can be obtained without orbit integration and can characterize kinematic properties of stars. Use of these quantities has advantages in that they do not require as heavy computation as orbit integration and that they can avoid the effects of numerical noise that can be significant in orbit integration when a star approaches too close to the Galactic center.

Most of widely used Milky Way potentials are static, and thus total energy of stars is conserved. Similarly, thanks to axisymmetry of the assumed potential, angular momentum around the symmetric axis is conserved. When stars are far from the Galactic plane, the Galactic potential becomes effectively spherical, and thus all the three components of the angular momentum vector are conserved. These conserved quantities are useful, e.g., to classify stars based on stellar kinematics. In case when we observe a limited region in the Galaxy, stellar velocity itself also provides rich information.

Use of action variables becoming more popular in recent years (e.g., Chiba & Beers, 2000; Myeong et al., 2018b). Although action variables have

clear advantages that they are adiabatic invariant (Binney & Tremaine, 2008), one of the difficulties has been their estimation. In general axisymmetric potential, it is not possible to analytically obtain action variables. However, in Stäckel potential, where potential can be expressed in the form of $\frac{U(u)-V(v)}{\sinh^2 u+\sin^2 v}$, orbits of stars become analytic. Therefore, by approximating general Milky Way potentials with Stäckel potential, action variables can be estimated quickly. The key parameter for this approximation is the parameter called focal length Δ, through which coordinates are transformed from cylindrical coordinates (R, z) to (u, v), following

$$R = \Delta \sinh u \sin v \tag{2.8}$$

$$z = \Delta \cosh u \cos v. \tag{2.9}$$

Methods to estimate action variables are reviewed in, e.g., Sanders & Binney (2016).

2.3.1 Tools

`Galpy` (Bovy et al., 2016) is a `Python` package, which offers convenient classes to carry out kinematic analysis from observations. `AGAMA` (Vasiliev, 2019) is another tool for kinematic analysis which is basically written in `C++` and with a `Python` wrapper. Although `AGAMA` is written in medium-level language and fast, it does not have a function for coordinate transformation from observables to Galactocentric coordinates.

I have developed a `Python` module called `kaldas`[11] to carry out coordinate transformations, orbit integration, and action calculation from observed values in large surveys, by combining `Astropy` and `Agama`. It also has a function to estimate errors through MCMC methods. Since the data set can be too large for computer memories, calculations are automatically divided into several steps depending on the data size and the available memory size.

2.4 Summary of the tools used in this study

Table 2.1 summarises tools used in this thesis.

[11] `https://github.com/tadmatsuno/kaldas`

Table 2.1. Analysis tools used in this study

	Software	Purpose	Reference[a]	Contribution[b]	chapters
Spectroscopy	`MAKEE`	data reduction	(1)	x	3
	`hdsql`	data reduction	(2)	x	5
	`EWmeasure`	EW measurements	N/A	a	3
	`gfitsp`	EW measurements	N/A	c	5
	`MPSP`	spectral synthesis	N/A	c	3, 5
	`MOOG`	spectral synthesis	Sneden (1973)	x	3, 5
	`q2`	abundance analysis	Ramírez et al. (2014)	b	3, 5
Asteroseismology	`Asfgrid`	parameter estimations	Sharma et al. (2016)	x	5
Kinematics	`galpy`	kinematics calculation	Bovy (2015)	x	4
	`Agama`	orbit integration	Vasiliev (2019)	x	5
	`kaldas`	kinematics calculation	(3)	a	5

[a](1) `http://www.astro.caltech.edu/~tb/makee/`,
(2) `https://www.subarutelescope.org/Observing/Instruments/HDS/hdsql-e.html`
(3) `https://github.com/tadmatsuno/kaldas`

[b]a: primary developer, b: made significant revisions, c: made minor revisions, x: used as it is.

Chapter 3

High-resolution spectroscopy of young α-rich stars

From this chapter in this thesis, I present the results we obtained with collaborators. Each chapter is published or will be submitted to journals.

This work is to reveal the origin of a peculiar stellar population in the Galaxy, so-called young α-rich stars[12]. They are red giants having high [α/Fe] ratio, which is a sign of being old, although asteroseismology provides rather high mass for them, indicating their young ages. Namely these stars are chemically old but might actually be young. Existence of such stars is unexpected in standard chemical evolution models and the origin of these stars needs to be understood. From our optical high-resolution spectroscopy, we provide evidence supporting the scenario that these stars belong to a binary system and the high mass is due to binary interaction, ensuring our standard framework of chemical evolution. Therefore this study serves as a basis for the remaining two chapters, in which we interpret chemical abundances from the point of chemical evolution (Chapter 4 and 5).

3.1 Summary and context

Young α-rich stars are discovered by Martig et al. (2015) and Chiappini et al. (2015) through a combination of asteroseismology and a spectroscopic survey, Apache Point Observatory Galactic Evolution Experiment (APOGEE; Majewski et al., 2017) within the Sloan Digital Sky Survey (SDSS; York et al., 2000). They consist of about 6% of the α-rich disk population (Martig et al., 2015). In the discovery papers, two scenarios are mainly suggested as the origin. i) binary scenario, in which the high mass of these stars are attributed to binary mass transfer not to their young age. The age is consid-

[12]As we see, these stars turn out to be not actually young. However, here the name is kept to young α-rich stars throughout the thesis since there is no widely used term to describe this population.

ered to be simply underestimated because of accreted material. ii) special formation place scenario, in which these stars are considered to have formed recently in a special place in the Galaxy, where [α/Fe] ratio is locally high. A candidate place is near the end of the Galactic bar, since gas can be stagnated there. Although APOGEE provided multi-element abundances, we need additional optical spectroscopic observations since its wavelength coverage (H-band) does not allow our investigation of neutron-capture elements. Additional spectroscopic observation also enables us to test the binary scenario by adding another radial velocity measurement.

Yong et al. (2016) carried out a follow-up study for four stars using an optical high-resolution spectrograph. They confirmed α-element enhancements and showed that all the four stars do not show any abundance peculiarity compared to normal old α-rich stars. They also showed that two of them have infrared excess, suggesting the presence of a disk around the stars, which could be created through binary interaction.

Jofré et al. (2016) presented results of radial velocity monitoring for 13 young α-rich stars. They showed that fraction of stars showing radial velocity variation is higher for young α-rich stars than normal old stars. This result is consistent with the binary scenario.

The conclusion of our paper (Matsuno et al., 2018) basically supports Yong et al. (2016) and Jofré et al. (2016). We carry out high-resolution spectroscopy for 14 young α-rich stars to investigate abundance anomalies using optical spectra and to monitor radial velocity variation. Our approach is similar to Yong et al. (2016) but with more than three times larger sample. We show that 14 young α-rich stars follow the general trend of α-rich stars without abundance peculiarities. We also show that more than half of them show radial velocity variation.

All these works show that young α-rich stars are normal as stars of old population except for the high mass and their high fraction of radial velocity variation. We note that kinematics of young α-rich stars are also shown to be normal by Silva Aguirre et al. (2018). These results favour the binary scenario, which is also supported by a theoretical study (Izzard et al., 2018).

Even though the binary scenario seems to work as the origin for most of young α-rich stars, Casamiquela et al. (2018) reported an open cluster M 11 being young and α-rich. Since we cannot expect all the stars in the cluster are affected by binary mass transfer, the cluster seems to be truly young. However, we point out that this cluster is much younger than ages of young α-rich stars that are estimated under the assumption that their masses are not affected by binary interaction. Thus, different formation mechanisms could work for this cluster and for young α-rich stars.

Recently Hekker & Johnson (2019) investigated C, N, and O abundances of young α-rich stars as an indicator of their mass at the time of first dredge-up. They showed that some young α-rich stars follow the trend of low-mass red giants, suggesting that they gained mass after the first dredge-up. They

also found that the other young α-rich stars follow the trend of high-mass red giants indicating they were already massive at the time of the first dredge-up. They speculate these stars could be truly young or have gained mass before the first dredge-up through mergers.

Our work demonstrates the power of optical high-resolution spectroscopy in the sense that it provides abundances of elements having different nucleosynthesis channels (Fe, α, s-process, and r-process). In particular, high-precision abundance is a powerful tool to constrain or reveal abundance differences between stellar populations. It also shows the importance of multi-epoch spectroscopic observations in order to identify stars that have possibly been affected by binary interactions.

Importance of this work in the context of the thesis is that it ensures our standard framework of chemical evolution, by disfavoring the special formation place scenario for the origin of young α-rich stars. At the same time, this study calls an attention to those who try to interpret stellar ages obtained from asteroseismology. We need to keep in mind that the mass of a small fraction of stars does not necessarily reflect the true stellar age as a result of binary interaction.

This work is published as Matsuno et al. (2018). Following pages are based on the accepted version of the paper. The entire Table 2 and Table 4 are available on the online service, Vizier[13].

In Section 3.2, we describe observations and data reduction. The procedure of the abundance analysis is explained in Section 3.3. Based on the results presented in Section 3.4, we finally discuss the origin of young α-rich stars in Section 3.5.

3.2 Observation and data reduction

[13] http://vizier.u-strasbg.fr/viz-bin/VizieR?-source=J/ApJ/860/49

Table 3.1. Observation log

Object	2MASS ID	Exposure (s)	SNR (pix^{-1})[a]	Mass ($M_\odot$)	RV ($km\,s^{-1}$)	$RV_{(A)}$[b] ($km\,s^{-1}$)
Young α-rich stars						
CoRoT 101364068	J19281113–0020004	9000	268	1.30 ± 0.15	-49.3	-45.6
CoRoT 101665008	J19302198+0018463	9000	252	1.28 ± 0.15	0.1	-0.0
CoRoT 101748322	J19305707–0008228	3600	206	1.34 ± 0.11	20.1	11.7
KIC 10525475	J19102133+4743193	900	214	1.43 ± 0.18	-44.6	-39.6
KIC 11394905	J19093999+4913392	1800	249	1.40 ± 0.18	-74.7	-75.4
KIC 11445818	J19052620+4921373	3600	363	1.49 ± 0.16	-26.9	-26.5
KIC 11823838	J19455292+5002304	1200	180	1.57 ± 0.18	-27.0	-18.1
KIC 3455760	J19374569+3835356	1200	145	1.49 ± 0.16	-46.5	-47.6
KIC 3833399	J19024305+3854594	300	266	1.45 ± 0.17	-61.0	-62.0
KIC 4143460	J19101154+3914584	2310	229	1.58 ± 0.20	6.3	6.5
KIC 4350501	J19081716+3924583	1800	191	1.65 ± 0.20	-83.1	-83.3
KIC 5512910	J18553092+4042447	8100	169	1.66 ± 0.22	-40.4	-39.1
KIC 9269081	J19032243+4547495	2700	282	2.06 ± 0.43	-86.6	-85.8
KIC 9821622	J19083615+4641212	2700	261	1.71 ± 0.26	-5.3	-5.3
Comparison stars						
2M0001+2415	J00014289+2415111	40	304	1.40 ± 0.44	-7.1	-7.2
2M0006+4053	J00062019+4053555	40	230	0.79 ± 0.23	-76.0	-75.4
2M0040+5927	J00402003+5927517	60	214	0.76 ± 0.24	-12.5	-12.4

Table 3.1 (cont'd)

Object	2MASS ID	Exposure (s)	SNR (pix^{-1})[a]	Mass ($M_\odot$)	RV ($km\,s^{-1}$)	$RV_{(A)}$[b] ($km\,s^{-1}$)
2M0040–0421	J00404236–0421065	20	228	1.49 ± 0.44	38.0	37.3
2M0049+4104	J00491615+4104545	40	307	1.67 ± 0.54	-46.6	-46.7
2M0158+7622	J01580554+7622122	80	210	0.70 ± 0.22	-46.1	-45.8
2M0240+0253	J02404734+0253546	60	244	0.85 ± 0.27	69.1	71.8
2M0248+1817	J02483208+1817018	30	325	1.60 ± 0.48	47.1	46.7
2M0328+3548	J03284901+3548266	60	247	0.68 ± 0.21	8.7	8.1
2M0419+1416	J04194460+1416257	60	222	0.84 ± 0.25	-18.6	-19.1
2M2114+3914	J21142354+3914355	90	245	0.75 ± 0.24	-41.3	-41.4
2M2119+5303	J21194076+5303290	150	440	1.90 ± 0.59	11.1	11.2
2M2156+2109	J21563597+2109405	40	369	1.57 ± 0.50	-24.6	-24.4
2M2228+2701	J22281112+2701075	30	371	2.65 ± 0.77	-39.9	-39.6
2M2308+0207	J23084093+0207404	20	346	1.40 ± 0.41	-13.6	-25.2
2M2344+5547	J23444837+5547589	20	254	1.64 ± 0.49	5.5	6.1

[a]Measured at 6000 Å. Each pixel corresponds to $1.33\,km\,s^{-1}$.

[b]Radial velocity provided from APOGEE.

Fourteen young α-rich stars are selected from Martig et al. (2015) and Chiappini et al. (2015). All the selected stars have effective temperature ($T_{\rm eff}$) between 4500 K and 5000 K according to their estimates. The narrow range of $T_{\rm eff}$ enables us to achieve high precision in deriving relative abundances between stars. In addition, 16 nearby bright giants in Hipparcos/APOGEE sample of Feuillet et al. (2016) are selected as typical disk stars to compare the abundance pattern of young α-rich stars. The comparison sample covers similar range in $T_{\rm eff}$ and [Fe/H] as the main targets ($4500\,{\rm K} \lesssim T_{\rm eff} \lesssim 5000\,{\rm K}$, $-0.7 \lesssim {\rm [Fe/H]} \lesssim -0.2$). We try to include both α-poor and α-rich disk stars in the comparison sample, among which five result in being α-rich, though they are inclined to be metal-rich (see results). Although the selection does not include age, it is highly unlikely that the comparison sample includes many young α-rich stars given their small fraction among α-rich stars.

Observations were conducted on August 7 and 8, 2016, under good sky condition with HIRES (Vogt et al., 1994) on Keck I telescope through the time exchanging program between Keck and the Subaru Telescope (proposal ID: S16B-084). We adopt the B2 setting ($R \sim 67,000$), with the echelle angle of $-0.13°$, and the red cross disperser at the angle of $0.504°$. While the obtained spectra cover from 4200 Å to 8750 Å, we refrain from analysing bluer part of the spectra than 5200 Å to avoid the effect of significant line blending. The read-out of the CCD data were conducted with the default 2×1 binning and in the low gain setting.

Data reduction is conducted in a standard manner using `MAKEE` version 5.2.4. We then shift the spectra to the rest frame with `dopcor` after measuring radial velocities using `fxcor` in IRAF. The Arcturus spectrum of Hinkle et al. (2000) is used as the reference. While the above procedure typically gives $\sim 0.05\,{\rm km\,s^{-1}}$ as the uncertainties, we need to take into account the effects of temperature variation in the instrument during a night. The temperature variation can affect radial velocity measurements at the level of $\sim 0.5\,{\rm km\,s^{-1}}$ (Griest et al., 2010).

Continuum placements are carried out by creating a continuum mask. We first run the `continuum` task for the spectrum of 2M0248+1817 since it has high photon counts and shows strongest absorption features. Continuum of the other objects are placed by fitting the wavelength regions that are used in the continuum fitting for 2M0248+1817.

Information of targets and observation is summarised in Table 3.1.

3.3 Abundance analysis

The line data used in this study are listed in Table 3.2. We also include effects of hyperfine structure splitting in the analysis for Sc I, Sc II, V I, Mn I, Co I, Cu I, Ba II, La II, and Eu II. Isotopic shifts are also included for Ba and

Table 3.2. Line list, equivalent widths and FWHM

Object	species	wavelength (Å)	χ (eV)	$\log gf$	EW (mÅ)	$FWHM$ (Å)	Reference [a]
2M0001+2415	NaI	6154.225	2.102	-1.547	87.5	0.162	1
2M0001+2415	NaI	6160.747	2.102	-1.246	95.8	0.165	1
2M0001+2415	MgI	7387.689	5.753	-1.000	84.4	0.210	1
2M0001+2415	MgI	7691.553	5.753	-0.783	99.8	0.223	1
2M0001+2415	MgI	8717.815	5.933	-0.930	82.9	0.274	2
2M0001+2415	AlI	5557.059	3.143	-2.371	30.5	0.182	3

Note. — Portion of the table is shown. The entity is available on Vizier (`http://vizier.u-strasbg.fr/viz-bin/VizieR-3?-source=J/ApJ/860/49/table2`)

[a] 1: Kelleher & Podobedova (2008a), 2: Pehlivan Rhodin et al. (2017), 3: Kelleher & Podobedova (2008b), 4: Kelleher & Podobedova (2008c), 5: Nandy et al. (2012), 6: Smith & Raggett (1981), 7: Smith (1988), 8: Aldenius et al. (2009), 9: Lawler & Dakin (1989), 10: Lawler et al. (2013), 11: Wood et al. (2013), 12: Lawler et al. (2014), 13: Sobeck et al. (2007), 14: Lawler et al. (2017), 15: Booth et al. (1984), 16: Den Hartog et al. (2011), 17: Ruffoni et al. (2014), 18: Bard et al. (1991), 19: Bard & Kock (1994), 20: O'Brian et al. (1991), 21: Blackwell et al. (1979), 22: Blackwell et al. (1980), 23: Blackwell et al. (1982a), 24: Blackwell et al. (1982b), 25: Blackwell et al. (1986), 26: Meléndez & Barbuy (2009), 27: Lawler et al. (2015), 28: Wood et al. (2014), 29: Kock & Richter (1968), 30: Hannaford et al. (1982), 31: Klose et al. (2002), 32: Lawler et al. (2001a), 33: Lawler et al. (2009), 34: Den Hartog et al. (2003), 35: Lawler et al. (2001b).

Eu, assuming the solar ratio (Asplund et al., 2009; Rosman & Taylor, 1998). Line positions and relative strengths are taken from McWilliam (1998) for Ba II, Ivans et al. (2006) for La II and Eu II, and Robert L. Kurucz's linelist[14] for the others.

Equivalent widths (EWs) are measured in a consistent manner for all the stars. We include Voigt profile for the fitting of strong lines that have $\log(\mathrm{EW}/\lambda) > -5.0$, where λ is the wavelength of the line center.

The subsequent analysis is based on line-by-line differential analysis using q^2 (Ramírez et al., 2014), which carries out abundance calculation using `MOOG` (Sneden, 1973). Abundances are calculated with the ATLAS9 ODFNEW model atmospheres under 1D/LTE approximation with α-enhancements

[14] `http://kurucz.harvard.edu/linelists.html`

(Castelli & Kurucz, 2004). Since the temperature range of our targets is narrow, we assume departures from the 1D/LTE approximation do not significantly affect the relative scale. We have also carried out the same analysis with ATLAS9 ODFNEW model atmospheres without α-enhancements and obtained consistent results.

The reference star adopted in the analysis is KIC 11445818, which has typical stellar parameters among the observed stars. The stellar parameters and abundances of this star set the absolute scale of our analysis and need to be fixed in advance. The $T_{\rm eff}$ is taken from the calibrated APOGEE DR12 catalog. The $\log g$ is calculated using a scaling relation of asteroseismology, where $\log g_{\odot} = 4.438$, $\nu_{\rm max,\odot} = 3090\,\mu$Hz, and $T_{\rm eff,\odot} = 5777\,$K. The microturbulent velocity (v_t) is set to minimize the correlation between reduced equivalent widths ($\log(EW/\lambda)$) and abundances derived for individual neutral iron lines.

Stellar parameters of the other stars relative to KIC 11445818 are determined through fully spectroscopic analysis. We first derive abundance for each iron line. More details can be found in Appendix 3.A. Results with uncertainties are given in Table 3.3.

Once the stellar parameters have been fixed, we derive abundance of each species for a star relative to the abundance for the reference star. All the relative abundances are converted to the absolute scale using the abundance of the reference star, KIC 11445818, which is directly calculated using the line data listed in Table 3.2. Table 3.4 lists the absolute abundances with uncertainties. There are two sources of uncertainties in the derived abundance: one is originated from measurements of equivalent widths and/or modeling of absorption lines, and the other is from uncertainties in stellar parameters. The former appears as the line-to-line scatter (σ) in derived abundances and contribute to the total error as $\sigma/\sqrt{N}$, where N is the number of lines for the species used in the analysis. For the species that have less than three detectable lines and smaller line-to-line scatter than neutral iron lines, we adopt σ of iron abundance from neutral iron lines. The effect of uncertainties in stellar parameters is estimated by recalculating the abundances with the stellar parameters shifted by their uncertainties. In this process, we take the correlation between parameters into account. Since $T_{\rm eff}$ and $\log g$ are particularly degenerate in the process of stellar parameter determination, the covariance is sometimes important (Appendix 3.A). Note that the uncertainties in Tables 3.3 and 3.4 only reflect random errors only. Although the absolute scale is subject to systematic uncertainties, it does not affect the conclusion of this Chapter since we do not aim a quantitative comparison with literature sample.

Table 3.3. Stellar parameters

Object	$T_{\rm eff}$ (K)	$\sigma(T_{\rm eff})$ (K)	$\log g$ (dex)	$\sigma(\log g)$ (dex)	v_t (km s^{-1})	$\sigma(v_t)$ (km s^{-1})
2M0001+2415	4474	27	1.95	0.09	1.83	0.04
2M0006+4053	4712	39	2.67	0.09	1.74	0.04
2M0040+5927	4674	37	2.36	0.13	1.96	0.05
2M0040-0421	4561	41	1.74	0.13	1.93	0.04
2M0049+4104	4812	41	2.66	0.10	1.72	0.05
2M0158+7622	4716	42	2.60	0.10	1.55	0.05
2M0240+0253	4733	39	2.50	0.11	1.63	0.04
2M0248+1817	4440	32	1.85	0.12	1.88	0.06
2M0328+3548	4639	55	2.66	0.14	1.88	0.07
2M0419+1416	4902	52	3.30	0.14	1.62	0.07
2M2114+3914	4513	46	2.34	0.15	1.89	0.07
2M2119+5303	4764	35	2.46	0.10	1.76	0.04
2M2156+2109	4812	34	2.49	0.09	1.92	0.04
2M2228+2701	4807	31	2.27	0.11	1.79	0.04
2M2308+0207	4863	51	2.36	0.17	1.75	0.05
2M2344+5547	4883	30	2.41	0.11	1.81	0.04
CRT101364068	4618	48	2.08	0.13	1.79	0.05
CRT101665008	4706	36	2.74	0.10	1.66	0.06
CRT101748322	4736	31	2.60	0.07	1.60	0.04
KIC10525475	4764	16	2.45	0.06	1.74	0.03
KIC11394905	4854	47	2.34	0.16	1.69	0.05
KIC11445818 [a]	4767	···	2.47	···	1.81	···
KIC11823838	4892	37	2.40	0.13	1.71	0.05
KIC3455760	4699	32	2.66	0.07	1.77	0.04
KIC3833399	4677	36	2.36	0.14	1.95	0.06
KIC4143460	4801	28	2.44	0.09	1.70	0.04
KIC4350501	4864	33	2.99	0.09	1.50	0.06
KIC5512910	4854	39	2.33	0.13	1.73	0.04
KIC9269081	4752	34	2.25	0.09	1.83	0.04
KIC9821622	4807	48	2.69	0.12	1.52	0.06

[a]Reference star.

Table 3.4. Abundances

Object	Species	[X/H]	σ([X/H])	[X/Fe]	σ([X/Fe])
2M0001+2415	FeI	-0.49	0.02	···	···
2M0001+2415	FeII	-0.47	0.04	···	···
2M0001+2415	NaI	-0.17	0.04	0.33	0.04
2M0001+2415	MgI	-0.23	0.04	0.26	0.04
2M0001+2415	AlI	-0.03	0.03	0.46	0.03

Note. — Portion of the table is shown. The entity is available on Vizier (`http://vizier.u-strasbg.fr/viz-bin/VizieR-3?-source=J/ApJ/860/49/table4`)

Note. — KIC11445818 is the reference star.

3.4 Results

3.4.1 Comparison to previous studies

Asteroseismology and parallax

Figure 3.1 compares spectroscopic $\log g$ with those from asteroseismology and parallax.

All young α-rich stars have asteroseismic information, which enables us to constrain $\log g$ with the precision of ~ 0.01 dex. Since we use KIC 11445818 as reference in the spectroscopic analysis, we derive asteroseismic $\log g$ in the scale of this star as

$$\log g = 2.47 + \log(\nu_{\rm max}/37.05\,\mu{\rm Hz}) + 0.5\log(T_{\rm eff}/4767\,{\rm K}). \quad (3.1)$$

While the comparison stars do not have asteroseismic information, twelve of them and seven of young α-rich stars have parallax measurements, which also provides independent $\log g$ as

$$g = M/R^2 \propto MT_{\rm eff}^4/L, \quad (3.2)$$

where M is the mass of the star, R is the radius, and L is the luminosity. Luminosity is estimated from Gaia DR1/TGAS parallax (Gaia Collaboration et al., 2016b,a), J, H, and K_s magnitudes from 2MASS (Cutri et al., 2003), synthetic bolometric correction (Casagrande & VandenBerg, 2014), and extinction (Green et al., 2015). For the comparison stars, we adopt

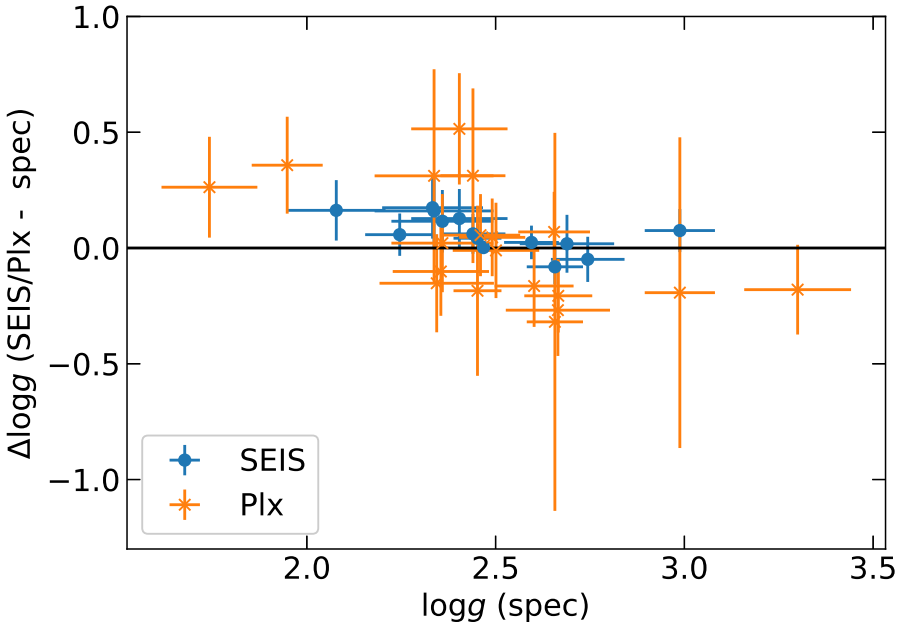

Figure 3.1 Comparison of spectroscopic $\log g$ with other methods. Averages and standard deviations of the differences are 0.06 ± 0.08 for seismic $\log g$ and 0.00 ± 0.21 for parallax $\log g$.

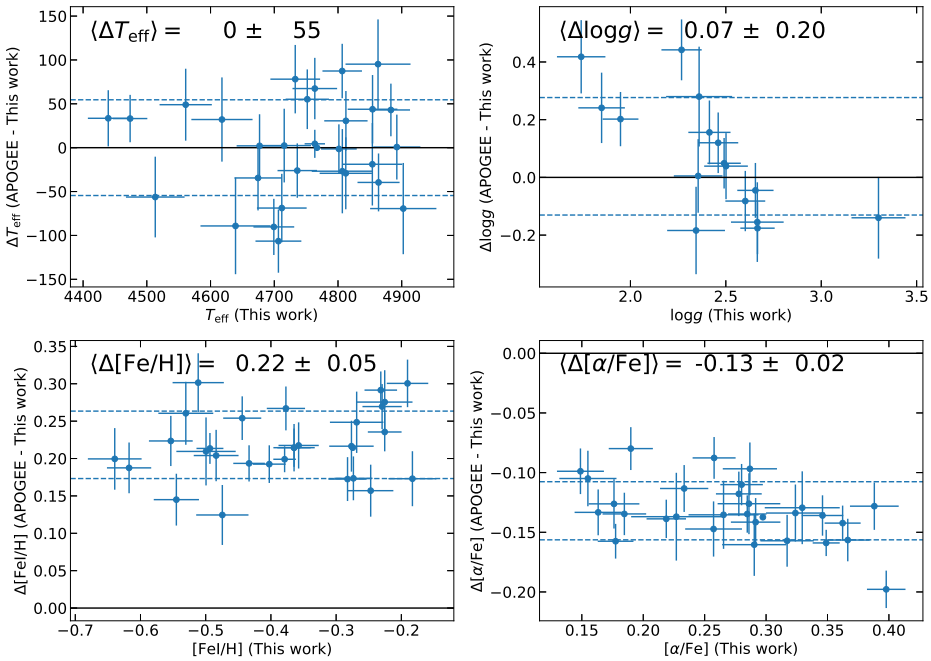

Figure 3.2 Comparison of stellar parameters with the APOGEE DR12 catalog. The average difference and standard deviation are shown in the top left corner of each panel. Horizontal dashed lines show 1σ ranges of the difference. Note that error bars do not include the contribution of systematic uncertainties or those in APOGEE.

mass estimates of Feuillet et al. (2016). For the young α-rich stars we adopt mass estimates from the scaling relation of asteroseismology.

The overall agreement is fairy good regardless of the choice of the method. Spectroscopic and parallax-based $\log g$ do not show any significant offsets (Figure 3.1), although the latter has larger error. On the other hand, asteroseismic $\log g$ gives a slightly higher value compared to the spectroscopic method by 0.06 dex in average.

Comparison with APOGEE

All of our stars are originally selected based on calibrated abundances of the APOGEE DR12 catalog. Here we compare $T_{\rm eff}$, $\log g$, [Fe/H], and [α/Fe] with the values in Chiappini et al. (2015), Martig et al. (2015), and Feuillet et al. (2016). The results are shown in Figure 3.2.

Since we adopt $T_{\rm eff}$ of the reference star obtained from the APOGEE catalog, we expect good agreement on average in this parameter. In fact, there is no significant offset in $T_{\rm eff}$. The amplitude of the star-to-star scatter is as small as expected from uncertainties of this work and APOGEE results.

The other parameters show offsets with small dispersion. We now briefly address the 0.22 ± 0.05 dex (standard deviation) offset in metallicity between our study and APOGEE results. This offset could be coupled with the estimate of $\log g$. Since we set the $\log g$ of the reference star from asteroseismology, we also compare our results with Hawkins et al. (2016), who re-analysed APOGEE spectra of stars in the *Kepler* field by utilizing asteroseismic $\log g$ constraints. The metallicity offset is smaller (0.08 dex) between our results and Hawkins et al. (2016) work. The reason for the smaller offset is, however, unclear since they did not find systematic offset between their work and the calibrated APOGEE results in their whole sample. We also tried another 1D/LTE spectral synthesis code that is used and described in, e.g., Aoki et al. (2009), and confirmed that the results are unchanged.

The [α/Fe] offset of 0.13 dex is also large compared to measurement errors. This large offset is mainly due to our higher Si abundances than APOGEE results (see next subsection).

3.4.2 α-elements

The abundances of α-elements are shown in Figure 3.3 and 3.4, with the results from Bensby et al. (2014). For the Bensby et al. (2014) sample, we define old stars as those older than 9 Gyr and young stars as those younger than 7 Gyr. Since our sample and theirs differ in spectral types, the absolute scale could differ. To take the advantages of differential analysis, the [X/Fe] of Bensby et al. (2014) is shifted by comparing the median abundance of α-normal stars (see below) in our comparison sample and young stars in Bensby et al. (2014). The corrections are 0.06, 0.32, -0.02, and 0.03 for [Mg/Fe], [Si/Fe], [Ca/Fe], and [Ti/Fe], respectively. The Bensby et al. (2014) sample is binned and median values for each bin are plotted.

We show the distributions of [X/Fe] after removing the effect of the Galactic chemical evolution. The effect is determined from α-normal comparison stars, using orthogonal distance regression. In Figure 3.3 and subsequent similar plots, the zero point of the histogram is set to the [X/Fe] value of the chemical evolution at [Fe/H] $= -0.15$ (metal-rich end of the left panel).

Overall α-enhancements of young α-rich stars compared to nearby red giants are clearly confirmed from Figure 3.4. We note that five stars in the comparison sample seem to have high [α/Fe] for their metallicity. These five stars are considered as α-rich and treated separately from the rest of α-normal comparison stars.

Trends with metallicity among the individual α-elements are similar between our α-normal stars and young stars in Bensby et al. (2014): [α/Fe] decreases as metallicity increases. The [α/Fe] of old stars in Bensby et al. (2014) are also decreasing with metallicity, but are systematically higher than young stars. Young α-rich stars and α-rich comparison stars generally

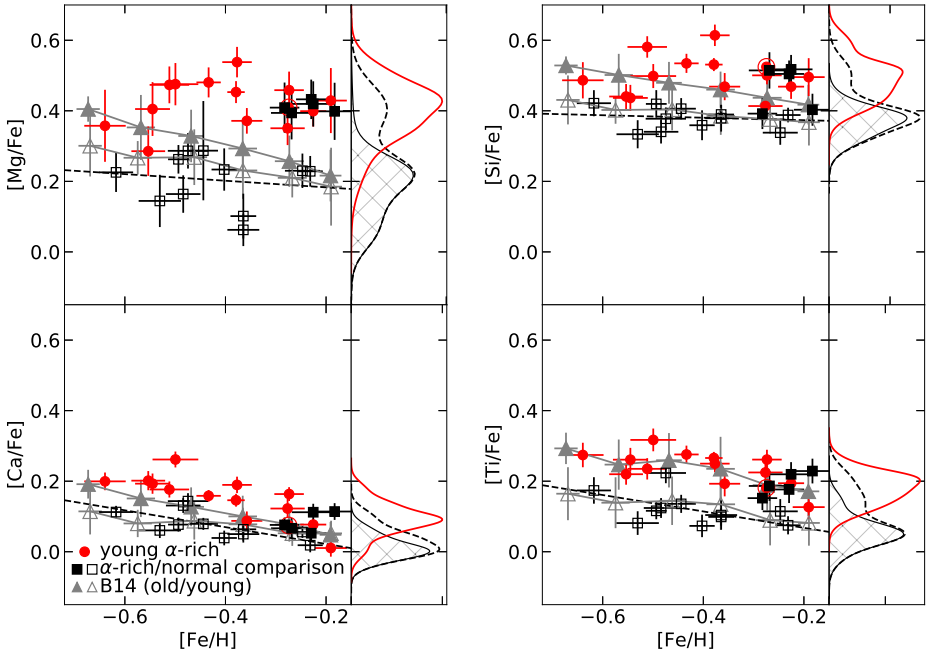

Figure 3.3 Abundances of α-elements as a function of metallicity for young α-rich stars, our comparison stars, and Bensby et al. (2014) sample (B14). The reference star is circled and shown without error bars. After correcting for the Galactic chemical evolution (black dashed line), we show the distribution of [X/Fe] of stars for each element and for each population (red solid; young α-rich stars; black solid: α-normal comparison stars; black dashed: whole comparison stars). See text for details.

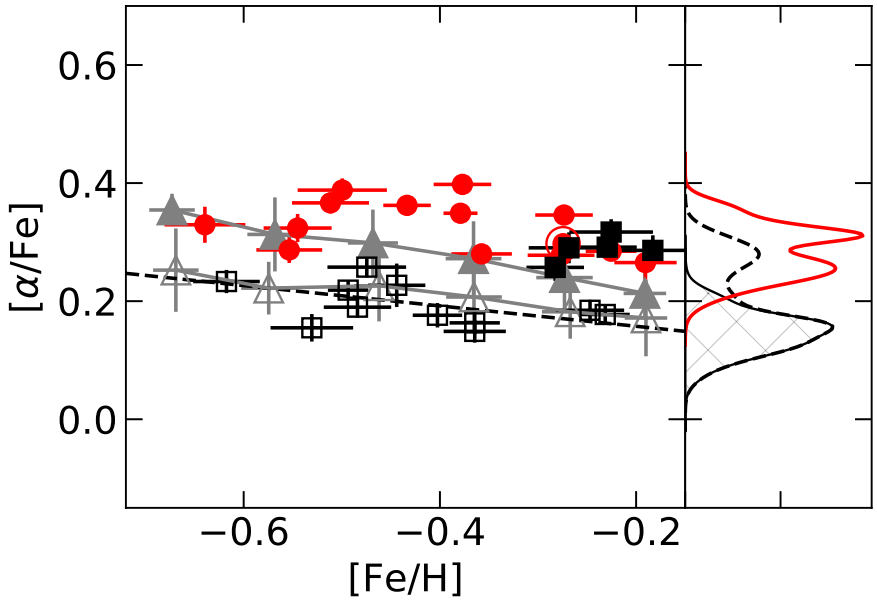

Figure 3.4 The [α/Fe] (mean of [Mg/Fe], [Si/Fe], [Ca/Fe], and [Ti/Fe]) as a function of metallicity. Symbols are the same as in Figure 3.3.

follow this trend of old stars.

The α-element abundances of young α-rich stars obtained in this study are consistent with the results of Martig et al. (2015) and Chiappini et al. (2015). They have typical abundance pattern of old thick disk stars.

3.4.3 Neutron-capture elements

While abundances of neutron-capture elements from APOGEE spectra of the young α-rich stars are not yet available, our new measurements from optical spectra shed new light on the origin of these objects. The s-process elements are produced mostly in the interior of low- to intermediate-mass stars (Karakas & Lugaro, 2016) with a longer time-scale of enrichment than α-elements. The r-process elements are considered to be efficiently synthesized by neutron star mergers (e.g., Wanajo et al., 2014a; Drout et al., 2017). Though the time scale of the enrichment is still uncertain, the early rise of r-process abundances in metal-poor stars indicates a shorter time-scale compared to that by type Ia supernovae or s-process (Argast et al. 2004, see also Ishimaru et al. 2015; Hirai et al. 2015; Hotokezaka et al. 2018), whereas some sort of supernovae are proposed to be another source (Nishimura et al., 2017). Recent high-precision abundance analysis of solar twins illustrates this timescale difference of abundance trends of neutron-capture elements

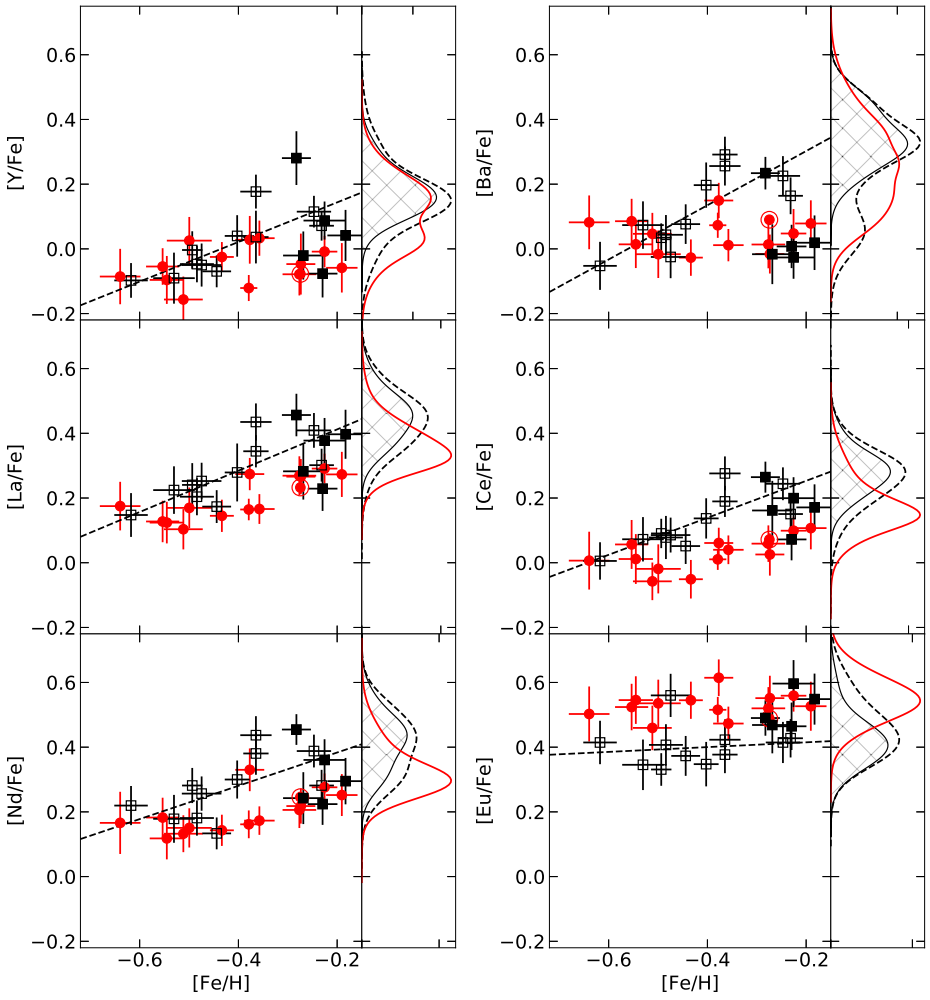

Figure 3.5 Abundances of neutron-capture elements. Symbols are the same as in Figure 3.3.

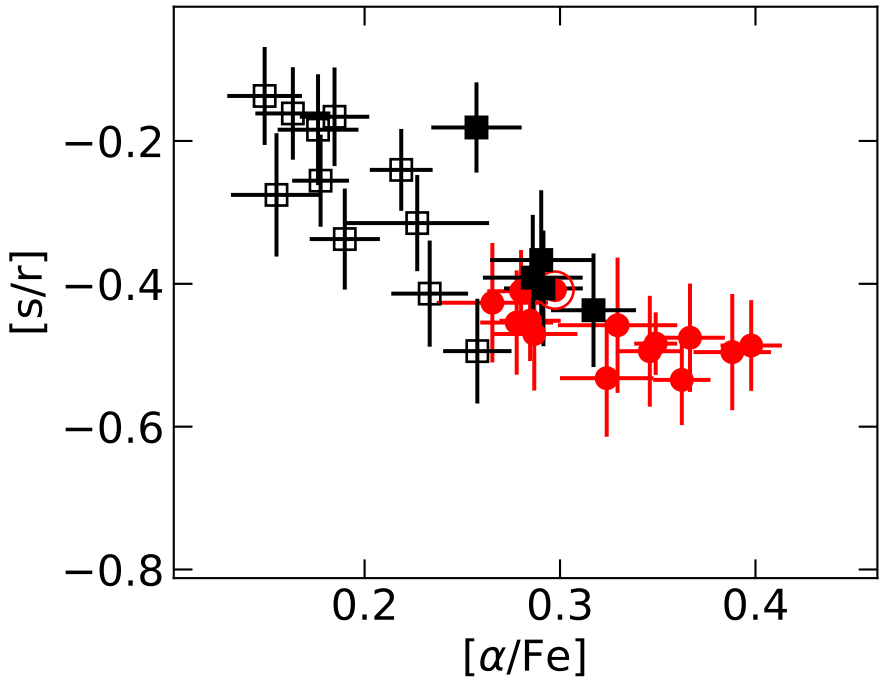

Figure 3.6 The $[s/r]$ ratio as a function of $[\alpha/\mathrm{Fe}]$. Symbols are the same as in Figure 3.3.

(Spina et al., 2018a).

We determine abundances of Y II, Ba II, La II, Ce II, Nd II, and Eu II, among which the r-process has a dominant contribution only to Eu (Sneden et al., 2008). Their abundance distributions are shown in Figure 3.5. Although Battistini & Bensby (2016) derived abundances of neutron-capture elements for the sample of Bensby et al. (2014), there are not many measurements of neutron-capture element abundances at low metallicity and the measured abundances show large scatter. Therefore, we do not include their results in figures.

The abundance ratio [X/Fe] for s-process elements increases with metallicity in α-normal stars (Figure 3.5). On the other hand, s-process abundances of young α-rich stars and α-rich comparison stars are almost flat, which results in lower s-process abundances at high metallicity. This near constancy in s-process elements supports a short time-scale for star formation as suggested from α-elements and Fe.

In contrast to the s-process elements, the Eu abundance is higher in young α-rich stars as well as α-rich comparison stars than in α-normal stars, i.e., similar feature as α-elements. This result is naturally understood from short timescale of r-process enrichments, which has been observationally shown.

To see the relative contribution of s- and r-processes, we also investigate $[s/r]$ as a function of [α/Fe] (Figure 3.6). Here $[s/\mathrm{Fe}]$ is the average of [X/Fe] for Y II, Ba II, La II, and Ce II, and $[s/r] = [s/\mathrm{Fe}] - [\mathrm{Eu/Fe}]$. Nucleosynthesis events with short time-scales such as r-process production events or type II supernovae mean that the starting point of chemical evolution are high [α/Fe] and low $[s/r]$ ratios. The later contribution from low- to intermediate-mass stars produce more Fe and s-process elements than the earlier events and move stars towards the upper left in Figure 3.6. On the other hand, mass transfer from AGB companions in binary systems should lead to high $[s/r]$ ratio with no change of [α/Fe]. Such objects are not found in Figure 3.6.

Young α-rich stars and nearby bright giants mostly follow the same trend in Figure 3.6. Importantly, none of the young α-rich stars are s-process enhanced. One of the key results of this work is that young α-rich stars are not chemically peculiar in neutron-capture elements.

3.4.4 Other elements (Li, and Na through Cu)

Abundances of other elements from Na to Cu are shown in Figure 3.7 and 3.8. Some of those elements have also been measured in APOGEE and presented in Chiappini et al. (2015).

The overall distribution of the abundances of young α-rich stars is similar to the α-rich comparison sample. This is expected from the similarities in α-elements and neutron-capture elements.

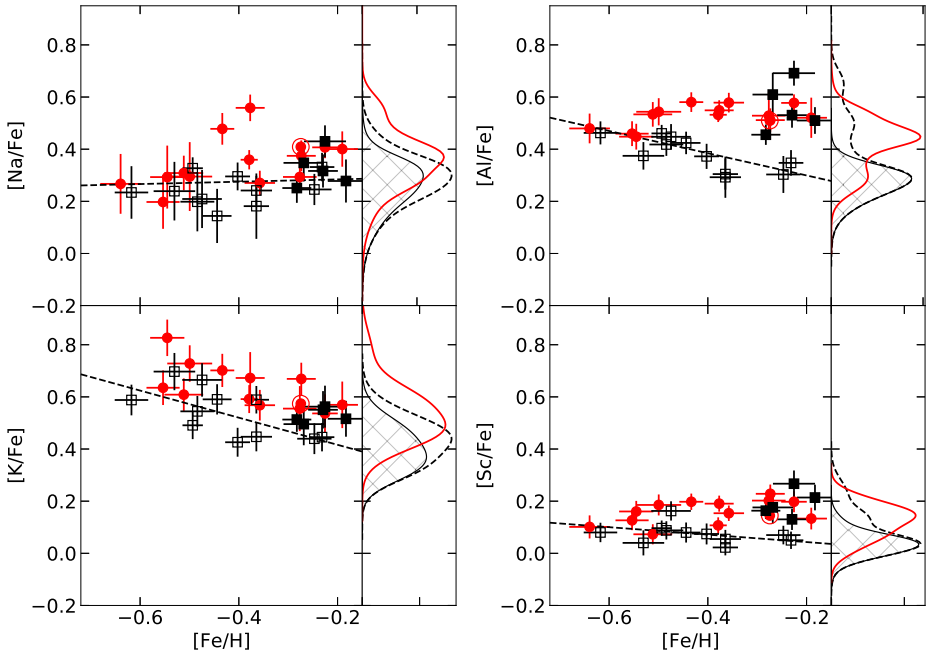

Figure 3.7 Abundances of Na I, Al I, K I, and Sc I. Symbols are the same as in Figure 3.3.

There are some young α-rich stars that seem to show mild enhancement in Na or Cu. Since the two absorption lines used for the analysis of Na at 6154 Å and 6161 Å are free from blending of other features, the measurements of equivalent widths are quite robust. By contrast, the only absorption line of Cu in the analysis is located at 5782 Å, a relatively crowded region in which the continuum placement is difficult.

The Na abundances of the two stars with high [Na/Fe] in this study (KIC 4143460 and KIC 9269081) are also high in Hawkins et al. (2016). The Na enhancements might be related to their high-mass (e.g., Luck, 1994), especially for the case of KIC 9269081.

KIC 9821622 was reported to be Li-rich in Jofré et al. (2015), which is later confirmed by Yong et al. (2016). The fraction of Li-rich objects among red giants is estimated to be $\sim 1\,\%$, and abundances of other elements have been shown to be indistinguishable from normal giants (Takeda & Tajitsu, 2017). One of the scenarios proposed to explain the Li-excess is engulfment of a brown dwarf or planet, that could accompany mass increase. If young α-rich stars have obtained mass through such engulfment, we would expect high fraction of Li-rich objects.

Among 14 objects, only KIC 9821622 shows clear Li-enhancement, which can be seen at $\sim$ 6708 Å. The line is not detectable for the others. We

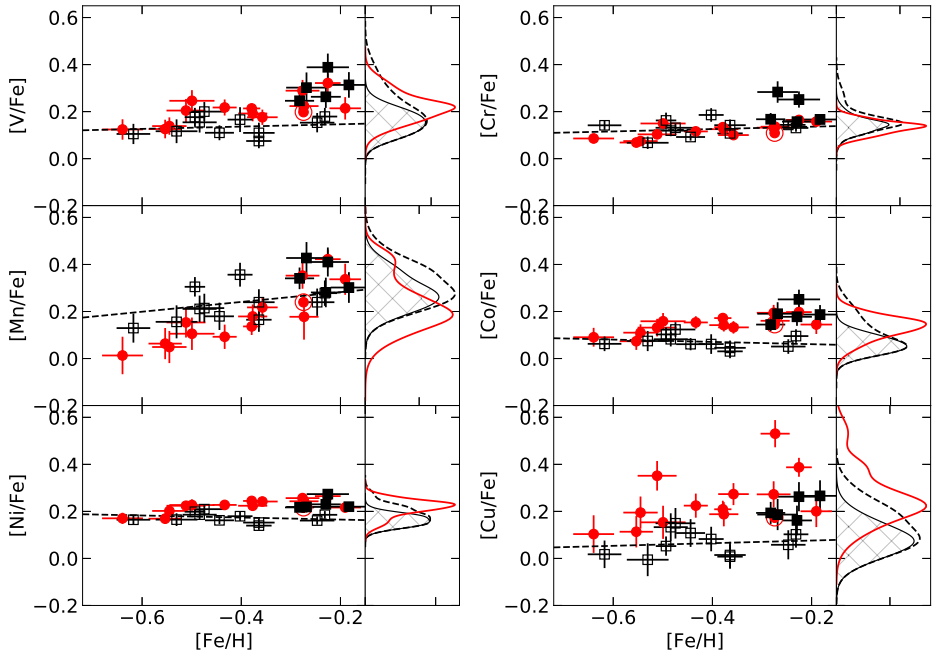

Figure 3.8 Abundances of V I, Cr I, Mn I, Co I, Ni I, and Cu I. Symbols are the same as in Figure 3.3.

estimate the fraction of Li-rich stars among young α-rich stars as $0.07^{+0.13}_{-0.02}\%$ (1σ) and $0.07^{+0.29}_{-0.06}$ (2σ) from binomial distribution. Due to the limited size of the sample, we cannot conclude if the fraction of Li-enhanced objects is high.

3.4.5 Mass and abundances

Figure 3.9 shows [α/Fe] and [s/r] abundance ratios as a function of stellar mass. In a standard framework of chemical evolution, [α/Fe] decreases and [s/r] increases as time passes. On the other hand, if binary mass transfer is not at work, mass of red giants is a proxy of stellar age in the sense that more massive stars are younger. Therefore, chemical evolution makes a trend from upper left (lower left) to lower right (upper right) in the upper (lower) panel of Figure 3.9. Binary mass transfer instead moves stars rightward in both figures [15].

Comparison stars show trends that are expected in the case of chemical evolution in both panels of Figure 3.9. Therefore, we consider that their chemical abundances and masses reflect the Galactic chemical evolution.

[15]Some binary mass transfer is known to enhance s-process element abundances. However, it is not seen in our sample as discussed with Figure 3.6.

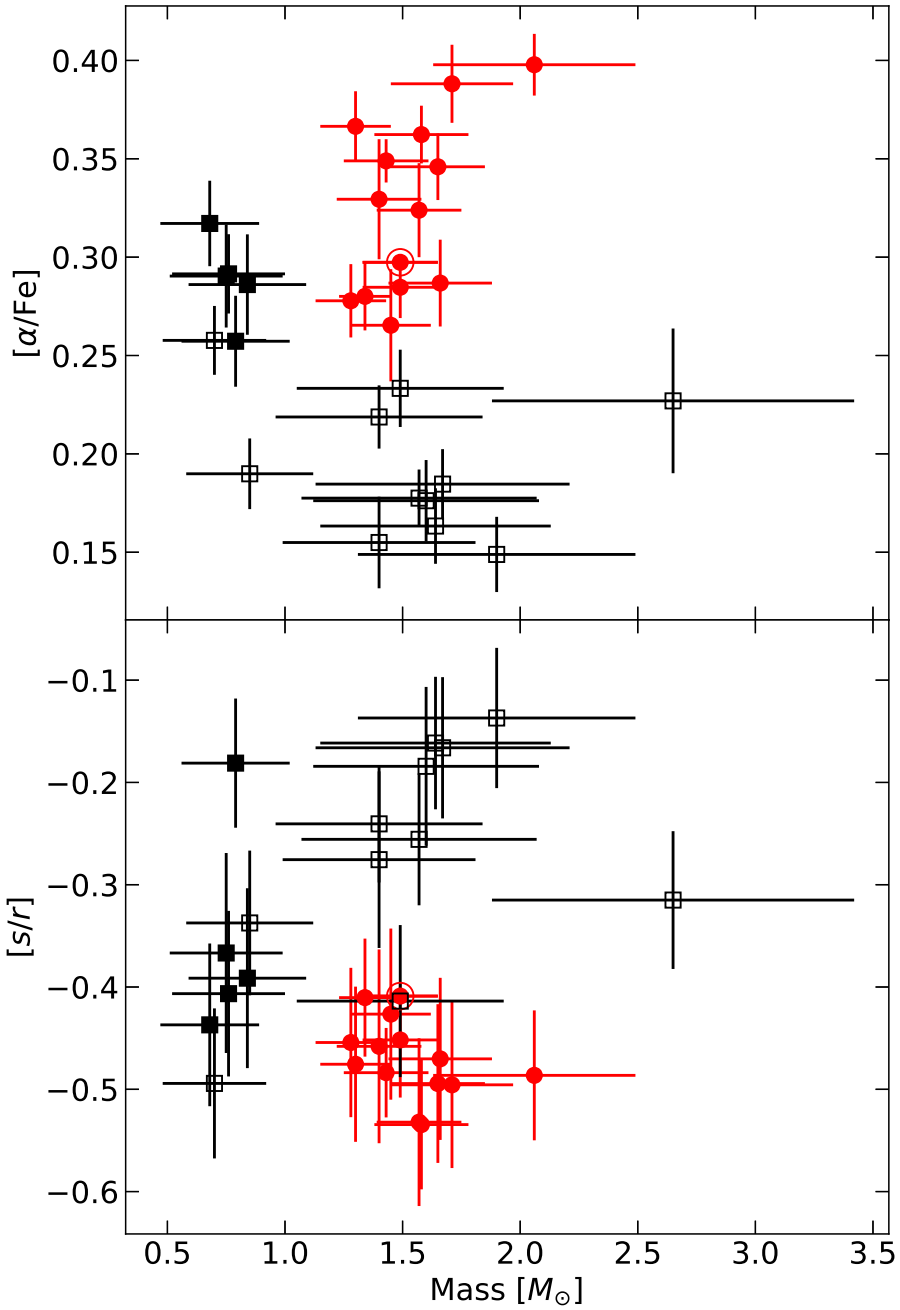

Figure 3.9 Abundances and mass of the stars. Symbols follow Figure 3.3.

Trends among young α-rich stars are clearly different from those seen among comparison stars. If young α-rich stars share the birth place, as in the special formation place scenario, they would show signatures of chemical evolution among them. A lack of such trends indicates that birth places of young α-rich stars are different from star to star.

The comparison of young α-rich stars and comparison stars in Figure 3.9 reveals that mass and abundance of young α-rich stars can be explained as a result of binary mass transfer in a old system with low mass, high-[α/Fe], and low-[s/r].

3.4.6 Radial velocities and line widths

Radial velocity variation is a sign of the existence of a companion. If mass transfer has played an important role in the formation of young α-rich stars, a significant fraction of them should exhibit radial velocity variations (Izzard et al., 2018; Jofré et al., 2016).

Radial velocity monitoring of 13 young α-rich stars has been carried out by Jofré et al. (2016). They report that six stars have high probability ($P > 0.68$) of radial velocity variation. They found that the fraction of stars with radial velocity variation is higher for young α-rich stars than for their comparison stars, though this difference is not significant at 2σ level.

We found that seven out of the 14 young α-rich stars in our study have radial velocity variation larger than $1\,\mathrm{km\,s^{-1}}$. By contrast, only two out of the 16 comparison stars show the variation. This difference is significant at the 2σ level according to Fisher's exact test ($p = 0.046$).

The $1\,\mathrm{km\,s^{-1}}$ criterion is rather conservative (see also Section 3.2). We also carry out the same test adopting a less conservative $0.7\,\mathrm{km\,s^{-1}}$ as the criterion and obtain $p = 0.057$. We conclude that the choice of the criterion does not affect our conclusion.

All of our eleven young α-rich stars in the *Kepler* field have been studied by Jofré et al. (2016). While KIC 9821622 and KIC 11394905 are not regarded as members of binary systems in this study, they have high probability of radial velocity variation in Jofré et al. (2016). On the other hand, KIC 3833399 shows radial velocity change from APOGEE to our observation, but is not identified as a binary star in Jofré et al. (2016). If we combine our results and Jofré et al. (2016), at least eight out of the 13 young α-rich stars in the *Kepler* field show radial velocity variation larger than $1\,\mathrm{km\,s^{-1}}$. Thanks to the increase of the baseline of radial velocity monitoring, we increase the likelihood that young α-rich stars belong to binary systems, which supports the mass transfer scenario.

Stellar mergers and mass transfer could cause excess of rotation velocity as a result of angular momentum transfer. We investigate the median of FWHM of iron lines with $-5.5 < \log(EW/\lambda) < -5.0$ to search for such signatures. The average of the medians of FWHM for the comparison sample

is $7.9 \pm 0.4\,\mathrm{km\,s^{-1}}$ (standard deviation), while that for young α-rich stars is $8.0 \pm 0.4\,\mathrm{km\,s^{-1}}$. The largest values are $9.1\,\mathrm{km\,s^{-1}}$ among the comparisons and $8.8\,\mathrm{km\,s^{-1}}$ among the young α-rich stars. We conclude that there is no signature of broad absorption features in young α-rich stars.

3.5 Discussion

Our findings in the Section 3.4 are summarised as follows: i) young α-rich stars have similar abundance trends to old α-rich stars. ii) they exhibit a high binary frequency. These results point to mass transfer from a companion as the dominant formation channel of young α-rich stars (Izzard et al., 2018). In particular, the lack of s-process enhancement suggests that the binary companions were not AGB stars.

The lack of s-process enhancement is well explained by the scenario of mass transfer origin. Since stars that have accreted significant amount of mass cannot survive long due to their large masses, binary interaction should have occurred recently for such stars to be observed at present. Then, the companion cannot be too massive since we assume it was coeval and survived until the recent interaction.

Chiappini et al. (2015) and Martig et al. (2015) derived $\lesssim 5\,\mathrm{Gyr}$ upper limits on age of young α-rich stars based on the assumption that they were born with the mass currently estimated from asteroseismology. This means that the mass transfer events occurred within the past 5 Gyr. On the other hand, the typical age of α-rich thick disk stars is $> 8\,\mathrm{Gyr}$. Accordingly, the companion should have lived for at least 3 Gyr, which corresponds to the lifetime of $\sim 1.5\,\mathrm{M_\odot}$ solar metallicity stars. This estimate is conservative, so we expect that most of the companions were less massive than $1.5\,\mathrm{M_\odot}$. Since stars with $M \lesssim 1.3\,\mathrm{M_\odot}$ do not produce substantial amounts of s-process elements (Karakas & Lugaro, 2016), we cannot expect many of the companions have produced significant amount of s-process elements.

Not all stars show radial velocity variation, which might indicate that some of the stars formed through stellar merger. In order to constrain the formation channel, we need to keep monitoring the radial velocities for these stars. Additional radial velocity measurements for the stars with radial velocity variation is also important to constrain the nature of the companion through its mass determination.

This work demonstrates that the apparent inconsistency between chemical abundance and ages of some red giant stars is mainly due to binary interaction. This result confirms the validity of our standard understandings of chemical evolution and ensures our use of chemical abundances to investigate the nature of stellar populations in Chapter 4 and 5. Moreover, by providing astrophysical explanation for the young α-rich stars, we rein-

force the reliability of mass estimates from asteroseismology, which is a basis of Chapter 5.

acknowledgements

We thank Dr. Paula Jofré, Dr. Luca Casagrande, and Prof. Martin Asplund for fruitful discussion, and the referee for his/her comments on the study of this Chapter.

Software: NumPy (van der Walt et al., 2011), SciPy (Jones et al., 2001–), Astropy (Astropy Collaboration et al., 2013), Matplotlib (Hunter, 2007), Pandas (Mckinney, 2010), Corner (Foreman-Mackey, 2016)

Appendix 3.A Stellar Parameter Determination

Stellar parameters ($T_{\rm eff}, \log g, v_t$) are determined by incorporating a Markov chain Monte Carlo method (MCMC) to q^2. In exchange for computational costs, use of MCMC has advantages that correlations between stellar parameters can be estimated and that an exact convergence required in the original q^2 is not needed in calculations.

As described in the main text, the determination of stellar parameters is based on the analysis of iron lines. In what follows, we use $\Delta A({\rm Fe})_i$ as the relative iron abundance derived for the line i. Following the traditional determination method, we evaluate three quantities: correlation between $\Delta A({\rm Fe})_i$ and the reduced equivalent width $REW_i = \log(EW_i/\lambda_i)$ for neutral iron lines ($r_{(EW,A)}$), correlation between $\Delta A({\rm Fe})_i$ and χ_i for neutral iron lines ($r_{(\chi,A)}$), and the difference of averages of $\Delta A({\rm Fe})$ of neutral and singly-ionized lines $dA = \langle \Delta A({\rm Fe})_i \rangle_{\rm FeI} - \langle \Delta A({\rm Fe})_i \rangle_{\rm FeII}$[16]. We assume that when we use the appropriate set of stellar parameters, each $\Delta A({\rm Fe})_i$ is distributed randomly around the true relative abundance. In other words, the basic assumption is that when the uncertainties of measured equivalent widths are infinitesimal and when the proper stellar parameters are used in the analysis of a star, relative iron abundances derived for individual iron lines $\Delta A({\rm Fe})_i$ would be the same.

The likelihood can be decomposed as

$$\mathcal{L}(r_{(EW,A)},\, r_{(\chi,A)},\, dA | T_{\rm eff},\, \log g,\, v_t) = f(r_{(EW,A)},\, r_{(\chi,A)}) \times f(dA). \quad (3.3)$$

Note that $r_{(EW,A)}$ and $r_{(\chi,A)}$ are not independent because both involve $\Delta A({\rm Fe})_i$. Therefore, the distribution of $(r_{(EW,A)}, r_{(\chi,A)})$ should be inves-

[16] $r_{(X,Y)}$ denotes the Pearson's correlation coefficient between variables X and Y.

tigated under the presence of $r_{(EW,\chi)}$, and hence,

$$f(r_{(EW,A)}, r_{(\chi,A)}) = f(r_{(EW,A)}, r_{(\chi,A)}|r_{(EW,\chi)}) \quad (3.4)$$

$$= \frac{f(r_{(EW,\chi)}|r_{(EW,A)}, r_{(\chi,A)}) f(r_{(EW,A)}) f(r_{(\chi,A)})}{f(r_{(EW,\chi)})}, \quad (3.5)$$

where $f(r_{(EW,A)})$, $f(r_{(\chi,A)})$, and $f(r_{(EW,\chi)})$ are the probability distribution function of Pearson's correlation coefficient for an independent set of two variables, and $f(r_{(EW,\chi)}|r_{(EW,A)}, r_{(\chi,A)})$ is that of partial correlation coefficient. The $f(dA)$ is calculated using Student's t-test described in the Section 14.2 of Press et al. (1992).

We use flat priors with boundaries on $T_{\rm eff}, \log g, v_t$. The initial guess is adopted from the estimates by q^2, though the choice of the initial guess does not affect the final results. The EnsembleSampler in `emcee` (Foreman-Mackey et al., 2013) was used to sample the posterior probability distributions. The median of each parameter is adopted in the abundance analysis, and the half of the difference between 16th and 84th percentile values is adopted as the uncertainty. Correlation coefficients between parameters are estimated and used in the error estimation of the abundances.

In Figure 3.10, we show an example of scatter plots for 2M0040+5927 with the result from q^2. It is clear that the two methods are basically consistent. The effectiveness of the MCMC method is that we can estimate the correlations between parameters. In principle, we can adopt a prior from asteroseismology or parallax measurements, which serves to resolve degeneracies.

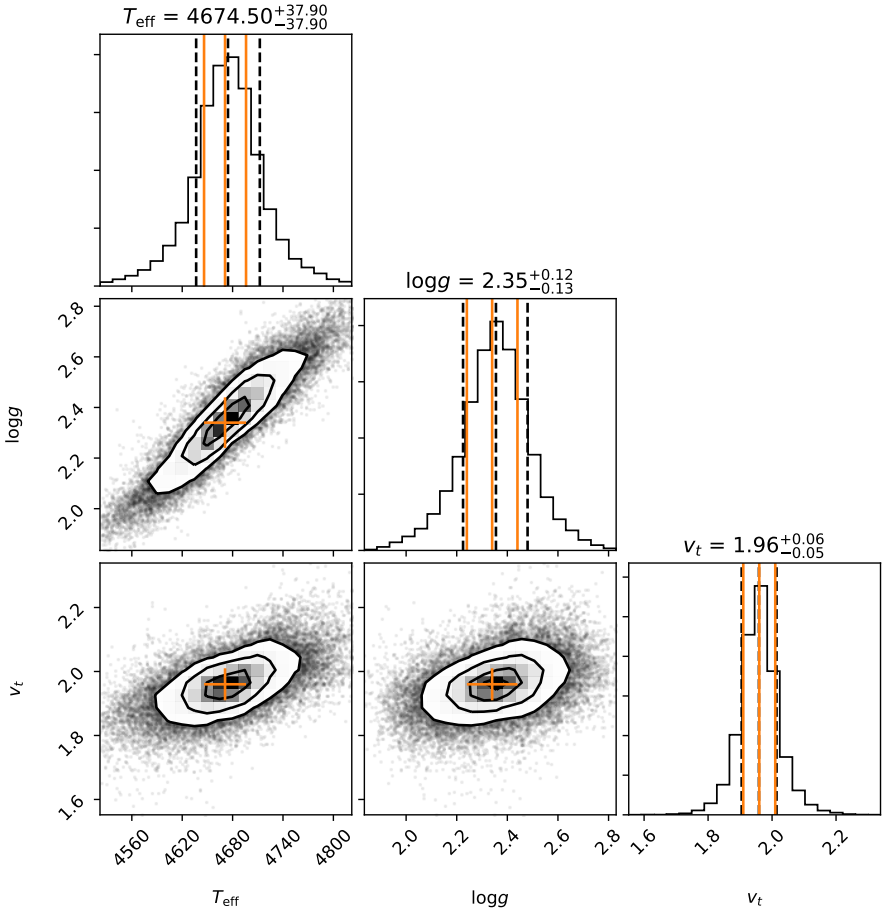

Figure 3.10 Corner plots to show the result of the MCMC stellar parameter determination. Black dashed lines in the histograms show 16th, 50th, and 84th percentile values. Orange plus signs in corner plots and solid lines in histograms show the parameters and 1σ uncertainties given by the original q^2.

Chapter 4

Chemical abundance of a kinematic substructure

The work on young α-rich stars is followed by the study of kinematics and chemical abundances of halo stars. We confirmed in the previous chapter that our understandings of chemical evolution hold valid, and we now interpret chemical abundances of groups of halo stars with different kinematics in this Chapter. We show that a recently discovered kinematic substructure of stars shows a chemical abundance signature of accretion origin. The chemical abundance also suggests that this substructure needs a progenitor with a long star formation timescale that is independent of known accreted galaxies, providing a new insight about the Milky Way merging history.

4.1 Summary and context

This work is to clarify the origin of a kinematic substructure of stars in the Galactic halo by studying chemical abundances. Helmi et al. (2017) and Myeong et al. (2018b) pointed out there is an excess of stars with highly retrograde orbit with high orbital energy in the Galactic halo using data from Gaia DR1. Here we regard this excess as a kinematic substructure and call it high-E retrograde halo, which is later named as "Sequoia" (Myeong et al., 2019). Myeong et al. (2018d) carried out a follow-up study of retrograde kinematic substructures and suggested that they might be related to the globular cluster ω Centauri. However, the velocity distribution of the retrograde stars can also be consistent with being a part of Gaia-Enceladus (Helmi et al., 2018). These studies indicate needs for chemical abundances to unravel the origin of this substructure. We suggested that this substructure forms a distinct chemical abundance sequence with very low α-element abundances using a database of stellar chemical abundances. Our results support that the high-E retrograde halo is caused by an accretion event that is independent from Gaia-Enceladus. We also show that Ba abun-

dances are different from ω Centauri suggesting that the cluster is unrelated to the high-E retrograde halo.

The existence of the excess of highly retrograde stars with high orbital energy was pointed out by Helmi et al. (2017) based on Gaia DR1 and RAVE data. They showed that fraction of stars with highly retrograde orbits is so high that it is very rare in cosmological simulations. Myeong et al. (2018b) used a catalog that combined Gaia DR1 and SDSS, and showed that the excess was only seen between [Fe/H]$= -1.9$ and -1.3. Based on the lack of the excess at lower metallicity, they argued that the progenitor should be massive. Since ω Centauri also has large retrograde motion for its energy and is considered to be a nucleus of a dwarf galaxy, they speculated the connection between the retrograde excess and ω Centauri. Myeong et al. (2018d) re-identified seven retrograde substructures using the same catalog and investigated if dynamical properties of those substructures and ω Centauri are explained by the same accretion event using model calculation. They proposed that 5 retrograde substructures could be associated with ω Centauri. Considering the current orbital energy and angular momentum, they suggested that the progenitor should have been more massive than $5 \times 10^8\,\mathrm{M}_\odot$. The excess is also later confirmed with Gaia DR2 (e.g., Koppelman et al., 2018).

These studies are based on analyses of stellar kinematics and metallicity. As mentioned in Myeong et al. (2018d), detailed chemical abundances are necessary to pin down the origin and characterize the progenitor. Moreover, simulation of the merger of Gaia-Enceladus presented in Helmi et al. (2018) showed that it is also possible for Gaia-Enceladus to deposit stars to highly retrograde orbits. Chemical abundances provide a way to investigate if the progenitor is independent from Gaia-Enceladus or not. Since ω Centauri shows unusually high Ba abundance, chemical abundance of the high-E retrograde halo will also bring us the information about its connection to the globular cluster.

Since large high-resolution spectroscopic surveys do not include sufficient number of highly retrograde stars and their precision is not sufficient at low metallicity, no chemical abundance was provided at that time. However, there was a suggestion about the chemistry of the retrograde stars. Stephens & Boesgaard (2002) have observed nearby outer halo stars that are selected from their velocity and suggested that the outermost halo stars tend to have lower [α/Fe] abundance ratio than other halo stars. Venn et al. (2004) showed that the [α/Fe] ratio actually correlates with rotation velocity around the Galactic center in the sense that highly retrograde stars tend to have lower α-element abundances. Although these studies have provided a hint about the chemical abundances of retrograde stars, it would be of great importance to revisit and reinterpret the chemical abundances of retrograde stars in the context of current understandings of the Galactic halo with the Gaia data. In particular, the connection between chemical abundances of

retrograde stars and the high-E retrograde halo needs to be investigated.

In Matsuno et al. (2019), we investigated chemical abundance of the high-E retrograde halo using the SAGA database (Suda et al., 2008), in which chemical abundances measured in past studies are compiled. We select candidate member stars of the substructure based on angular momentum and orbital energy of stars that are calculated using the Gaia DR2 data, since the substructure was first found in the angular momentum – orbital energy space. Abundances of Na, Mg, and Ca of the selected stars seem to be lower than other halo stars. This difference is confirmed for Mg and Ca using a simple fit to the chemical evolution trend. We also explicitly showed that the metallicity distribution peaks at lower metallicity than Gaia-Enceladus using LAMOST DR4. These results suggest that the high-E retrograde halo needs an independent and lower mass progenitor than Gaia-Enceladus. We also show that Ba abundance of the selected stars is clearly different from ω Centauri, suggesting they would be unrelated.

After the publication of our work, several studies added insights to this kinematic substructure. Basically our conclusion on chemical abundances are consistent with Monty et al. (2019) and Koppelman et al. (2019a). The former reanalyses stars in Stephens & Boesgaard (2002) confirming its abundance scale and reinterpret abundances of those stars in the context of the current understandings the Milky Way formation. The latter study (Koppelman et al., 2019a) is based on APOGEE DR14. They also compared observed distribution of stellar kinematics with mock accreted dwarf galaxies and concluded that it is unlikely that the high-E retrograde halo and ω Centauri are brought from the same dwarf galaxy. We note that they did not exclude the possibility that the substructure corresponds to the outer part of the Gaia Enceladus.

Motivated by the discovery of a globular cluster with a highly retrograde orbit (FSR 1758; Barbá et al., 2019; Simpson, 2019), Myeong et al. (2019) associated six globular clusters, including ω Centauri to this kinematic substructure from analysis of action variables. They also identify possible member stars in APOGEE DR14. Based on the property of the six globular clusters (dynamics, age-metallicity relation, and the total mass), and metallicity and abundance distributions of APOGEE member stars, they argue that the high-E retrograde halo needs an independent progenitor, which they call Sequoia [17].

Our work demonstrates the power of the combination of chemical abun-

[17] Actually abundance trends Myeong et al. (2019) obtained from APOGEE do not show good agreement with our results. However, we note that the precision of APOGEE abundance is not high at the metallicity of Sequoia. In addition, since APOGEE target giants, most of which are distant, Gaia measurements of parallax for APOGEE stars are not very precise, and hence they used spectroscopic distance. They used the space of action variables instead of the angular momentum – energy space. These might be possible sources of the inconsistency.

dances and stellar kinematics for understanding the Milky Way accretion history. While analyses of stellar kinematics can reveal accretion signature candidates and provide hypothesis about their origins, chemical abundances enable us to confirm the existence and constrain the hypothesis. This work also shows that although we are entering the era of large spectroscopic surveys, individual spectroscopic observations remain powerful for low metallicity stars. We also note that this study does not benefit from high-precision abundance from differential analysis. The fact that the abundance difference we investigated in this study was close to the level of uncertainties indirectly indicates needs for future high-precision abundance analysis.

The importance of this work is that we provide supports for the existence of a halo stellar population with accretion origin in addition to the two major halo populations.

This work is published as Matsuno et al. (2019). Following pages are based on the accepted version of the paper.

4.2 Sample

4.2.1 Target selection from the SAGA database

Chemical abundances

The abundances of metal-poor stars were extracted from the Stellar Abundances for Galactic Archaeology (SAGA) database (Suda et al., 2008, 2011; Yamada et al., 2013; Suda et al., 2017). This database compiles abundances of metal-poor stars from studies that used high- or medium-resolution spectrographs ($R \gtrsim 7,000$). Given that the density of metal-poor stars on the sky is very low, high-resolution spectroscopic surveys using multi-object spectrographs are not efficient. Therefore, the use of the SAGA database is an efficient way to obtain chemical abundances of many elements for a large number of metal-poor stars. We started with $\sim$ 2,100 metal-poor stars ([Fe/H]< -0.7) in this database.

Since our study is based on the abundance data collected from literature, we take two major sources of abundance uncertainties in the SAGA database into consideration. One is caused by different methods of abundance analyses among different studies, for example, different stellar parameters or different line lists. The other is that we mixed various types of stars from main-sequence stars to red giants, between which there could be offsets in abundances caused e.g., by departures from the local thermo-dynamic equilibrium and plane-parallel approximations in real stellar photospheres (non-LTE/3D effects). Hereafter, we denote σ_1 and σ_2 to indicate the contribution from the first and the second effect, respectively. The total uncertainty σ can be expressed as $\sigma^2 = \sigma_1^2 + \sigma_2^2$. We note that literature uncertainties are not explicitly adopted in the error estimate here because these uncertainties

should be included in the σ values evaluated by the following procedure.

In the following assessments of uncertainties, we used all the stars in the database that have $-3.0 <$[Fe/H]< -2.5 and those have $-2 <$[Fe/H]< -1. The σ values are expressed as $\sigma_{\rm mp}$ and $\sigma_{\rm mr}$ for the former and the latter sample, respectively. As seen below, our focus in this Chapter is the metallicity range $-2 <$[Fe/H]< -1, and hence $\sigma_{\rm mr}$ matters. The σ_1 was assessed by investigating the median value of standard deviations of abundance measurements for individual objects for which more than two studies had reported abundances. The $\sigma_{1,\rm mp}$ values (numbers of stars used) are $0.18\ ^{+0.06}_{-0.04}$ (20), $0.13\ ^{+0.05}_{-0.03}$ (42), $0.08\ ^{+0.02}_{-0.03}$ (35), $0.16\ ^{+0.07}_{-0.04}$ (43) and $0.10^{+0.08}_{-0.02}$ (103) for [Na/Fe], [Mg/Fe], [Ca/Fe], [Ba/Fe], and [Fe/H], respectively and the $\sigma_{1,\rm mr}$ are $0.07\ ^{+0.05}_{-0.02}$ (79), $0.10\ ^{+0.03}_{-0.04}$ (97), $0.06\ ^{+0.03}_{-0.02}$ (90), $0.18^{+0.04}_{-0.04}$ (90) and $0.10^{+0.04}_{-0.04}$ (196). The superscript and subscript indicate the values between the third quartile and the median and that between the median and the first quartile, respectively. We also directly evaluated $\sigma_{\rm mp}$ by examining a spread of [X/Fe] for each element with the assumption that intrinsic abundance spreads are smaller than measurement errors at $-3 <$[Fe/H]< -2.5[18]. We conducted a linear regression and took the half of the difference between 16th and 84th percentiles of residuals as $\sigma_{\rm mp}$. The $\sigma_{\rm mp}$ values (numbers of stars used) are 0.31 (96), 0.13 (312), and 0.11 (310) for Na, Mg, and Ca[19]. Note that $\sigma_{\rm mp}$ evaluated by this process reflects both two sources of uncertainties. Thus it is possible to calculate $\sigma_{2,\rm mp}$ from the equation $\sigma^2_{\rm mp} = \sigma^2_{1,\rm mp} + \sigma^2_{2,\rm mp}$ as $\sigma_{2,\rm mp} = 0.25$, 0.00, 0.08 respectively[20]. Assuming σ_2 does not depend on metallicity (i.e., $\sigma_{2,\rm mp} = \sigma_{2,\rm mr}$), we get $\sigma_{\rm mr}$ =0.27, 0.10, and 0.10 for [Na/Fe], [Mg/Fe], and [Ca/Fe][21]. Since there is no way to estimate $\sigma_{\rm mp}$ for [Fe/H] and thus $\sigma_{2,\rm mp}$ and $\sigma_{2,\rm mr}$, we assumed $\sigma_{\rm mr} = 1.5 \times \sigma_{1,\rm mr} = 0.15$ without estimating σ_2 values. It is also not possible to estimate $\sigma_{\rm mp}$ for [Ba/Fe] due to the intrinsic abundance spread at low metallicity. Therefore, we again skipped the estimation of σ_2 and assume $\sigma_{\rm mr} = 0.27$ for [Ba/Fe]. The estimated errors are small enough not to significantly affect our conclusions.

The systematic uncertainties of abundances among different papers are discussed in Suda et al. (2008) where they picked up 17 stars having multiple measurements for carbon abundances, and compared their offsets for the stellar parameters and abundances (in their Fig.10). Possible causes of the

[18]This is not feasible for the metal-rich sample, since abundance ratios are sensitive to the time scale of star formation.

[19]We use stars with $-2.5 <$[Fe/H]< -2.0 to measure $\sigma_{\rm mp}$ for Na since there is a population of extremely metal-poor stars that show very large Na enhancement.

[20]The above estimate results in $\sigma_{1,\rm mp}$ value comparable to $\sigma_{\rm mp}$ for [Mg/Fe]. We interpret σ_2 is negligible for [Mg/Fe] and consider $\sigma_{2,\rm mr} = 0$. This would be because of similar ionization potentials of neutral Mg and Fe.

[21]The large metallicity dependence of σ_1 for [Na/Fe] is probably because Na abundance measurements have to rely on the D lines at low metallicity, which are sensitive to the NLTE effect. σ_2 is also expected to be smaller for high metallicity stars and $\sigma_{\rm mr}$ for [Na/Fe] is likely to be overestimated.

uncertainties are also listed, while the inconsistency by the use of different solar abundances from paper to paper is alleviated by the update of the database as discussed in Suda et al. (2017).

Positions, distances, and proper motions

Stellar positions and proper motions were obtained from Gaia DR2. Here, we briefly explain the process of crossmatching the SAGA database to Gaia DR2. The details of the method will be presented in a forthcoming paper.

We complemented incomplete stellar position data in the database from Simbad using star names and inspected 2MASS images (Cutri et al., 2003) to examine the accuracy of the positions. After manually correcting the coordinates as required, the SAGA database was crossmatched to 2MASS using the coordinates. Most of the stars are sufficiently bright to be detected by 2MASS. Finally, astrometric information was obtained via the `gaiadr2.tmass_best_neighbour` catalog. Twenty-five relatively faint stars have no counterparts in the 2MASS point source catalog. We searched for these 25 objects directly in the `gaiadr2.gaia_source` catalog and visually checked the results using Pan-STARRS images. With a few exceptions, the SAGA database was successfully crossmatched with Gaia DR2. We plan to update the SAGA database to include Gaia information, as well as the kinematics of metal-poor stars. We adopted the distance estimates of Bailer-Jones et al. (2018) and further restricted the sample to stars with `parallax_over_error`> 5. We also imposed an additional criterion using the equation C.1 of Lindegren et al. (2018). After these processes, 1,571 metal-poor stars remained.

Radial velocities

To obtain radial velocities, three sources were combined: Gaia DR2, the SAGA database, and Simbad, as none of them alone provided radial velocities for a sufficient number of stars. Radial velocities in the SAGA database and Simbad are based on past measurements in the literature; thus, these sources have heterogeneous data quality. The consistency among sources was evaluated by comparing their radial velocity values with those reported in Gaia DR2. Radial velocity data from the SAGA database were consistent with the measurements obtained by Gaia DR2 at the $2-3\,\mathrm{km\,s^{-1}}$ level; those obtained from Simbad showed similar consistency when using values of quality A or B.

We established priority in the order of Gaia DR2, SAGA database, and Simbad. We excluded stars that showed significant radial velocity differences ($> 10\,\mathrm{km\,s^{-1}}$ corresponding to $\sim 3\sigma$) between different sources; most of them are considered to be in binary systems. As a result, we were left with 1,290 metal-poor stars that showed no distinct radial velocity variation with good

parallax measurements.

Kinematics

We used `galpy` (Bovy, 2015) to calculate kinematics of stars. We firstly removed disk stars by applying $||\mathbf{v} - \mathbf{v}_{\rm LSR}|| > \mathbf{180}\,{\rm km\,s^{-1}}$. As a result, we have 882 stars, among which 50% are within 0.88 kpc and 75% are within 2.07 kpc.

Energy (E) and angular momentum (L_z) were calculated adopting a modified `MWPotential2014` as the Milky Way gravitational potential (Bovy, 2015). We replaced the relatively shallow NFW potential in the `MWPotential2014` with the one with virial mass $M_{200} = 1.4 \times 10^{12}\,{\rm M}_\odot$. The concentration parameter was also changed to $c = 8.25$ to match the rotation curve of Milky Way (private comm. with K. Hattori). We subtracted the potential energy at a very large distance from the obtained E to get $E = 0$ at an infinite distance from the Galactic center, as explained in the document of `galpy`. The obtained $E - L_z$ distribution is presented in Figure 4.1.

4.2.2 LAMOST DR4

Since the number of stars in the database is still not very large and since there is a clear bias toward metal-poor stars in the database, we also investigate the $E - L_z$ distribution of metal-poor A-, F-, G-, and K-type stars catalogued in LAMOST DR4 (Cui et al., 2012, lower panel of Figure 4.1). We simply crossmatched stars in LAMOST estimated to be [Fe/H]< -0.7 to Gaia DR2, and selected halo stars with the same criteria as those used for the SAGA database stars. We have 35069 stars from LAMOST, and 50% of stars are within 1.75 kpc and 75% are within 2.63 kpc. We just used these LAMOST stars to confirm the $E - L_z$ distribution of stars in the SAGA database and to investigate metallicity distributions of selected regions.

4.2.3 Selection boxes

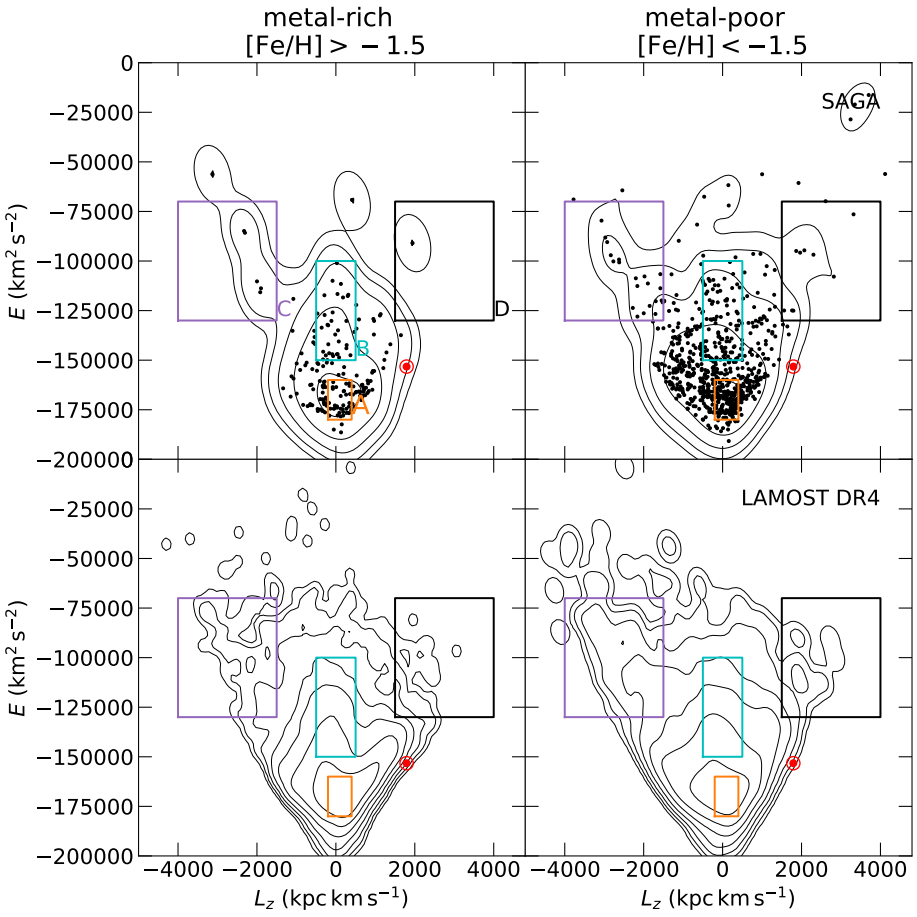

Figure 4.1 Distribution of stars in the energy (E) – angular momentum (L_z) space after dividing by the metallicity [Fe/H]$= -1.5$, for stars in the SAGA database (*upper* panel) and in A-, F-, G-, and K-type stars catalogued in LAMOST DR4 (*lower* panel). Individual stars in the SAGA database are plotted, as well as the contour; for LAMOST stars, only the contour is shown. The rectangles show the four regions used in subsequent chemical analyses (Table 4.1). The location of the Sun is also shown by red circles.

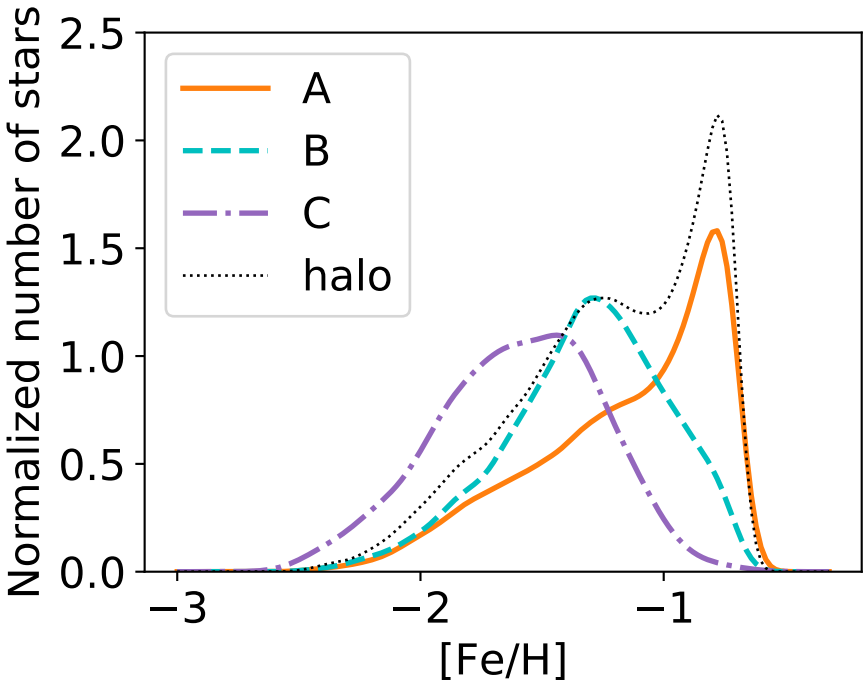

Figure 4.2 Normalized metallicity distribution functions of stars in the three selected regions and that of all the halo stars. This figure was constructed with Gaussian kernel density estimator using the A, F, G and K stars catalogued in LAMOST DR4, without the SAGA database. Note that the sharp cut-offs at high metallicity are due to our sample selection with [Fe/H]< -0.7 and that the histogram for the entire halo is multiplied by 1.5 for the visualization purpose.

Table 4.1. Properties of the four selected regions

Region ID	Name	# of stars		$\langle L_z \rangle \pm \sigma_{L_z}$		$\langle E \rangle \pm \sigma_E$		$\langle$[Fe/H]$\rangle \pm \sigma_{\text{[Fe/H]}}$
		SAGA	LAMOST	SAGA	LAMOST	SAGA	LAMOST	LAMOST
				$\times 10^3$kpc km s^{-1}	$\times 10^3$kpc km s^{-1}	$\times 10^5$km^2 s^{-2}	$\times 10^5$km^2 s^{-2}	
A	Innermost halo	161	8954	0.10 ± 0.17	0.12 ± 0.17	-1.71 ± 0.05	-1.70 ± 0.05	-1.16 ± 0.38
B	Gaia Enceladus	135	4222	-0.02 ± 0.27	-0.06 ± 0.26	-1.34 ± 0.13	-1.36 ± 0.11	-1.32 ± 0.33
C	high-E retrograde	26	299	-2.17 ± 0.48	-2.20 ± 0.52	-1.08 ± 0.14	-1.06 ± 0.15	-1.60 ± 0.33
D	...	10	70	2.14 ± 0.54	1.93 ± 0.35	-1.03 ± 0.17	-1.14 ± 0.12	-1.46 ± 0.47

In Figure 4.1, we show the distribution of stars with [Fe/H]< -0.7 in the SAGA database in the E–L_z plane. The contour was made using a Gaussian kernel density estimator. The upper panels show that the stellar kinematic properties vary with metallicity. At higher metallicity ([Fe/H]> -1.5; upper left panel), we see the signature of Gaia Enceladus/Sausage at $L_z \sim -500\,\mathrm{kpc\,km\,s^{-1}}$ and $E > -1.6 \times 10^5\,\mathrm{km^2\,s^{-2}}$ (Belokurov et al., 2018; Myeong et al., 2018c; Koppelman et al., 2018; Deason et al., 2018; Haywood et al., 2018; Helmi et al., 2018). Gaia Enceladus is interpreted as the result of dwarf galaxy accretion. As we move toward lower metallicity ([Fe/H]< -1.5), the Gaia Enceladus signature becomes weak (Belokurov et al., 2018; Myeong et al., 2018b). Instead, we see a clear enhancement of stars with retrograde motion. This metallicity difference between Gaia Enceladus and high-E retrograde halo stars seems consistent with Figure 2 of Myeong et al. (2018b), who noted that the excess of high-E retrograde stars extends down to [Fe/H]~ -1.9 while the diamond shape in the $L_z - E$ space, corresponding to Gaia Sausage/Enceladus, extends down to [Fe/H]~ -1.5.

The star distributions in LAMOST DR4 are similar to those in the SAGA database; the basic picture described above was confirmed by the LAMOST DR4 sample. Slight differences are attributable to the small number of stars in the SAGA database, the different metallicity distributions between the two samples, and/or the radial velocity and metallicity measurement quality. The SAGA database focuses on lower metallicity and has smaller uncertainties in radial velocity and metallicity measurements.

In the following chemical analysis, we compare the abundances of stars in the four regions in the E–L_z plane, shown by the rectangles in Figure 4.1 (see also Table 4.1). The first three regions in E–L_z are the innermost halo with small E and prograde motion (orange labeled as A), Gaia Enceladus with high E and low L_z (cyan; B), and the high-E retrograde stars (purple; C). The selection box C roughly corresponds to S1, Rg2, Rg3, Rg4, and Rg6 of Myeong et al. (2018d). [22] The last region, with a high E and prograde motion, was selected for the region C comparison (black; D). We note that results presented below are unchanged if we change the boundary L_z by a few $\times 100\,\mathrm{kpc\,km\,s^{-1}}$ or E by $\sim 10^4\,\mathrm{km^2\,s^{-2}}$ of the selection boxes.

4.3 Results

Figure 4.2 shows metallicity distributions of stars in the three regions from the LAMOST DR4 catalog. It is very clear that the three regions (A-C) have different metallicity distributions. The innermost halo (A) has the

[22] Since our analysis and that of Myeong et al. (2018d) are different, the comparison is not very precise. However, we note that we obtain similar L_z and E for ω Centauri ($-595\,\mathrm{kpc\,km\,s^{-1}}, -1.78 \times 10^5\,\mathrm{km^2\,s^{-2}}$) to their values ($-496\,\mathrm{kpc\,km\,s^{-1}}, -1.85 \times 10^5\,\mathrm{km^2\,s^{-2}}$).

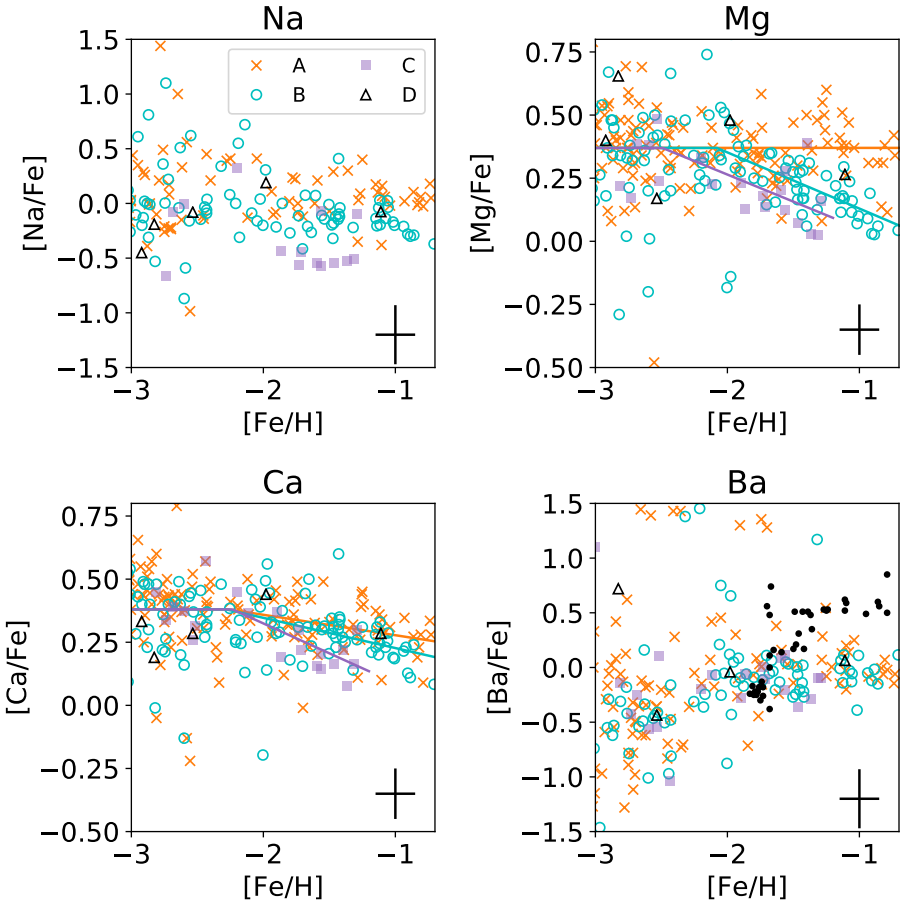

Figure 4.3 Chemical abundances of stars in the four regions for Na, Mg, Ca, and Ba. The data are taken from the SAGA database. Small black dots in the [Ba/Fe] panel are stars in ω Cen from Norris & Da Costa (1995). Regions A–C appear to occupy different positions in each of the three panels for Na, Mg and Ca. Note that the vertical scales for Na and Ba are different from the others. The lines in Mg and Ca panels show approximate chemical evolution of regions A–C. See Section 4.4 and Figure 4.4 for more details.

highest metallicity, while the retrograde substructure (C) has the lowest. In addition to this metallicity difference, we investigated abundance trends in detail in the following.

Figure 4.3 shows the chemical abundance trends of stars in the four regions for Na, Mg, Ca and Ba from the SAGA database; notably, data points that had only upper limits were excluded. This did not affect Na, Mg and Ca at [Fe/H]> -3.0 and only one star belonging to the innermost region was excluded ([Fe/H]$= -2.56$ and [Ba/Fe]< -1.32). When a star had multiple measurements for a given element, we simply took the average of the values for plotting.

It is known that there are two distinct chemical populations in the Galactic halo, namely high-/low-α populations (e.g., Nissen & Schuster, 2010). Nissen & Schuster (2010, 2011) showed that the high-α population has higher [X/Fe] for the three elements, Na, Mg, and Ca. Recent analyses of halo stars successfully associated the low-α population with the Gaia Enceladus from kinematics and chemical abundances of stars (e.g., Haywood et al., 2018; Helmi et al., 2018). This chemical abundance difference is understood as a result from slower star formation in the low-α population. This slower star formation leads to lower metallicity by the time of onset of type Ia supernovae.

Figure 4.3 confirms lower-α abundances of Gaia Enceladus (B) relative to the innermost halo population (A). A striking feature shown in the figure is that the retrograde substructure (C) does not follow either of the overall abundance trend of Gaia Enceladus or that of the innermost halo, with even lower [X/Fe] of the three elements on average than those of Gaia Enceladus at [Fe/H]$\gtrsim -2.0$. This indicates that the retrograde halo has a progenitor that is independent of the innermost halo or Gaia Enceladus. We further discuss the properties of the high-E retrograde halo stars in the next section from the perspective of chemical abundance.

Region D was selected for the comparison. It has the same range of E as high-E retrograde halo stars, but with prograde motion. Therefore, the region D provides us with estimates of the contribution of the "smooth" component of the halo to the region C. The region D does not have many stars at [Fe/H]> -2.5 as the region C, and a few stars with [Fe/H]> -2.5 have different abundances from most of the stars in the region C. This indicates that the high-E retrograde halo stars clusters in both kinematic (Myeong et al., 2018d,b) and chemical space and represents a distinct population.

For completeness, note that although we investigated other elements (C, Ti, Zn, Sr, Y, Ba, and Eu), we did not see significant differences among the regions, with Zn being an exception such that it might show a hint of possible abundance difference between high-E retrograde stars and Gaia Enceladus. Although the lacks of the difference may be partially due to insufficient precision of measured abundances, intrinsic abundance scatter of neutron capture elements, and/or abundance change during the stellar evolution, Ba

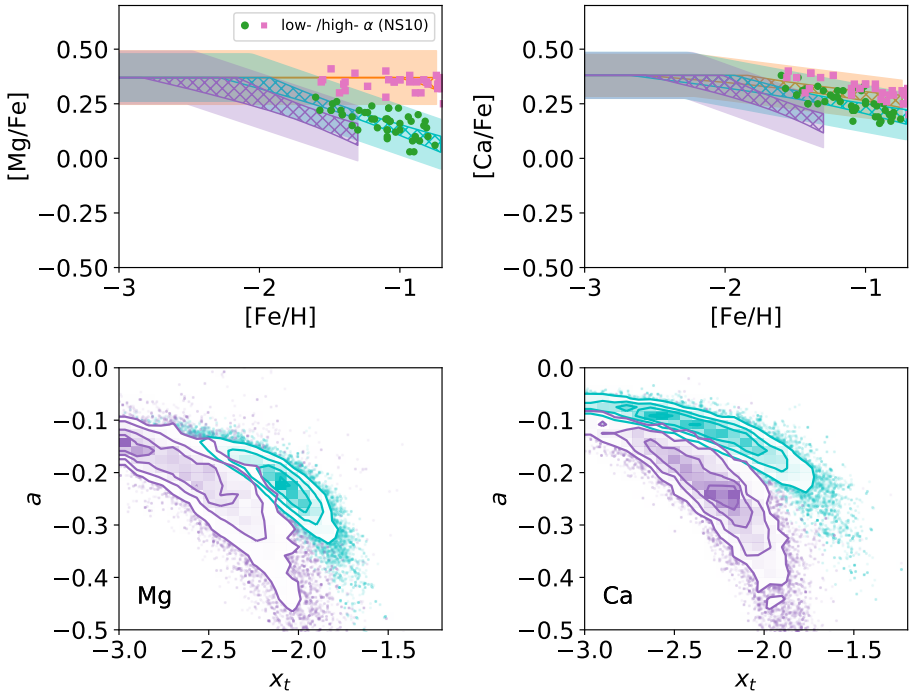

Figure 4.4 *upper panel*: Chemical abundance trends of stars in the three regions in the Milky Way halo for Mg and Ca. Colors for the three regions follow those in Figure 4.3. Halo stars from Nissen & Schuster (2010, 2011, ; green/salmon symbols corresponding to low-/high-α) are plotted for comparison purposes. *lower panel*: Posterior distributions of the obtained parameters for Gaia Enceladus and high-E retrograde halo stars. x_t denotes the metallicity at which [Mg/Fe] or [Ca/Fe] starts decreasing, and a denotes the slope of the trend at [Fe/H]$> x_t$ (see text and equations 4.1 and 4.4).

anomaly such as seen in ω Centauri (Norris & Da Costa, 1995) is clearly absent among the high-E retrograde stars (lower right panel of Figure 4.3).

4.4 Discussion

We approximated Mg and Ca abundance trends with the following form of function for chemical evolution (Figures 4.3 and 4.4),

$$f(x) = \begin{cases} y_0 & (x < x_t) \\ a(x - x_t) + y_0 & (x > x_t) \end{cases} \tag{4.1}$$

where x, y are for [Fe/H] and [X/Fe]. To obtain the set of parameters which describes the data best, we adopted the following likelihood,

$$p = \Pi_i \int f(\xi|[\mathrm{Fe/H}]_i, \sigma_{[\mathrm{Fe/H}]}) g([\mathrm{X/Fe}]_i|\xi, \mathbf{x}) \mathbf{d}\xi \tag{4.2}$$

where

$$f = \frac{1}{\sqrt{2\pi\sigma^2_{[\mathrm{Fe/H}]}}} \exp(-\frac{(\xi-[\mathrm{Fe/H}]_i)^2}{2\sigma^2_{[\mathrm{Fe/H}]}}) \tag{4.3}$$

$$\begin{aligned} g = \; & (1-f_o)\frac{1}{\sqrt{2\pi\sigma^2_{[\mathrm{X/Fe}]}}} \exp(-\frac{([\mathrm{X/Fe}]_i - f(\xi))^2}{2\sigma^2_{[\mathrm{X/Fe}]}}) \\ & + f_o \frac{1}{\sqrt{2\pi(\sigma^2_{[\mathrm{X/Fe}]}+\sigma_b^2)}} \exp(-\frac{([\mathrm{X/Fe}]_i-\mu_b)^2}{2(\sigma^2_{[\mathrm{X/Fe}]}+\sigma_b^2)}). \end{aligned} \tag{4.4}$$

f_o, μ_b, and σ_b are outlier fraction, mean and standard deviation for the outlying population. We estimated a set of parameters $(a, x_t, \sigma_{[\mathrm{X/Fe}]}, f_o, \mu_b, \sigma_b)$ using MCMC sampling while fixing y_0 and $\sigma_{[\mathrm{Fe/H}]}$. The mean [X/Fe] in $-3.0 <$[Fe/H]< -2.5 were adopted as y_0 (0.37 for Mg and 0.38 for Ca) and $\sigma_{[\mathrm{Fe/H}]} = 0.15$ was adopted. Flat priors with sufficiently wide ranges were adopted for the parameters except for x_t $(-3 < x_t < -1)$ and f_0 $(0 < f_0 < 0.5)$.

Posterior distributions for a and x_t are shown in the lower panels of Figure 4.4. The posterior distributions show that Gaia Enceladus and high-E retrograde stars are fit with different sets of parameters. The σ_X result in comparable to the estimated errors ($\sigma_{[\mathrm{Mg/Fe}]} = 0.12$, 0.11, and 0.12 and $\sigma_{[\mathrm{Ca/Fe}]} = 0.10$, 0.11, and 0.10 for regions A, B, and C respectively), indicating abundance spread of each region is smaller than or comparable to the estimated errors. We note that f_0 converge between $0.10 - 0.20$ for the regions A and B, and < 0.10 for the region C.

The best models are shown in Figure 4.3 and the upper panels of 4.4. The widths of the shaded areas correspond to $\sigma_{[\mathrm{X/Fe}]}$ and $\sigma_{[\mathrm{Fe/H}]}$ and the hatched areas correspond to 1σ regions of the best fit model (equation 4.1). Also shown in Figure 4.4 are "low-α" and "high-α" populations of Nissen & Schuster (2010, 2011). Note that we did not include region D in the following analysis, as it is not associated with main features in the E–L_z plane.

Figure 4.4 confirms that our innermost halo and Gaia Enceladus stars correspond to the high-/low-α populations of Nissen & Schuster (2010), respectively. The general interpretation of the two populations is that the high-α population experienced more intense star formation prior to the onset of type Ia supernovae. To achieve such a high star formation rate at the early phase, the high-α population is usually considered to have formed in a massive galaxy, probably the Milky Way itself, although the detailed process is still under debate (e.g., Fernández-Alvar et al., 2018; Mackereth et al., 2018). On the other hand, the low-α population of Nissen & Schuster (2010)

is now considered to be an accreted dwarf galaxy (Gaia Enceladus) from chemical abundances and kinematics (e.g., Helmi et al., 2018; Belokurov et al., 2018; Haywood et al., 2018).

Figure 4.4 also shows that the [X/Fe] ratios in the high-E retrograde halo stars are even lower for the two elements than the two halo populations in Nissen & Schuster (2010) at [Fe/H]$\gtrsim -2$. High-energy retrograde halo stars has been enriched only up to [Fe/H]~ -2.5 by the time of onset of type Ia supernovae, which indicates slow star formation.

The slow star formation indicated from the very low-α element abundances suggests very inefficient star formation, which would suggest a low mass progenitor. The mass ratio between the progenitor of the high-E retrograde halo stars and Gaia Enceladus was estimated by their metallicity distribution functions (Figure 4.2). The mean metallicity of Gaia Enceladus is ~ -1.3, and that of the high-E retrograde halo stars is ~ -1.6. The mass-metallicity relation of Kirby et al. (2013) for dwarf galaxies suggests that this 0.3 dex difference corresponds to a factor of ~ 10 stellar mass difference.

Considering this large mass ratio, the impact of the accretion of the progenitor of the high-E retrograde halo stars to Milky Way is likely to be much smaller than that of Gaia Enceladus. However, such a small system is still detectable by kinematics (Myeong et al., 2018b) and addition of chemical abundance information brings us robust conclusion and tells us the property of the progenitor. Note that we did not find many stars in the SAGA database that are similar in chemical abundances, but not in kinematics, to stars in the high-E retrograde halo stars. Therefore, the high-E retrograde halo stars would be a unique contributor to the Milky Way stellar halo.

Myeong et al. (2018d) discussed a possible connection of some of their high-energy retrograde substructures with ω Centauri. The abundance pattern of the high-E retrograde halo stars is different from the stellar chemical abundances in the globular cluster reported by Johnson & Pilachowski (2010); they reported almost flat α-element abundances up to [Fe/H]~ -1 for ω Centauri. This difference as well as the lack of Ba abundance anomalies (lower right panel of Figure 4.3) indicates that the majority of the high-E retrograde halo stars is unrelated to ω Centauri.

Considering that we only used a compilation of past abundance measurements, which can be affected by systematic uncertainties, sufficient precision could be achieved in large spectroscopic surveys with a well-calibrated analysis if the surveys are designed well to study metal-poor stars. Indeed, we have reached a consistent conclusion for Mg using APOGEE DR14 data (Holtzman et al., 2015). However, other elements in APOGEE do not show as clear differences as Mg. This is due to the limitations of the current surveys in terms of the number of halo stars and the accuracy of chemical abundance measurements for metal-poor stars; additionally, it highlights the need for high-resolution spectroscopic surveys designed specifically to study

halo stars.

4.5 Summary

Based on chemical abundances and kinematics from the SAGA database and Gaia DR2, we added new evidence that the excess of stars with highly-retrograde orbits at high energy is caused by an accretion of a dwarf galaxy which is different from Gaia Enceladus/Sausage. Compared to previous studies that have pointed out or investigated the excess with stellar kinematics and metallicity (Helmi et al., 2017; Myeong et al., 2018b,d), we included α-element abundances in the investigation. The α-element abundances are even lower than the low α-element abundances of Gaia Enceladus, suggesting a different and lower mass progenitor. Although there are studies that pointed out stars with large retrograde motion have low α-element abundances (Venn et al., 2004; Stephens & Boesgaard, 2002), these studies were in the pre-Gaia era, and hence our study is new in that it used the latest most precise kinematics from Gaia astrometric measurements and discussed the population in connection with a recently identified accretion signature in the Galaxy.

This work demonstrates that chemical abundances can reveal the origin of kinematically identified substructures in the Milky Way. Neither chemical abundance or kinematics alone would not be possible to provide evidence as solid as their combination in this Chapter. It presents evidence for an accretion event that is independent of Gaia Enceladus, providing insights about the Milky Way merging history.

acknowledgements

We thank Timothy C. Beers and Kohei Hattori for their helpful suggestions and comments on the study presented in this Chapter.

Chapter 5

High-resolution spectroscopy and asteroseismology of halo stars with kinematics

In the previous Chapter, we have investigated the halo formation history from stellar kinematics and chemical abundances. This chapter explores the possibility of obtaining additional clues by taking into account stellar age information using asteroseismology. The results of Chapter 3 have to be kept in mind when we interpret stellar ages from asteroseismology in this chapter; a small fraction of stars exists whose ages cannot be estimated properly despite the lack of abundance anomaly because of binary interaction. Even though our study is still in the exploratory phase of applying asteroseismology to halo stars, and despite the caution we provided from Chapter 3, we constrain halo formation timescale from the results of this chapter. This opens a new window to reveal the halo formation history over a wide volume with stellar ages and chemical abundances.

5.1 Summary and context

This chapter presents a pioneering work showing that chemical abundances, stellar kinematics, and stellar ages can be combined for distant red giant stars in the *Kepler* field using asteroseismology to study the Milky Way halo stellar populations. Nissen & Schuster (2010, 2011) and Schuster et al. (2012) combined these three types of information for halo turn-off stars in the solar neighbourhood. They showed that halo stars are clearly divided into two sub-populations based on α-element abundances and that these chemically defined two populations also differ in stellar kinematics and stellar age distributions. While the low-α population tends to be younger, on retrograde orbit, and with large vertical excursion, indicating accretion origin, the high-α population seems to have formed in-situ. We extend these

studies beyond the solar neighbourhood by using asteroseismology. Based on mass estimates provided from asteroseismology, we constrain the formation timescales and formation epochs for the halo stellar populations.

There are recent progresses in understandings of the two major halo populations thanks to the Gaia mission. Recent studies revealed that the low-α population corresponds to a relatively massive accreted dwarf galaxy, Gaia-Enceladus (Helmi et al., 2018; Mackereth et al., 2019) and that the high-α population could have been disk stars heated to the halo by the gravity of a massive accreted dwarf galaxy (e.g., Bonaca et al., 2017; Haywood et al., 2018; Di Matteo et al., 2018; Belokurov et al., 2019). Considering the large spatial extent of the halo, it is desired to expand the combination of abundances, kinematics, and age to a greater distance from Nissen & Schuster (2010, 2011) and Schuster et al. (2012). Although we are able to determine age of turn-off stars thorough isochrone fitting, we need age of red giant stars since turn-off stars are intrinsically much fainter than giants.

Age of red giants can be estimated with their mass measurements. Asteroseismology opened a window to estimate masses for a large number of red giant stars. Although asteroseismology has been applied to disk stars to study the Galactic disk evolution, its application to the halo has been limited because of the reliability of asteroseismology at low metallicity and the difficulty in finding halo stars with asteroseismic information.

A large systematic offset in asteroseismic mass measurements have been reported for low-metallicity stars if simple scaling relations are used (Epstein et al., 2014; Casey et al., 2018). Corrections to the scaling relations have been suggested based on theoretical modeling of stellar structure and stellar oscillations. Miglio et al. (2016) and Valentini et al. (2019) analysed metal-poor stars in a globular cluster and in the field, respectively, and reported that asteroseismology can derive masses without offset even for low-metallicity stars if the corrections are used. These studies suggest that asteroseismology can be useful for the study of stellar ages of halo stars.

Our study is the first application of asteroseismology to a relatively large number (26) of halo stars. We overcome the difficulty in the sample selection by utilizing spectroscopic surveys and validate this selection through analyses of stellar kinematics using Gaia DR2. Based on oscillation frequencies measured in literatures and stellar parameters derived through our line-by-line differential abundance analysis, we estimate mass of the halo stars. The derived masses are still systematically more massive than the expected value despite the use of corrections. While there seems mass spread among our halo stars, the scatter can fully be explained by measurement uncertainties if we exclude most luminous giants and core He burning stars. The lack of significant scatter over measurement errors indicates that the halo formation occurred within a timescale of 2 Gyr.

Precise chemical abundances allow us to separate our program stars into low-α and high-α halo populations. For the low-α population, we find the

presence of type Ia supernova contribution and the lack of main s-process contribution in its chemical evolution. These give a constraint on its star formation timescale as $100 - 300\,\mathrm{Myr}$. The star formation of the high-α population seems have proceeded with a shorter timescale than the low-α population. The mass estimates provide limits on the formation epoch difference between the two populations as $< 4\,\mathrm{Gyr}$.

We also find peculiar stars in our sample. One class of them is three Na-enhanced stars. We show that they show similar mass to other halo stars, indicating binary interaction or internal nucleosynthesis is not responsible for the Na enhancements. Although the O abundance might be low for the two Na-enhanced stars, which indicates globular cluster origin, additional abundance measurements for light elements are needed for more robust conclusion. Another class is two over-massive stars. These stars have significantly larger mass than other halo stars. Their chemical abundances are normal in most of the elements. Even though our data do not suggest radial velocity variation of these stars, these could be similar objects to young α-rich stars studied in Chapter 3.

Our work demonstrates that asteroseismology seems a promising tool to study age of distant halo stars as long as we exclude most luminous giants and core-He burning stars. Our study encourages future studies of halo stars with asteroseismology with ongoing/coming space telescopes. Further improvements in theoretical modelling of stellar oscillations would also bring benefits since they would resolve the systematic offset and would allow us to use currently excluded stars.

The importance of this work in the context of this thesis is that it provides constraint on the timescales and epochs of formation for the two chemically defined stellar subpopulations in the halo.

This work is in preparation for publication. The entire Table 5 and Table 7 are provided online.

5.2 Observation

5.2.1 Target selection

Targets are selected from LAMOST DR4 and APOKASC2 catalogs based on radial velocity and metallicity measurements (Figure 5.1). To make sure all the targets have frequency measurements, we only select stars in the catalog of asteroseismic analysis of ∼16,000 red giants by Yu et al. (2018). Selection criteria are determined to minimize the contamination of disk stars based on the distributions of disk and halo stars in a mock catalog of *Kepler* field generated from Besançon galaxy model (Robin et al., 2003). We note that some stars do not satisfy the criteria; since our observing condition was not necessarily perfect, we had to loosen our criteria during the observation. Two stars (KIC5858947 and KIC9696716) are included as a result.

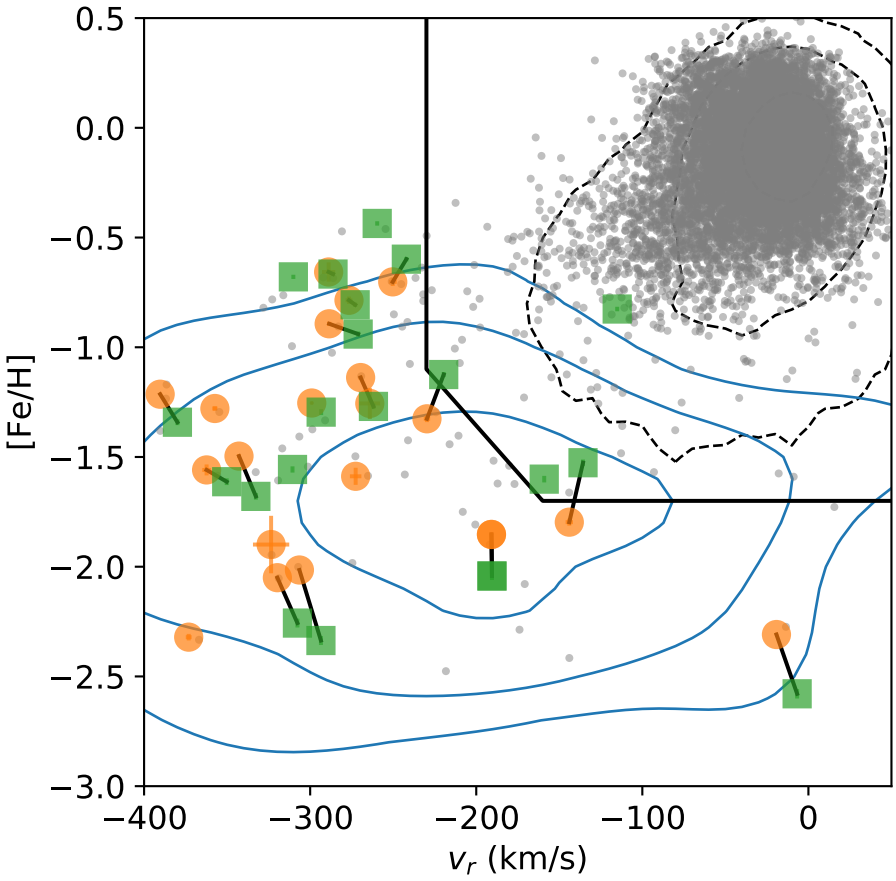

Figure 5.1 Target selection in the radial velocity – [Fe/H] plane. The contours are disk (black dashed) and halo (blue solid) stars in Besançon model (each contour contains 39.3, 86.5, and 98.9 % of the population.). Stars outside of the black solid line are selected as halo star candidates. Targets are shown with orange circles (LAMOST DR5) and green squares (APOKASC2). If a target is both in LAMOST DR5 and APOKASC2, two points are connected by a black line. Grey points are all the stars that are both in Yu et al. (2018) and in LAMOST DR5. Note that while LAMOST DR4 was used at the time of selection, here we use updated measurements in LAMOST DR5.

Table 5.1. Observation log

Object	Date[a]	Exposure (s)	S/N[b]	V_r (HDS) (km s^{-1})	$V_{r,L}$[c] (km s^{-1})	[Fe/H]$_{\rm L}$[c]	$V_{r,A}$[d] (km s^{-1})	[Fe/H]$_{\rm A}$[d]	$V_{r,G}$[e] (km s^{-1})	$\sigma(V_{r,G})$[e] (km s^{-1})	M_G[e] (mag)
KIC5184073	July 11, 2018	5400	107.0	-136.21	-143.97	-1.80	-135.71	-1.53	···	···	13.21
KIC5439372	July 10, 2018	1200	135.0	-213.57	···	···	-211.21	NaN	-212.89	0.58	11.82
KIC5446927	August 4, 2017	1200	115.0	-272.89	-276.62	-0.79	-272.91	-0.81	-272.90	0.39	11.71
KIC5698156	July 9 & 11, 2018	1200	246.0	-380.25	-390.31	-1.21	-379.93	-1.34	-379.28	0.72	10.45
KIC5858947	July 10, 2018	1800	135.0	-104.35	···	···	-115.13	-0.83	-106.91	2.09	11.72
KIC5953450	July 11, 2018	2400	265.0	-286.53	-288.88	-0.66	-286.24	-0.67	-284.63	0.82	12.67
KIC6279038	July 9, 2018	2200	118.0	-308.10	-319.75	-2.05	-307.67	-2.26	-308.15	0.75	12.43
KIC6520576	July 11, 2018	5400	171.0	-365.09	-373.14	-2.32	···	···	···	···	13.18
KIC6611219	July 11, 2018	1800	113.0	-293.95	···	···	-293.38	-1.30	-293.47	0.72	12.06
KIC7191496	August 2, 2017	1200	167.0	-290.55	-306.47	-2.02	-293.52	-2.34	-297.34	1.58	11.82
KIC7693833	August 2, 2017	1200	179.0	-7.10	-19.24	-2.31	-6.79	-2.58	-6.69	0.44	11.74
KIC7948268	July 9, 2018	2200	155.0	-292.58	-299.04	-1.25	···	···	-290.87	1.79	12.44
KIC8350894	July 11, 2018	3600	198.0	-219.94	-229.68	-1.33	-219.59	-1.12	-219.83	1.61	12.76
KIC9335536	July 10, 2018	5400	114.0	-350.52	-362.36	-1.56	-350.24	-1.61	-351.49	1.21	12.97
KIC9339711	July 9, 2018	1800	178.0	-332.81	-342.85	-1.50	-332.69	-1.68	-332.68	0.56	12.08
KIC9583607	July 10, 2018	2400	169.0	-309.74	···	···	-310.12	-0.68	-309.86	0.37	11.46
KIC9696716	July 9, 2018	1200	171.0	-146.71	···	···	-159.06	-1.60	-148.23	4.28	11.73
KIC10083815	August 4, 2017	1800	136.0	-270.98	-288.56	-0.89	-271.10	-0.94	-270.22	1.08	12.26

Table 5.1 (cont'd)

Object	Date[a]	Exposure (s)	S/N[b]	V_r (HDS) (km s^{-1})	$V_{r,L}$[c] (km s^{-1})	[Fe/H]$_{\rm L}$[c]	$V_{r,A}$[d] (km s^{-1})	[Fe/H]$_{\rm A}$[d]	$V_{r,G}$[e] (km s^{-1})	$\sigma(V_{r,G})$[e] (km s^{-1})	M_G[e] (mag)
KIC10096113	July 11, 2018	4800	160.0	-241.44	-250.28	-0.70	-242.08	-0.60	-240.37	2.64	13.21
KIC10328894	July 9, 2018	3600	188.0	-315.65	-323.52	-1.90	···	···	-316.37	1.89	13.02
KIC10460723	August 2, 2017	1800	152.0	-346.84	-357.37	-1.28	···	···	-347.34	0.62	12.32
KIC10737052	July 11, 2018	5400	200.0	-242.77	-264.09	-1.26	···	···	-237.99	1.04	13.20
KIC10992126	July 10, 2018	1200	142.0	-259.55	···	···	-259.64	-0.44	-259.84	0.41	10.85
KIC11563791	July 11, 2018	600	164.0	-262.45	-269.62	-1.14	-261.90	-1.27	-262.20	0.46	10.95
KIC11566038	July 10, 2018	1800	122.0	-310.67	···	···	-310.63	-1.56	-309.94	2.11	12.04
KIC12017985	August 2, 2017	600	225.0	-190.84	-190.84	-1.85	-190.54	-2.04	-184.34	2.03	10.14
	July 9, 2018	600	202.0	-190.24							
KIC12253381	July 9, 2018	2200	121.0	-272.44	-272.61	-1.59	···	···	-261.64	1.20	12.51

[a]Observations in 2017 are conducted with $R \sim 60,000$, while those in 2018 are with $R \sim 80,000$.

[b]S/N are measured from continuum around 5765 Å per 0.024 Å pixel.

[c]From LAMOST DR5 catalog.

[d]From APOGEE DR14 catalog.

[e]From Gaia DR2 catalog.

5.2.2 Observation

Observation was conducted with the High Dispersion Spectrograph (HDS; Noguchi et al., 2002) on the Subaru telescope. Most of the targets were observed in July 2018, during which we occasionally had thin clouds. Spectra were taken with a standard setup of HDS with 2x2 CCD binning which covers from $\sim$ 4000 Å to $\sim$ 6800, Å (StdYd). Image slicer #2 was used to achieve high signal-to-noise ratio (S/N) with $R \sim 80,000$ (Tajitsu et al., 2012). Subset of spectra were taken in 2017 as a back-up program for another proposal when the sky was covered with thin clouds. These spectra were taken with the same wavelength coverage but with $R \sim 60,000$ without the image slicer. KIC12017985 was observed both in 2017 and in 2018 to confirm the consistency of our analysis. We mainly adopt parameters from the 2018 observation in figures for this star, and denote the 2017 observation as KIC 12017985–17. We note that KIC10992126 was observed but not included in the following analysis, since it turned out to have large errors in the measured frequencies.

Spectra are reduced with an IRAF script, `hdsql`. The S/N is estimated from a continuum region around 5765 Å and radial velocity is estimated from wavelengths of iron lines. Details of the observation are shown in Table 5.1.

The uncertainty in radial velocity measurements is estimated to be $1\,\mathrm{km\,s^{-1}}$ considering the stability of the instrument. KIC5439372, KIC5858947, KIC7191496, KIC9696716 show signatures of radial velocity variation between APOGEE and our observation, suggesting the possibility of the existence of binary companions. Most of these stars show large uncertainties in Gaia radial velocity for their magnitude, which supports presence of the variation. In addition, KIC10737052, KIC12017985 and KIC12253381 show large offset between our observation and Gaia measurements, which suggests binarity of these objects.

5.3 Asteroseismology

Table 5.2. Asteroseismic parameters, mass, and radius

Object	νmax[a] (μHz)	$\sigma_{(\nu_{\rm max})}$[a] (μHz)	$\Delta\nu$[a] (μHz)	$\sigma_{(\Delta\nu)}$[a] (μHz)	Evo. stage[a]	M ($M_\odot$)	$\sigma_{(M)}$ ($M_\odot$)	R ($R_\odot$)	$\sigma_{(R)}$ ($R_\odot$)	$M_{\rm sc}$ ($M_\odot$)
KIC5184073	9.25	0.22	1.659	0.031	RGB	0.78	0.08	16.79	0.69	0.92
KIC5439372	6.39	0.22	1.186	0.054	RGB	0.97	0.22	22.53	2.37	1.17
KIC5446927	21.88	0.38	2.874	0.048	RC	1.49	0.13	14.95	0.58	1.44
KIC5698156	9.73	0.31	1.677	0.031	RGB	0.76	0.11	16.35	0.94	0.95
KIC5858947	168.93	0.89	14.533	0.019	RGB	0.98	0.05	4.36	0.09	1.01
KIC5953450	140.87	0.83	12.715	0.021	RGB	0.99	0.05	4.81	0.10	1.01
KIC6279038	5.59	0.28	1.018	0.047	RGB	1.18	0.34	26.53	3.32	1.42
KIC6520576	17.91	0.50	2.693	0.016	unknown	0.94	0.11	13.18	0.64	0.99
KIC6611219	6.96	0.21	1.330	0.028	RGB	0.70	0.10	18.55	1.13	0.88
KIC7191496	16.23	0.24	2.455	0.021	RGB	0.88	0.06	13.50	0.35	1.04
KIC7693833	31.73	0.32	4.046	0.014	RGB	1.03	0.05	10.34	0.19	1.11
KIC7948268	120.45	0.82	11.450	0.015	RGB	0.93	0.03	5.03	0.07	0.97
KIC8350894	12.69	0.29	2.005	0.024	RGB	0.90	0.08	15.48	0.56	1.09
KIC9335536	11.08	0.82	1.861	0.095	RGB	0.85	0.28	15.87	2.17	1.03
KIC9339711	20.51	0.31	2.825	0.019	RGB	1.05	0.07	13.07	0.36	1.21
KIC9583607	25.25	0.51	3.816	0.055	RC	0.76	0.05	9.94	0.25	0.71
KIC9696716	24.09	0.53	3.305	0.022	RGB	0.93	0.07	11.31	0.34	1.06
KIC10083815	17.99	0.38	2.605	0.015	RGB	0.91	0.07	13.07	0.39	1.08
KIC10096113	36.31	0.59	4.168	0.042	RC	1.44	0.10	11.50	0.32	1.42

Table 5.2 (cont'd)

Object	νmax[a] (μHz)	$\sigma_{(\nu_{\max})}$[a] (μHz)	$\Delta\nu$[a] (μHz)	$\sigma_{(\Delta\nu)}$[a] (μHz)	Evo. stage[a]	M ($M_\odot$)	$\sigma_{(M)}$ ($M_\odot$)	R ($R_\odot$)	$\sigma_{(R)}$ ($R_\odot$)	$M_{\rm sc}$ ($M_\odot$)
KIC10328894	30.72	0.40	3.965	0.016	RGB	0.97	0.05	10.20	0.20	1.07
KIC10460723	22.97	0.45	3.146	0.013	RC	1.09	0.07	12.56	0.29	1.10
KIC10737052	26.57	0.40	3.518	0.017	RC	1.10	0.04	11.72	0.18	1.11
KIC11563791	43.03	0.51	5.005	0.019	RGB	1.02	0.05	8.86	0.18	1.15
KIC11566038	31.36	0.32	3.954	0.023	RGB	1.03	0.05	10.43	0.22	1.15
KIC12017985	18.24	0.29	2.620	0.018	RGB	1.00	0.06	13.54	0.35	1.15
KIC12017985-17						0.99	0.06	13.48	0.34	1.15
KIC12253381	22.00	0.40	3.032	0.014	RGB	0.96	0.06	12.07	0.30	1.12

[a]From Yu et al. (2018).

All the targets are in Yu et al. (2018) catalog. They provided results of asteroseismic analysis of red giant stars using ∼4 years photometric data in the *Kepler* field using the SYD asteroseismic pipeline. The long base line enabled them to derive various properties of the stars including $\nu_{\rm max}$, $\Delta\nu$, and evolutionary status. Although they also derived mass and radius, their stellar parameters are based on collection of values from various literatures. Therefore, those mass and radius have to be revised using updated stellar parameters from our analysis of high-resolution spectra.

We derive mass and radius using `Asfgrid` (Sharma et al., 2016), which includes a correction to the $\Delta\nu$ scaling relation taking into account evolutionary status. The other necessary input parameters, $T_{\rm eff}$ and [Fe/H], are taken from our spectroscopic measurements in Section 5.5.

In Table 5.2, we also provide mass obtained from simple scaling relations. It is clear that the effect of correction is not negligible.

Masses of metal-poor turn-off stars have been estimated to be $\sim 0.8\,{\rm M}_\odot$ (e.g., Meléndez et al., 2010). We expect similar masses for our sample, since the time scale of the evolution after the turn-off is very short. Two stars are obviously more massive than others, which would be treated as outliers (KIC5446927 and KIC10096113). The weighted average of the masses excluding these two is $0.96 \pm 0.01\,{\rm M}_\odot$ (error of mean). Although this value is closer to the expected mass than that of masses from simple scaling relations ($1.03 \pm 0.01\,{\rm M}_\odot$), it is still significantly higher. More discussion is presented in Section 5.6.2.

Four stars in our sample are common with Epstein et al. (2014), which are re-analysed by Valentini et al. (2019), who uses frequencies derived with COR asteroseismic pipeline and a Bayesian approach for mass (and age) estimation. We compare our derived masses with Valentini et al. (2019) for the four stars in Figure 5.2. There is a good agreement between our study and Valentini et al. (2019). Although we derive slightly higher mass for two stars (KIC12017985 and KIC11563791), the difference is not with high significance. Figure 5.2 also includes masses that are derived in the way we adopt in this study but with frequencies provided in Valentini et al. (2019). The agreement for KIC12017985 and KIC11563791 becomes better, indicating the difference would be due to the use of different pipelines for frequency analysis. Since systematic offsets in measured frequencies should not depend on stellar metallicity, further discussions on the effect of asteroseismic pipelines are beyond the scope of this study. Such discussion is provided in Pinsonneault et al. (2018). We note that they quantified the systematic $\nu_{\rm max}$ or $\Delta\nu$ differences between COR and SYD pipelines as $\sim 1\%$ at most.

5.4 Kinematics

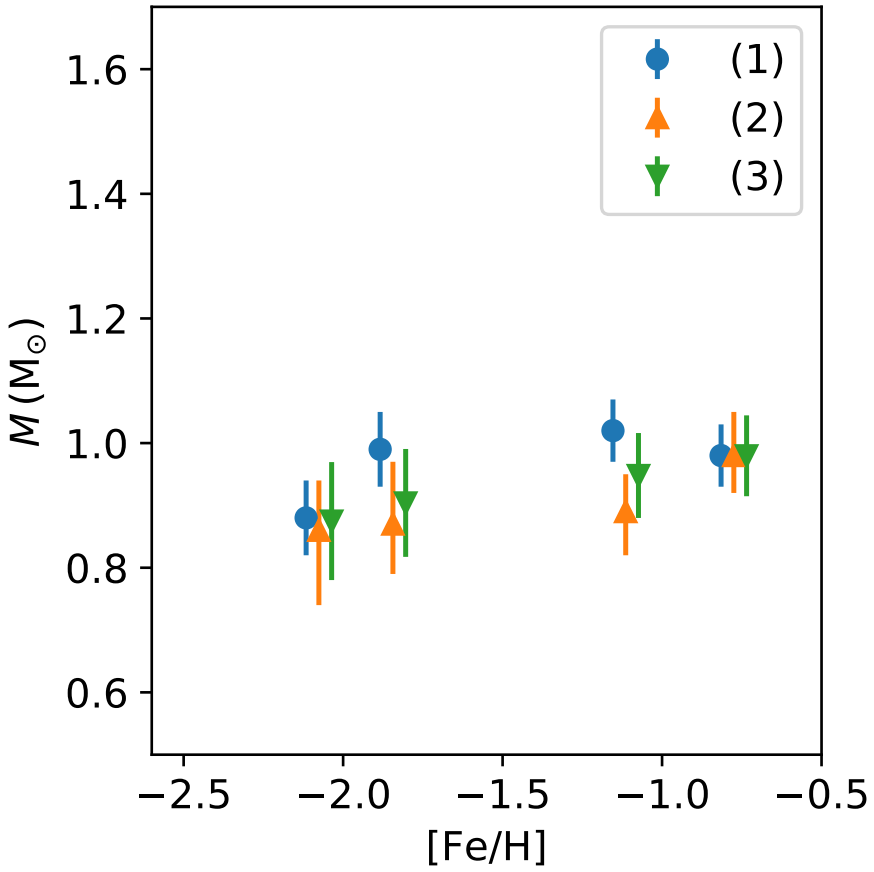

Figure 5.2 Comparison of derived masses with Valentini et al. (2019) for four stars (KIC7191496, KIC12017985, KIC11563791, and KIC5858947, from left to right). Each star has three data points: (1) the mass derived in this work, (2) the mass derived in Valentini et al. (2019), and (3) the mass derived with our method but with $\nu_{\rm max}$ and $\Delta\nu$ values provided in Valentini et al. (2019). Data points are horizontally shifted for visualization purpose.

Table 5.3. Parallax and extinction

Object	$\pi_{\rm Gaia}$ (mas)	$\sigma_{(\pi_{\rm Gaia})}$ (mas)	$\pi_{\rm seis}$ (mas)	$\sigma_{(\pi_{\rm seis})}$ (mas)	Choice [a]	$E(B-V)$[b] (mag)
KIC5184073	0.117	0.015	0.202	0.010	S	0.06
KIC5439372	0.289	0.020	0.273	0.030	G	0.06
KIC5446927	0.331	0.029	0.377	0.016	S	0.06
KIC5698156	0.663	0.024	0.774	0.047	G	0.06
KIC5858947	1.156	0.028	1.277	0.047	G	0.07
KIC5953450	0.791	0.025	0.754	0.027	G	0.06
KIC6279038	0.145	0.027	0.178	0.024	S	0.04
KIC6520576	0.202	0.013	0.231	0.012	S	0.05
KIC6611219	0.272	0.025	0.333	0.021	S	0.06
KIC7191496	0.424	0.019	0.421	0.013	S	0.05
KIC7693833	0.636	0.024	0.593	0.016	S	0.11
KIC7948268	0.762	0.024	0.747	0.018	S	0.04
KIC8350894	0.193	0.020	0.259	0.011	S	0.05
KIC9335536	0.203	0.015	0.235	0.034	G	0.05
KIC9339711	0.415	0.020	0.403	0.013	S	0.07
KIC9583607	0.570	0.024	0.627	0.016	S	0.04
KIC9696716	0.429	0.025	0.505	0.018	S	0.04
KIC10083815	0.367	0.026	0.410	0.018	S	0.07
KIC10096113	0.280	0.015	0.322	0.012	S	0.19
KIC10328894	0.271	0.014	0.301	0.007	S	0.05
KIC10460723	0.370	0.020	0.363	0.011	S	0.04
KIC10737052	0.255	0.013	0.262	0.006	S	0.06
KIC11563791	0.975	0.025	0.950	0.029	G	0.05
KIC11566038	0.495	0.020	0.472	0.013	S	0.04
KIC12017985	0.799	0.027	0.887	0.028	G	0.04
KIC12017985-17	0.799	0.027	0.891	0.027	S	0.04
KIC12253381	0.354	0.023	0.343	0.010	S	0.04

[a]S: Parallax from asteroseismology. G: Gaia parallax

[b]Obtained from the relation $E(B-V) = 0.884\alpha$, which is provided in Green et al. (2018).

Table 5.4. Kinematic properties

Object	v_R ($\mathrm{km\,s^{-1}}$)	$\sigma_{(v_R)}$ ($\mathrm{km\,s^{-1}}$)	v_ϕ ($\mathrm{km\,s^{-1}}$)	$\sigma_{(v_\phi)}$ ($\mathrm{km\,s^{-1}}$)	v_z ($\mathrm{km\,s^{-1}}$)	$\sigma_{(v_z)}$ ($\mathrm{km\,s^{-1}}$)	$z_{\max}$ (kpc)	$\sigma_{(z_{\max})}$ (kpc)	$r_{\max}$ (kpc)	$\sigma_{(r_{\max})}$ (kpc)	e	$\sigma_{(e)}$
KIC5184073	143.4	4.6	94.3	3.0	-107.0	3.6	5.97	0.59	10.5	0.2	0.59	0.01
KIC5439372	-33.7	5.6	-2.8	1.6	110.3	8.5	6.51	0.79	8.0	0.1	0.93	0.04
KIC5446927	-137.7	8.2	-21.9	2.2	-72.1	1.2	3.99	0.04	9.7	0.2	0.89	0.00
KIC5698156	43.9	1.8	-137.0	1.2	-27.9	1.5	0.62	0.03	8.1	0.0	0.42	0.01
KIC5858947[a]	-161.5	4.3	95.4	1.3	8.8	0.7	0.52	0.10	10.6	0.1	0.70	0.01
KIC5953450	298.9	6.7	-0.4	1.1	-12.8	1.2	1.92	1.15	18.7	0.7	0.99	0.01
KIC6279038	-17.3	11.8	-76.3	1.7	22.7	10.3	1.39	0.59	8.4	0.3	0.67	0.01
KIC6520576	-81.6	7.5	-89.8	3.6	-123.5	2.8	5.13	0.30	9.3	0.2	0.56	0.02
KIC6611219	-240.3	17.6	-33.0	6.0	-24.8	1.4	0.91	0.04	14.0	1.2	0.92	0.02
KIC7191496	40.0	0.8	-42.8	1.0	-51.7	0.5	1.21	0.04	8.2	0.0	0.82	0.00
KIC7693833	63.2	2.1	240.6	1.0	-1.0	0.4	0.37	0.01	10.2	0.1	0.19	0.01
KIC7948268	118.8	1.3	-40.1	1.1	-20.3	1.3	0.59	0.01	9.1	0.0	0.85	0.00
KIC8350894	-149.1	7.3	50.4	3.7	-46.4	0.7	3.75	0.10	10.2	0.3	0.82	0.01
KIC9335536	227.0	6.5	-192.8	9.8	105.5	10.1	5.80	1.19	20.3	2.2	0.66	0.01
KIC9339711	52.6	0.4	-61.9	1.0	-153.0	2.5	7.22	0.10	8.6	0.0	0.49	0.01
KIC9583607	-131.0	4.8	-83.6	1.0	22.5	2.5	0.70	0.08	9.6	0.1	0.71	0.00
KIC9696716	-109.2	4.5	105.8	1.3	-48.6	0.6	1.32	0.03	9.3	0.1	0.61	0.00
KIC10083815	336.3	12.3	-50.5	5.2	-60.1	0.7	8.18	1.16	26.0	2.5	0.94	0.00
KIC10096113	-48.4	2.2	22.3	1.5	-56.7	0.9	3.89	0.09	8.6	0.0	0.90	0.01

Table 5.4 (cont'd)

Object	v_R ($\mathrm{km\,s^{-1}}$)	$\sigma_{(v_R)}$ ($\mathrm{km\,s^{-1}}$)	v_ϕ ($\mathrm{km\,s^{-1}}$)	$\sigma_{(v_\phi)}$ ($\mathrm{km\,s^{-1}}$)	v_z ($\mathrm{km\,s^{-1}}$)	$\sigma_{(v_z)}$ ($\mathrm{km\,s^{-1}}$)	$z_{\max}$ (kpc)	$\sigma_{(z_{\max})}$ (kpc)	$r_{\max}$ (kpc)	$\sigma_{(r_{\max})}$ (kpc)	e	$\sigma_{(e)}$
KIC10328894	-39.4	2.2	-81.5	0.9	11.4	2.2	0.97	0.02	8.3	0.0	0.65	0.00
KIC10460723	103.8	1.3	-114.1	1.8	-38.3	1.5	1.53	0.02	9.2	0.0	0.56	0.01
KIC10737052	-300.0	6.9	59.0	4.0	62.9	2.4	9.20	2.18	21.3	1.1	0.90	0.00
KIC11563791	-23.0	1.2	-38.9	1.1	72.2	3.0	3.44	0.55	8.2	0.1	0.82	0.01
KIC11566038	-147.9	4.4	-46.6	1.6	-34.6	0.7	0.97	0.03	10.2	0.1	0.85	0.01
KIC12017985	-141.7	4.8	76.5	1.5	-88.4	1.7	3.61	0.10	10.4	0.2	0.73	0.00
KIC12017985-17	-135.1	4.1	75.1	1.3	-86.2	1.5	3.50	0.07	10.2	0.1	0.73	0.00
KIC12253381	-344.1	10.2	35.5	4.7	-40.6	1.2	2.02	0.16	27.4	2.2	0.96	0.01

[a]The `ruwe` is ~ 1.7, and hence the values presented here must be considered with a caution for this star.

Although we did not fully utilize stellar kinematics for the target selection, we can confirm that most of our targets have halo-like kinematics thanks to astrometric measurements by the Gaia mission (Gaia Collaboration et al., 2016b). We adopt proper motions provided in Gaia data release 2 (Gaia DR2; Gaia Collaboration et al., 2018) and radial velocity measured from our spectra (see Section 5.2). Distance can be estimated from either astrometric parallax or asteroseismic parallax. For the former, we use parallax measurements in Gaia DR2 (Lindegren et al., 2018) after correction for systematic offset of 0.052 mas (Zinn et al., 2019). For the asteroseismic parallax, we first compute radius using asteroseismic scaling relations. Combined with effective temperature from our high-resolution spectra, we obtain luminosity of the stars through $L \propto R^2 T_{\rm eff}^4$. To derive parallax, this luminosity is then compared with the bolometric magnitude that is based on The Two Micron All-Sky Survey (2MASS; Skrutskie et al., 2006) K_s band photometry and the bolometric correction provided by (Casagrande & VandenBerg, 2014). Interstellar extinction is corrected for using the 3D extinction map provided by Green et al. (2018). The two parallaxes are provided in Table 5.3 and are compared in Figure 5.3. Note that Table 5.3 lists astrometric parallax without the 0.052 mas correction, but the correction is applied in Figure 5.3. They agree well each other. For the calculation of kinematics, we adopt one with smaller uncertainty for each star. The choice is also shown in Table 5.3.

Table 5.4 shows quantities that characterize orbits of stars. We adopt $R_0 = 8.2\,{\rm kpc}$ (McMillan, 2017) and $z_0 = 0.025\,{\rm kpc}$ (Jurić et al., 2008) for the solar position, and $(v_x, v_y, v_z)_\odot = (11.1,\ 247.97,\ 7.25)\,{\rm km\,s^{-1}}$ for the solar velocity relative to the Galactic center, where v_x is the velocity toward the Galactic center, v_y is in the direction of Galactic rotation, and v_z is toward north. The v_x and v_z come from Schönrich et al. (2010), and v_y comes from the proper motion measurement of the Sgr A* (Reid & Brunthaler, 2004) and R_0. Coordinate transformation from observed quantities to the Galactocentric Cartesian system was conducted with `astropy.coordinates` package. We note that v_ϕ is taken positive toward the Galactic rotation direction. Orbits of stars are integrated in the Milky Way potential by McMillan (2017) with `AGAMA` (Vasiliev, 2019) for sufficiently long time to get the maximum vertical excursion, $z_{\rm max}$, the distance to the Galactic center at apocenter $r_{\rm max}$, and eccentricity, e. Errors are estimated by Monte Carlo sampling. We note that all the stars are treated as single, although some show radial velocity variation. While the presence of a binary companion might lead to inaccurate astrometric measurements in Gaia DR2, the Renormalised Unit Weight Error (`ruwe`), whose high value indicates a problematic astrometric solution, is smaller than 1.3 except for KIC5858947, for which `ruwe` is ~ 1.7.

Figure 5.4 shows the velocity distribution of stars. It is clear that most of the program stars do not follow the motion of the majority of the stars in the *Kepler* field, i.e., they have very different velocities than the Galactic disk

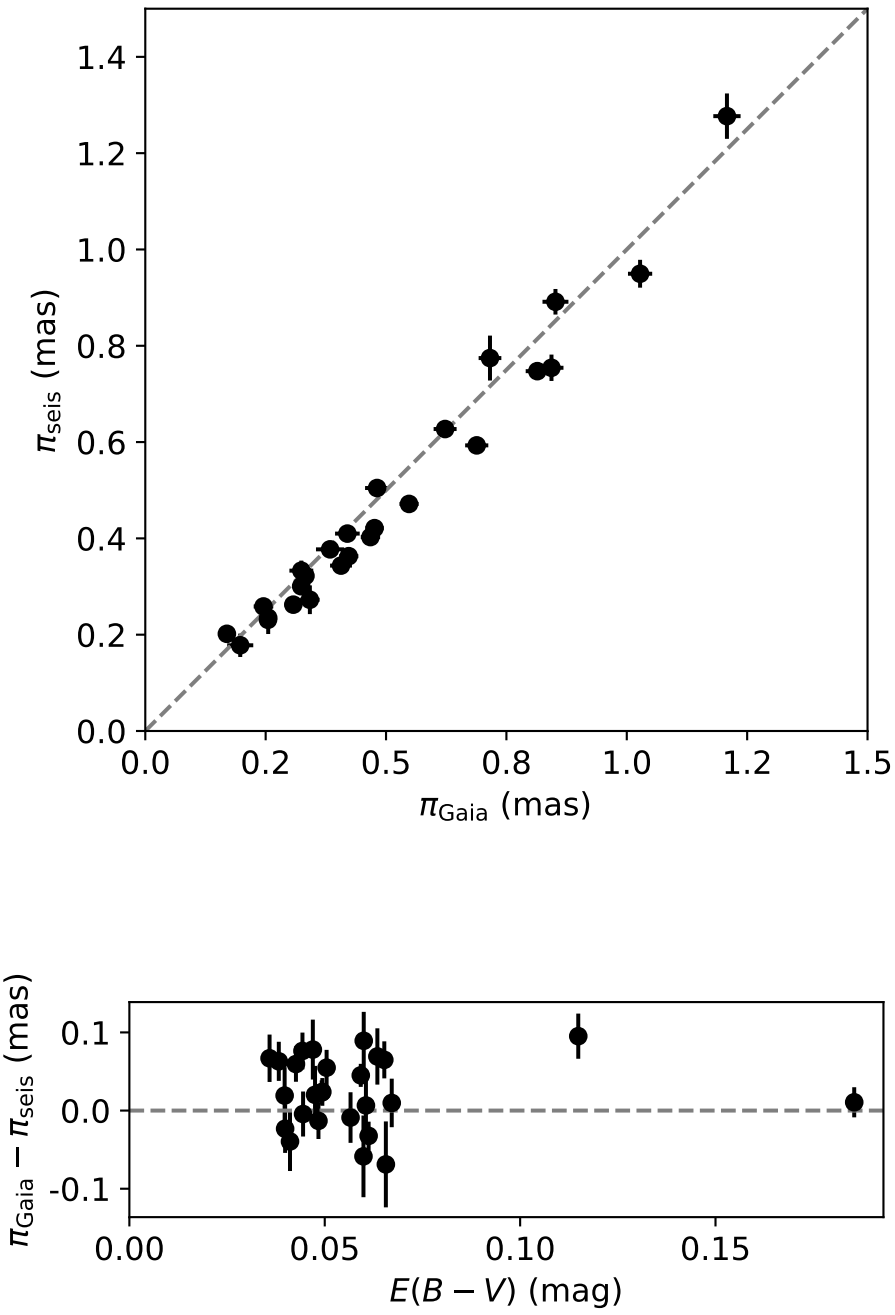

Figure 5.3 Comparison of Gaia and asteroseismic parallaxes. The zero point offset of Gaia parallax is corrected. The lower panel shows the difference as a function of reddening.

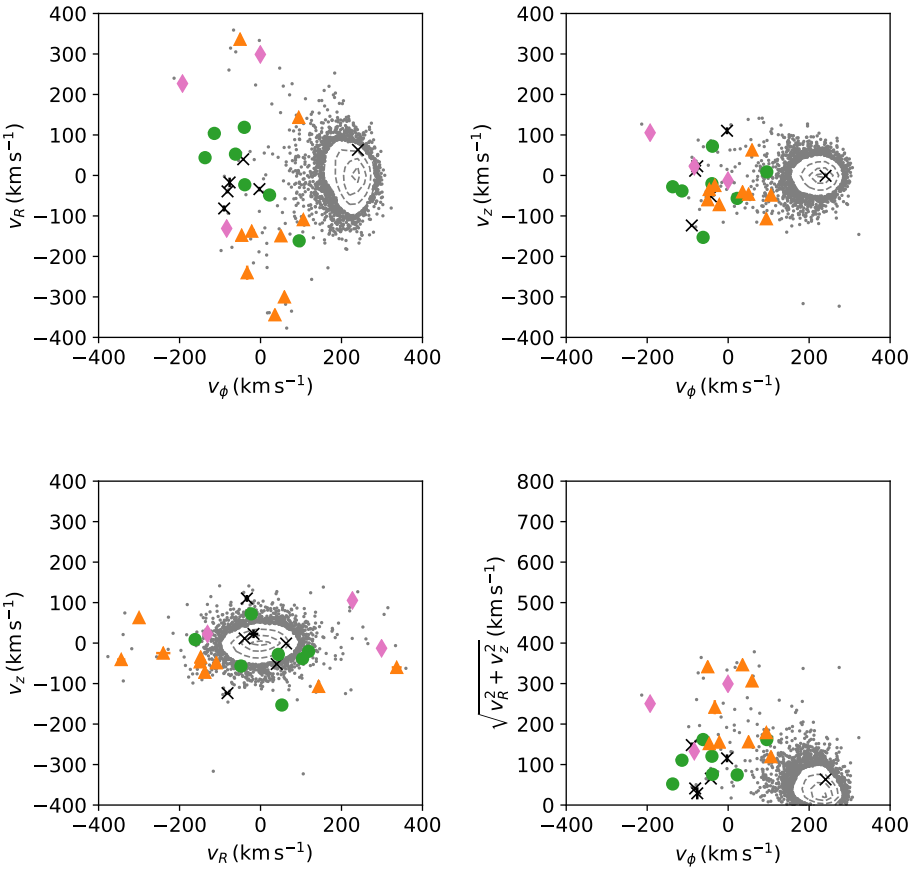

Figure 5.4 Large symbols (black cross, green circles, orange triangles and pink diamonds) show velocities of the program stars with errorbars, while grey points and contours are the distribution of stars in the crossmatched catalog of LAMOST DR5 (Zong et al., 2018) and Yu et al. (2018). The different symbols are used according to the Mg and Fe based classification made in Section 5.5. For the LAMOST sample, we calculated velocities in exactly the same way as for the program stars.

Table 5.5. Line list and measured equivalent widths.

λ (Å)	species	χ (eV)	$\log gf$	Syn	KIC5184073 (mÅ)
4053.821	Ti II	1.89	-1.07		80.8
4056.187	Ti II	0.61	-3.28		49.5
4082.939	Mn I	2.18	-0.35		...
4086.714	La II	0.00	-0.07	syn	59.2
4099.783	V I	0.28	-0.10		41.6

Note. — The entity of the table is available online (`https://www.dropbox.com/s/4ig6dlcpatecth6/Table5.tex?dl=0`).

stars. This is expected since our selection is partly based on radial velocity and since the *Kepler* field is centered at $l = 76.32°$. The only exception would be KIC7693833; however, we keep this star in our sample since it is one of the lowest metallicity stars.

5.5 Abundance analysis

5.5.1 Line list

Table 5.5 shows a list of lines used in this study together with measured equivalent widths. Lines are carefully selected by comparing synthetic spectra and very high-S/N observed spectra of HD122563. Additional lines are added from Matsuno et al. (2018) for analyses of high-metallicity stars. Hyperfine structure splitting is included for Sc II, V I, Mn I, Co I, Cu I, Ba II, and Eu II, assuming solar r-process abundance ratio for neutron capture elements. Line positions and relative strengths are taken from McWilliam (1998, Ba) , Ivans et al. (2006, Eu), and Robert L. Kurucz's linelist for the others.

Equivalent widths are measured through fitting Gaussian to absorption lines. Lines are limited to those with reduced equivalent width ($REW = \log(EW/\lambda)$) smaller than -4.5 to avoid significant effects of saturation. Figure 5.5 compares equivalent widths measured from 2017 and 2018 observations for KIC12017985. Despite different wavelength resolutions, the two measurements show good agreement.

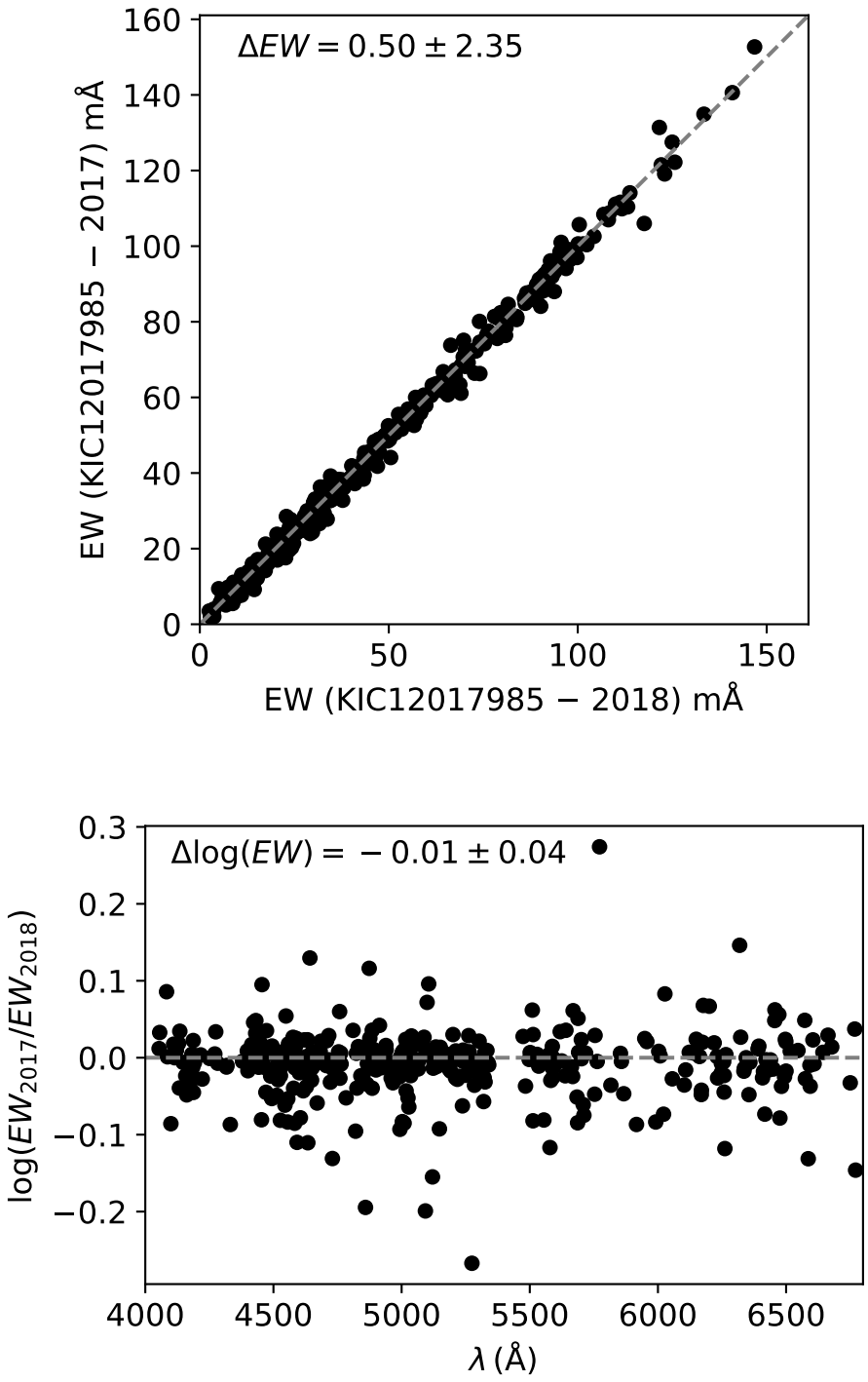

Figure 5.5 Comparison of equivalent widths for KIC12017985 from 2017 and 2018 observations. Mean difference and line-to-line scatter are shown in the figure.

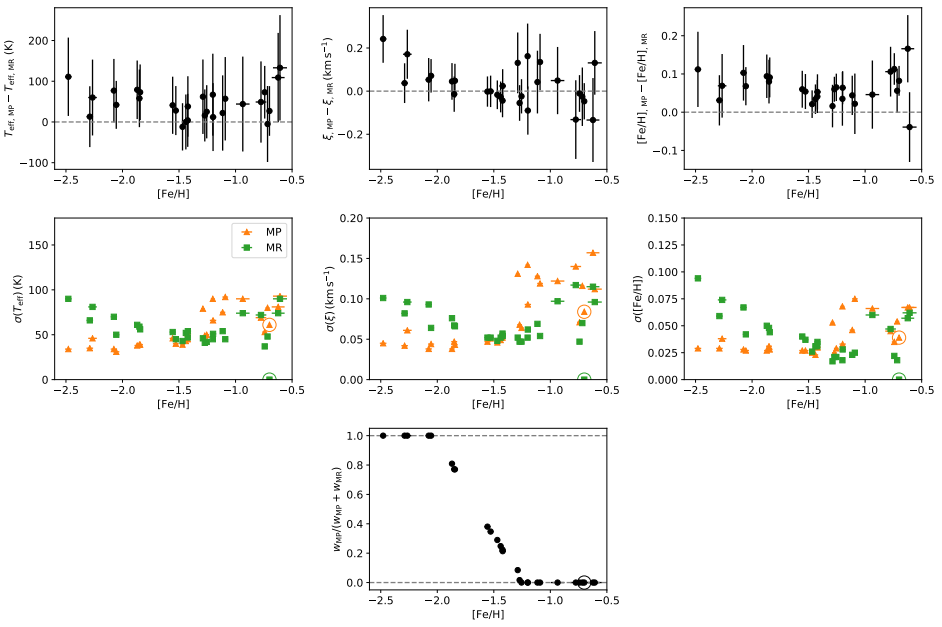

Figure 5.6 Comparison of stellar parameters from two analyses. One analysis uses the metal-poor standard star (HD122563) and the other uses the metal-rich one (KIC9583607). Since the latter is one of the program stars, we show its location with open circle in the bottom four panels. Considering the trends in the ξ uncertainties, we adopt stellar parameters with the weights shown in the bottom panel.

5.5.2 Stellar parameter determination

Stellar parameter determination and subsequent abundance measurements are conducted with a modified version of `q2` (Ramírez et al., 2014; Matsuno et al., 2018), through which abundance calculation is conducted by February 2017 version of the `MOOG` (Sneden, 1973). We obtain models of the structure of atmospheres from interpolation of MARCS atmospheres with standard chemical composition (Gustafsson et al., 2008b). In the process of stellar parameter determination, we adopt the line-by-line non-LTE corrections provided by Amarsi et al. (2016a) [23]. All the subsequent abundance analysis is conducted under one dimensional plane-parallel (1D) and local thermo-dynamical equilibrium (LTE) approximations otherwise stated.

Stellar parameters are determined spectroscopically for $T_{\rm eff}$ and ξ. The surface gravity is constrained from asteroseismology. We also used a prior on ξ as a function of $\log g$ (see Appendix 5.A).

To achieve high-precision and to minimize the effects of departures from 1D approximations and those of uncertain atomic data, we adopt a line-

[23] The grid is available at `http://www.mpia.de/homes/amarsi/index.html`

Table 5.6. Adopted stellar parameters

Object	$T_{\rm eff}$ (K)	$\sigma_{(T_{\rm eff})}$ (K)	$\log g$	$\sigma_{(\log g)}$	ξ (km s^{-1})	$\sigma_{(\xi)}$ (km s^{-1})	[Fe/H]	$\sigma_{([\rm Fe/H])}$
KIC5184073	4864	44	1.876	0.010	1.581	0.044	-1.422	0.028
KIC5439372	4835	34	1.716	0.016	1.915	0.045	-2.479	0.029
KIC5446927	5102	37	2.261	0.008	1.530	0.047	-0.742	0.022
KIC5698156	4644	43	1.888	0.015	1.533	0.049	-1.289	0.016
KIC5858947	5105	72	3.149	0.004	1.221	0.117	-0.775	0.047
KIC5953450	5127	74	3.071	0.005	1.234	0.115	-0.623	0.057
KIC6279038	4761	31	1.654	0.025	1.784	0.044	-2.055	0.027
KIC6520576	4971	35	2.169	0.014	1.602	0.042	-2.289	0.029
KIC6611219	4652	45	1.742	0.016	1.566	0.052	-1.201	0.018
KIC7191496	4903	34	2.122	0.007	1.672	0.038	-2.076	0.028
KIC7693833	5094	46	2.422	0.006	1.664	0.061	-2.265	0.038
KIC7948268	5154	51	3.004	0.004	1.230	0.062	-1.199	0.028
KIC8350894	4797	45	2.012	0.012	1.491	0.054	-1.091	0.025
KIC9335536	4817	32	1.951	0.026	1.527	0.038	-1.528	0.026
KIC9339711	4937	33	2.226	0.006	1.509	0.037	-1.469	0.020
KIC9583607	5059	···	2.322	···	1.590	···	-0.700	···
KIC9696716	4962	41	2.297	0.009	1.453	0.041	-1.440	0.024
KIC10083815	4784	74	2.161	0.013	1.476	0.097	-0.936	0.060
KIC10096113	4948	48	2.475	0.007	1.443	0.070	-0.717	0.018
KIC10328894	5018	33	2.405	0.006	1.528	0.039	-1.850	0.026
KIC10460723	4922	40	2.275	0.010	1.466	0.046	-1.272	0.021
KIC10737052	4973	42	2.340	0.008	1.478	0.047	-1.255	0.021
KIC10992126	4253	90	1.774	0.015	1.571	0.096	-0.607	0.062
KIC11563791	4974	54	2.550	0.006	1.326	0.069	-1.114	0.023
KIC11566038	4999	38	2.413	0.005	1.451	0.046	-1.423	0.025
KIC12017985	4945	33	2.175	0.006	1.628	0.036	-1.844	0.024
KIC12017985-17	4932	33	2.175	0.007	1.637	0.034	-1.870	0.024
KIC12253381	4922	37	2.256	0.007	1.512	0.037	-1.556	0.027

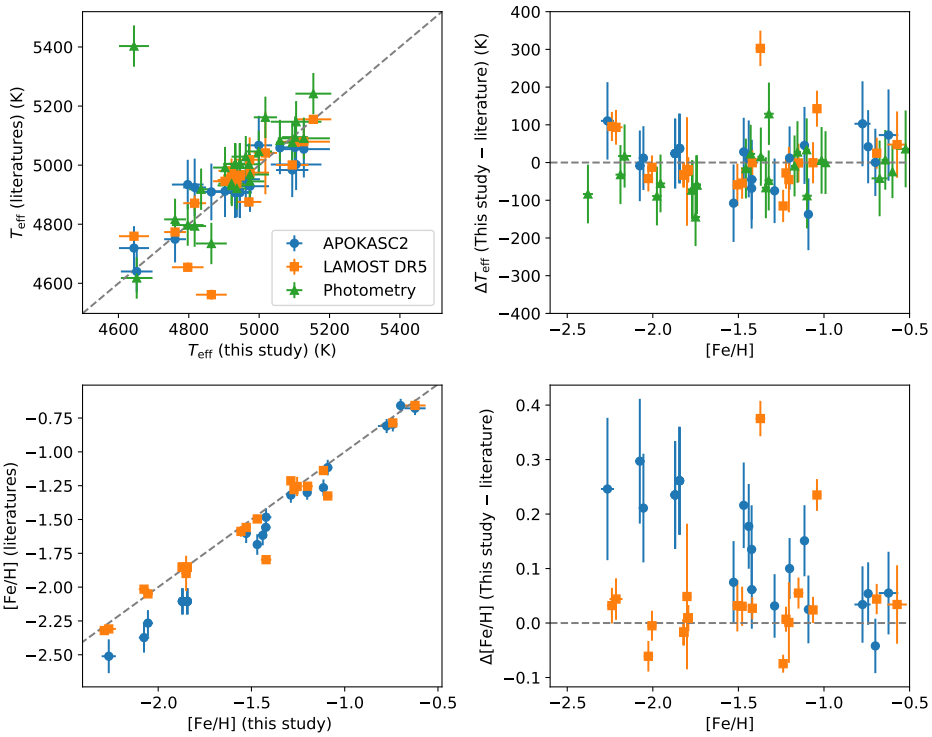

Figure 5.7 Comparison of stellar parameters with literatures. We note that errorbars only reflect internal errors in our analysis and surveys.

by-line differential abundance analysis. Since our targets span over ∼2 dex in metallicity, we repeated analysis adopting two standard stars. One is a well-studied metal-poor star HD 122563 with [Fe/H]∼ −2.6. This star is the only metal-poor giant whose $T_{\rm eff}$ and $\log g$ have been measured with high accuracy through interferometric measurements (Karovicova et al., 2018) and asteroseismology (Creevey et al., 2019), respectively. The other standard star is one of the program stars, KIC9583607, which is a metal-rich star ([Fe/H]∼ −0.7) and was also observed by APOGEE. Since APOGEE is carefully calibrated at high metallicity and since this star has an asteroseismic $\log g$ constraint, the use of this star as a standard star ensures us that our parameters are not systematically biased. Stellar parameters determined relative to HD122563 and those relative to KIC9583607 are denoted as $X_{\rm MP}$ and $X_{\rm MR}$ respectively.

Each star has two sets of parameters, and we need to combine the two results in a way that we obtain precise parameters without significant systematic offsets. We here combine the two results following the equation,

$$X = X_{\rm MP} * w_{\rm MP} + X_{\rm MR} * w_{\rm MR}, \tag{5.1}$$

where $w_{\rm MP}$ and $w_{\rm MR}$ are the weights. We determine $w_{\rm MP}$ and $w_{\rm MR}$ from the comparison of the two sets of analyses.

The comparison is provided in Figure 5.6 for parameters and their errors as a function of metallicity. When a star and the standard star have large metallicity difference, there are two types of difficulties. The first one is that departures from 1D approximations might not act in the same way. The other difficulty is that a number of common lines becomes smaller as the metallicity difference becomes larger. This is because absorption lines of the more metal-rich one suffer from saturation or blending while those of the more metal-poor one might be too weak to be detected. These effects are recognisable in Figure 5.6. Microturbulence velocity particularly suffers from metallicity difference. Considering the behavior of the uncertainties of microturbulence velocities, we define

$$x_{\rm MP} = \quad 1.0 - ([{\rm Fe/H}]_{\rm standard} - [{\rm Fe/H}]_{\rm MP})/s_{\rm MP} \tag{5.2}$$

$$x_{\rm MR} = \quad 1.0 - ([{\rm Fe/H}]_{\rm MR} - [{\rm Fe/H}]_{\rm standard})/s_{\rm MR}, \tag{5.3}$$

where $s_{\rm MP}$ and $s_{\rm MR}$ are free parameters, and define $w_{\rm MP} = max\{0.0,\, min\{1.0,\, x_{\rm MP}\}\}$ (similarly for $w_{\rm MR}$). The $w_{\rm MP}$ and w_{MR} are then scaled so that their sum becomes 1. The two parameters, $s_{\rm MP}$ and $s_{\rm MR}$ are chosen to be 1.4, but results are insensitive to the exact choice of these parameters for most of the stars. Obtained $w_{\rm MP}$ and $w_{\rm MR}$ are also shown in Figure 5.6 and adopted parameters are listed in Table 5.6. The parameters in Table 5.6 are used in asteroseismology including mass estimates and in figures throughout this study.

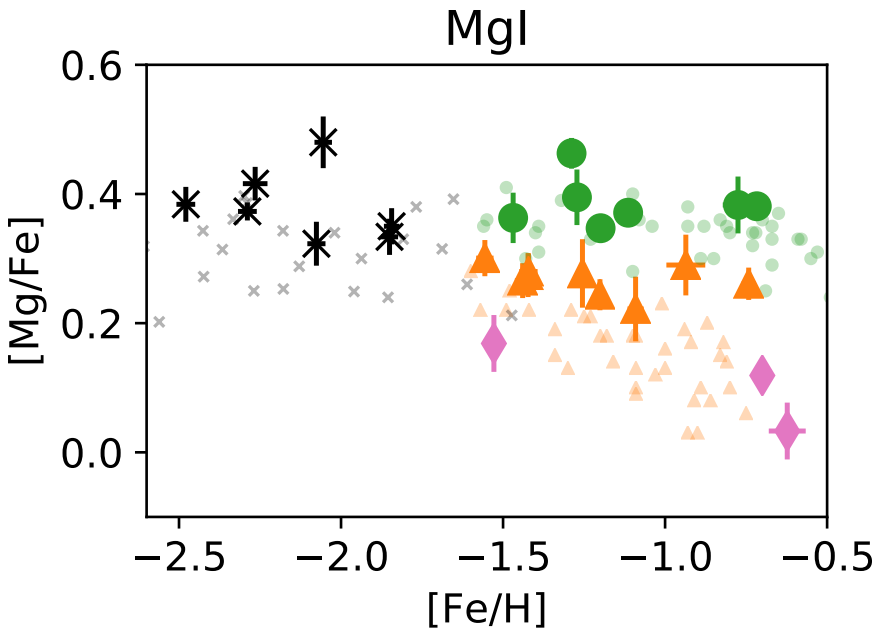

Figure 5.8 Mg abundance ratios of stars derived from Mg I. Our targets are shown with large symbols with errorbars and are divided into four depending on their Mg and Fe abundance: metal-poor (black crosses), α-rich (green circles), α-poor (orange triangles) and very α-poor (pink diamonds). Small green circles and orange triangles are high-/low-α populations from Nissen & Schuster (2010, 2011) and Fishlock et al. (2017). Small black crosses are stars from Reggiani et al. (2017). These stars from literatures are to guide eyes and a quantitative comparison needs a caution (see text).

Uncertainties provided in this thesis only reflects random errors that are obtained through a MCMC method. It is important to take systematic uncertainties into consideration when one tries to quantitatively compare our results with other studies. Source of systematic uncertainties includes the uncertainties in stellar parameters and abundances of the standard stars, possible blending with unknown weak lines, and deviation from assumed model atmosphere in real photospheres. Among these, the impact of the first source is studied in Appendix 5.C.

The obtained parameters are compared to spectroscopic surveys (APOGEE and LAMOST) and photometric temperature in Figure 5.7. The good agreements show that our parameters do not have large systematic offsets.

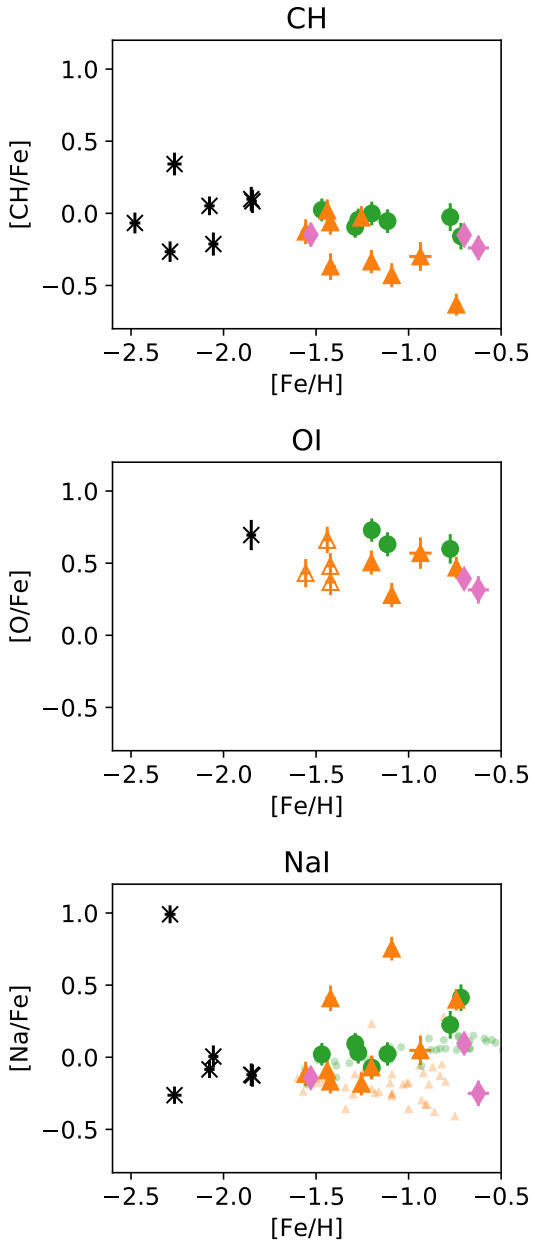

Figure 5.9 Same as Figure 5.8 but for C (CH), O (O I), and Na (Na I). Open symbols indicate that while the abundance should be derived by weighing two analyses with different standard stars, only one of them can be used since the other standard does not have common lines with the target star.

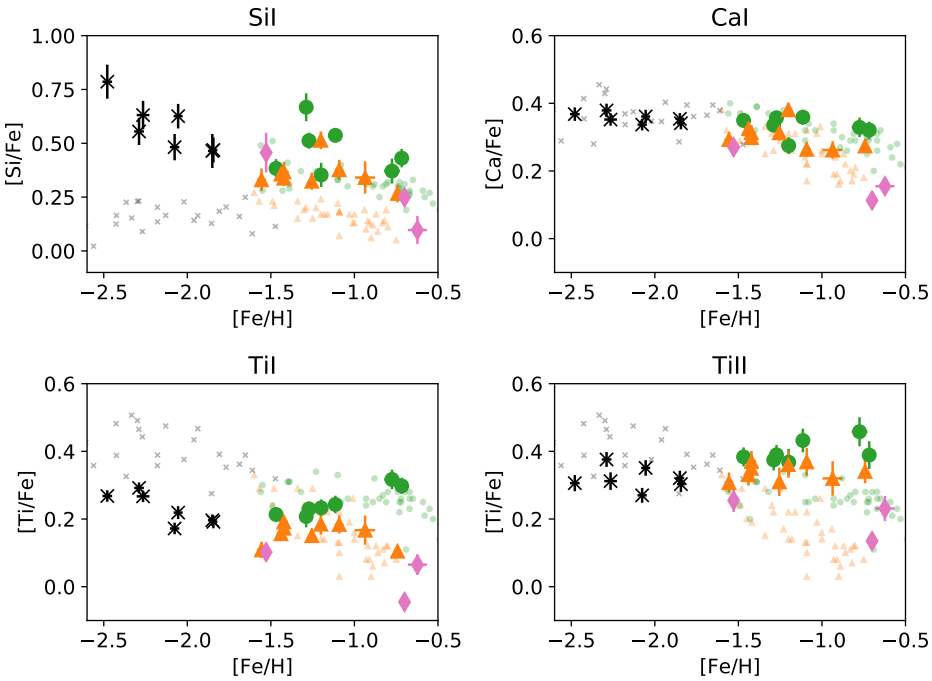

Figure 5.10 Same as Figure 5.8 but for Si (Si I), Ca (Ca I), and Ti (Ti I and Ti II). Note that the vertical scale is different only for Si.

Table 5.7. Abundances

Object	Species	[X/H]	$\sigma_{(X/H)}$	[X/Fe]	$\sigma_{(X/Fe)}$
KIC5184073	Mg I	-1.26	0.09	0.28	0.03
KIC5184073	CH	-1.91	0.31	-0.37	0.09
KIC5184073	O I	-1.18	0.09	0.37	0.09
KIC5184073	Na I	-1.13	0.15	0.41	0.09
KIC5184073	Si I	-1.17	0.07	0.37	0.05

Note. — A portion is shown here. The entity is available online (`https://www.dropbox.com/s/p31pgfwjh3ahxnr/Table8.tex?dl=0`).

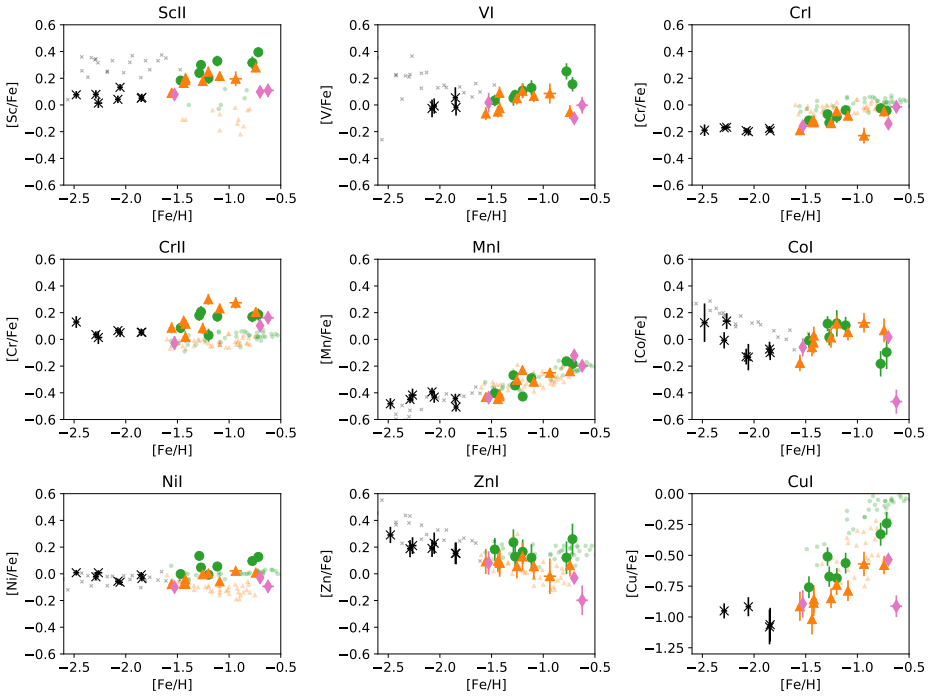

Figure 5.11 Same as Figure 5.9 but for V (V I), Cr (Cr I and Cr II), Mn (Mn I), Co (Co I), Ni (Ni I), Zn (Zn I) and Cu (Cu I). Note that the vertical scale is different only for Cu.

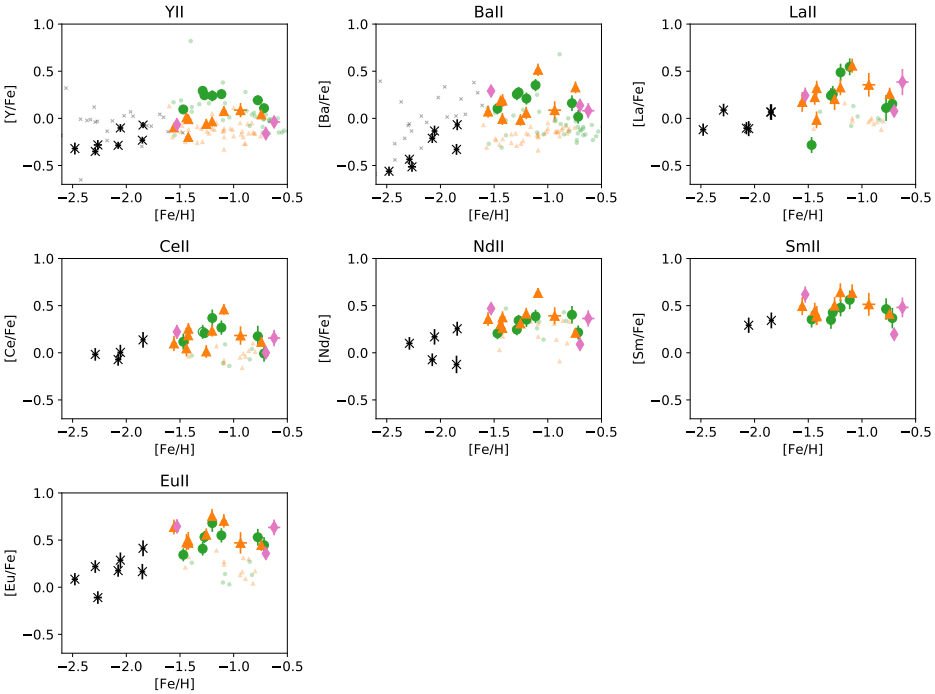

Figure 5.12 Same as Figure 5.8 but for Y (Y II), Zr (Zr I), Ba (Ba II), La (La II), Ce (Ce II), Nd (Nd II), Sm (Sm II), and Eu (Eu II).

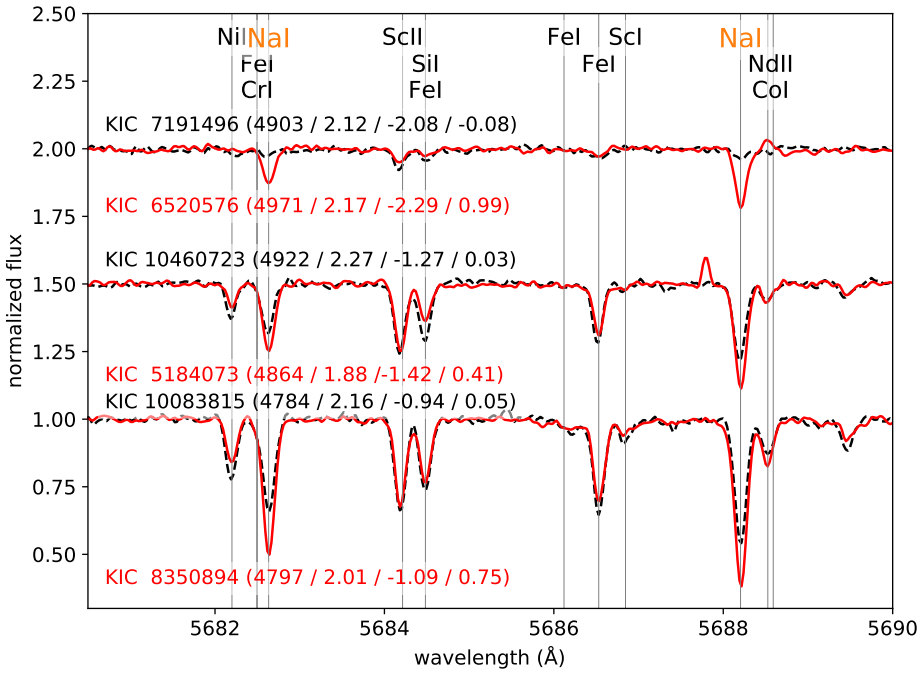

Figure 5.13 Spectra of Na-enhanced objects (red solid) and those of comparison stars (black dashed) with offsets for visualization purpose. Stellar parameters and 1D LTE abundances are shown as ($T_{\rm eff}$ / $\log g$ / [Fe/H] / [Na/Fe]).

5.5.3 Elemental abundances

Elemental abundances are derived based on equivalent widths for most of the elements. We first derive abundances for the standard stars, then derive abundances of the other stars differentially through a line-by-line analysis. Thanks to this approach, we achieve high precision in relative abundances, although the absolute scale could be affected by systematic uncertainties such as those due to NLTE effects.

As in the case for the stellar parameters, we obtain two sets of chemical abundance for each star through two analyses with different standard stars. We combine these abundances with the Eq. 5.1. However, there are cases where a star has no common line with one of the standard stars for some elements. In this case, we have to rely on the abundance derived from the analysis with the other standard star. Unless this other analysis has a weight of 1, the abundance of the star has to be taken with a caution and we show these cases with open circles in the figures.

We estimate uncertainties as follows: there are two sources of uncertainty in abundance measurements. One is due to the noise present in the spectra, which affects measured equivalent widths. We denote this component as σ_1 and estimate it from the line-to-line scatter ($\sigma_{\rm sct}$) in derived abundance for each element as $\sigma_1 = \sigma_{\rm sct}/\sqrt{N}$, where N is the number of lines used for the abundance measurements. When N is smaller than 4 and when $\sigma_{\rm sct}$ is smaller than $\sigma_{\rm sct}$ for Fe I lines, we substitute $\sigma_{\rm sct}$ with the latter. The other source is the uncertainties of stellar parameters (σ_2). This component is estimated by repeating analyses changing stellar parameters by the same amount as their uncertainties. We quadratically sum σ_1 and σ_2 to obtain final error estimates.

Abundances from CH (molecule), and O I, Na I, Mg I, Co I, Cu I, Zn I, Ba II, La II, Ce II, Nd II, Sm II, and Eu II (small number of available lines) are analysed through spectral synthesis. Synthetic spectra with stellar parameters listed in Table 5.6 are compared with observed spectra using linelists from VALD3 [24] to get the best-fit abundance. Equivalent width of the line that is listed in Table 5.5 is then estimated for the best-fit abundance. We carry out equivalent widths analysis using these estimated equivalent widths as we did for the other elements to consistently derive abundances.

5.5.4 Abundances: results

Abundances are provided in Table 5.7 and shown as a function of metallicity in Figures 5.8, 5.9, 5.10, 5.11, and 5.12. Our stars are compared with turn-off halo stars studied by Nissen & Schuster (2010, 2011), Fishlock et al. (2017), and Reggiani et al. (2017). This comparison is not meant to be

[24] `http://vald.astro.uu.se/`

quantitative but to guide eyes. It is necessary to account for systematic uncertainties in addition to those reported in this study when our abundances are quantitatively compared with other studies (see Appendix 5.C).

Following Nissen & Schuster (2010), we divide our sample using Mg abundance (Figure 5.8). Firstly, our sample is divided by the metallicity at [Fe/H]~ -1.7 (metal-poor/others). For the metal-rich sample, we further divide the sample by [Mg/Fe]: stars having [Mg/Fe] comparable to the metal-poor subsample (high-α), those having lower [Mg/Fe] (low-α), and those having even lower [Mg/Fe] (very low-α). While [Mg/Fe] spreads among each of the three metal-rich subsamples are small and comparable to the measurement errors, differences in average [Mg/Fe] between different subsamples are significantly larger than measurement errors. However, this division is arbitrary, and we investigate if the three subsamples also show differences in other element abundances or in kinematics in Section 5.6.1.

There seems to be Na-enhanced metal-poor objects (KIC8350894, KIC5184073, and KIC6520576), for which spectra around Na I 5688 Å are shown in Figure 5.13. The Na enhancements are clear and cannot be attributable to cosmic ray or bad pixels. While tabulated Na abundances are in 1D/LTE, it is known that Na suffers from large NLTE effects (Lind et al., 2011). NLTE corrections (NLTE − LTE) from Lind et al. (2011) are -0.114, -0.141 and -0.232 for KIC6520576, KIC5184073, and KIC8350894, while those for their comparison stars in Figure 5.13 are ~ -0.06, -0.115 and -0.145, respectively. Therefore, NLTE effects cannot be the cause of the large Na abundance. The origin of these stars are discussed in the Section 5.6.4.

Si abundance shows large scatter and increasing trend toward low metallicity, which is not seen in literatures (e.g., Zhang et al., 2011). NLTE effect for Si abundance is not expected to be large for giants (Shi et al., 2009). Since multiple lines are used for the analysis, the source of this behavior remains unknown.

5.6 Discussion

5.6.1 Halo subpopulations

We divided the sample into four subsamples in Section 5.5. We investigate kinematics and abundances of the four subsamples in this subsection.

We first focus on our high-α and low-α subsamples. There are at least hints of abundance difference between high-α and low-α subsamples in [X/Fe] of many elements (C, O, Na, Ca, Sc, Ti, V, Ni, Cu, Zn, and Y). For most of these elements except for Na and Ca, the probability that the two subsamples have the same mean abundance is small ($P < 0.05$). Na and Ca abundance differences are not statistically significant, which would be due to a few outliers. Other elements do not show differences because of, e.g., insufficient abundance precision, intrinsic dispersion in each of the two sub-

sample, and/or intrinsic lack of difference. The last possibility applies to elements whose origin is similar to Fe, i.e., they are contributed from both of type Ia and II supernovae. These results are consistent with abundance differences between turn-off high-α and low-α populations reported in literatures (Nissen & Schuster, 2010, 2011; Nissen et al., 2014). This suggests that our high-/low-α subsamples correspond to the two distinct halo populations reported by Nissen & Schuster (2010).

These two subsamples also differ in stellar kinematics (Figure 5.4). The radial component of the velocity (v_R) shows completely different distribution, with our low-α subsample having large absolute values. This suggests that the low-α population has more radial orbit, which is a signature of Gaia Sausage (Belokurov et al., 2018). Since Gaia Sausage (or Gaia Enceladus; Helmi et al., 2018) is considered to correspond to the low-α population of Nissen & Schuster (2010), kinematics also supports the correspondence of our low-α subsample and the low-α population of Nissen & Schuster (2010). Although Nissen & Schuster (2010) reported that the high-α and low-α populations tend to be prograde and retrograde, respectively, we do not detect such difference. This could be due to the selection of halo stars in the sense that, since our selection of halo stars is more strict, high-α stars that have relatively similar orbits to thick disk stars might be excluded. Note that we include radial velocity in the selection (Section 5.2), which basically traces v_ϕ thanks to the galactic longitude of the *Kepler* field.

We here discuss the very low-α subsample. This subsample consists of three stars, KIC5953450, KIC9335536, and KIC9583607, among which KIC9335536 is located at [Fe/H]~ -1.5 and the others are at [Fe/H]~ -0.6. While these three stars are selected as very low α subsample based on Mg abundance, other element abundances also seem to behave differently from other subsamples with a tendency of being extreme cases of the low-α subsample discussed above. Kinematics are characterized by high v_R and basically follow the trend of the low-α subsample. While these results suggest that the very low-α subsample is clearly different from high-α population, it is still unclear if they are a separate component from the low-α subsample.

The metal-poor subsample is chemically homogeneous to some extent; there are tight trends of [X/Fe] with [Fe/H] for many of the elements studied. This is consistent with the result by Reggiani et al. (2017), who conducted high-precision abundance analysis for metal-poor turn-off stars concluding that there is no significant scatter in abundances.

It is not clear from chemical abundances if the metal-poor subsample corresponds to the low metallicity extension of other subsamples. On the other hand, kinematics are more similar to the high-α subsample, which might be related to a fraction of metal-poor stars in the low-α or high-α populations. However, we note that no radial velocity selection was adopted in the sample selection for the lowest metallicity stars (Figure 5.1), which would affect their distribution in the velocity space.

5.6.2 How reliable is the asteroseismic mass?

In this subsection, we discuss reliability of mass estimates from asteroseismology. It has been discussed for low-metallicity stars in Epstein et al. (2014), Casey et al. (2018), Miglio et al. (2016), and Valentini et al. (2019). Here we have 26 halo stars, of which 5 are below [Fe/H]< -2 and additional 16 are below [Fe/H]< -1. As far as we know, this is the largest sample of metal-poor stars for which asteroseismology and high-resolution spectroscopy are combined. We take advantage of our sample to re-visit the asteroseismology at low-metallicity.

In Figure 5.14, we investigate if the estimated mass correlates with metallicity or surface gravity. We also present theoretical mass of low-mass red giant stars from MESA Isochrones and Stellar Tracks (MIST; Dotter, 2016; Choi et al., 2016), which is based on Modules for Experiments in Stellar Astrophysics (MESA; Paxton et al., 2011). Since halo stars are generally considered to be old from independent studies ($\sim$ 10 Gyr; e.g., Schuster et al., 2012; Carollo et al., 2016; Kilic et al., 2019), we present the mass as a function of metallicity for 6, 8, 10, 12, and 14 Gyr isochrones. Red giant stars are selected based on surface gravity ($\log g < 3.3$) and the `phase` parameter as they are on either of red giant branch phase, core He burning phase, early AGB phase, or thermal-pulse AGB phase (`phase`= 2, 3, 4, and 5). The mass range of red giant stars are measured for each isochrone and shown in the Figure 5.14.

The upper panel clearly shows that our sample has an intrinsic mass scatter at fixed metallicity, in particular the presence of outliers are evident. In order to inspect if this spread is due to the evolutionary status, the lower panel visualizes the correlation between mass and surface gravity. This panel suggests that mass of luminous giants ($\log g \lesssim 2.0$) is systematically lower, or is underestimated, although uncertainties are large for some luminous stars due to low oscillation frequencies. We also note that the two over-massive stars are red clump stars. Possible systematic mass offsets for these luminous giants and red clump stars are also suggested by, e.g., Pinsonneault et al. (2018). This could be due to mass loss or systematic uncertainties that only affect these stars.

Considering these possible effects of evolutionary status on the mass estimates, we separate red clump stars and luminous giants from other RGB stars. If we focus on less-luminous RGB stars ($\log g < 2$), the estimated masses show smaller dispersion. In fact, χ^2-test indicates that the mass dispersion is insignificant if we exclude red clump stars and luminous stars ($P = 0.65$, 15 stars), whereas there is a significant dispersion in mass when we consider all the stars ($P < 0.0001$).

Even though mass dispersion disappears by limiting evolutionary status, the average mass (0.97 $M_\odot$) is still higher than the value usually adopted for typical halo stars (0.8 $M_\odot$); the mass could be over-estimated at least

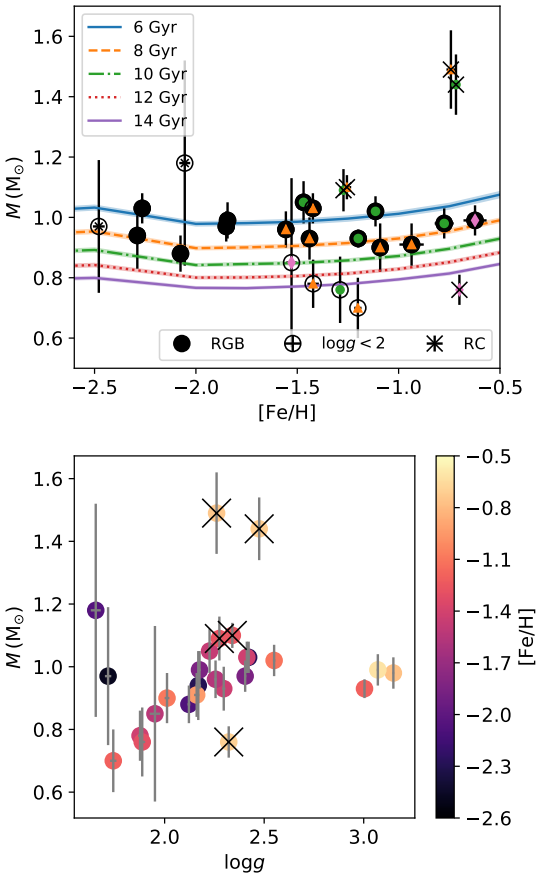

Figure 5.14 (*Upper:*) Mass of stars as a function of metallicity. Red clump stars, luminous stars, and the other red giant branch stars are separated. Small symbols are over plotted according to the Mg and Fe classification in Section 5.5.4. We present theoretical initial mass of red giant branch stars from MIST isochrones for various age and metallicity (Dotter, 2016; Choi et al., 2016, ; see text for more details.). Note that while each theoretical line has a width reflecting the mass range of stars along the red giant branch, the width is too narrow to be visible in most cases. (*Lower:*) Mass of stars as a function of surface gravity. Cross symbols are over-plotted for red clump stars.

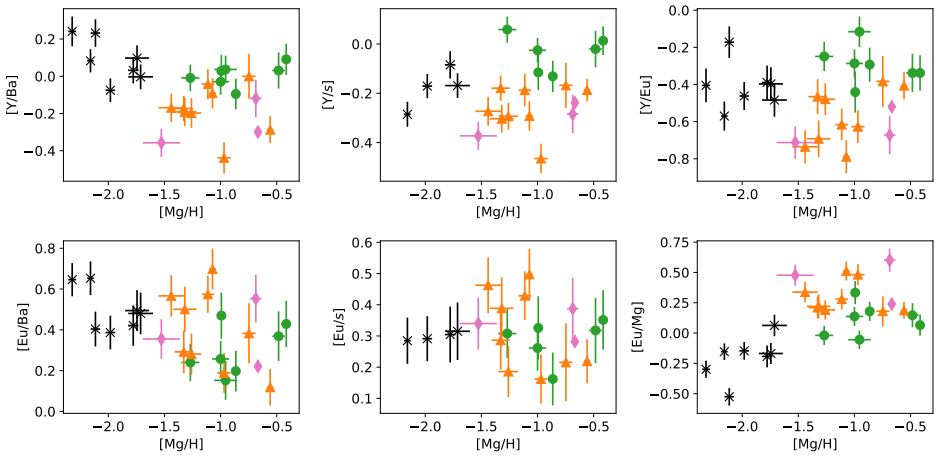

Figure 5.15 Abundance trends of neutron-capture elements. Here s is the average of Ba, La, Ce, and Nd.

by 10%. This difference cannot be explained by offset of stellar parameter estimates since our stellar parameters are derived differentially to well-calibrated stars, which indicates our parameters are not severely affected by systematic uncertainties. In addition, in order to reduce the derived mass by 10%, we need to change $T_{\rm eff}$ by 15%, which corresponds to $\sim 750\,$K. This is much larger than expected uncertainties in spectroscopic stellar parameter determination including systematic uncertainties.

The small scatter we obtained after limiting the evolutionary status indicates that the mass of low-metallicity stars can be estimated with high internal precision. However, further studies are required to solve the possible systematic offset and to achieve high accuracy.

5.6.3 Formation timescales of the halo

In this subsection, we discuss formation timescales of the Galactic halo focusing on our high-α and low-α subsamples. We first discuss constraints from chemical abundances and then discuss those from stellar mass. Since we have shown that these two subsamples corresponds to the low-α and high-α populations of Nissen & Schuster (2010), we refer each subsample as a population.

Constraints from abundances

The [α/Fe] difference is usually interpreted as a result of different amounts of type Ia supernovae contribution, which is a result of different star formation timescale (Nissen & Schuster, 2010). Differences in other elemental abundances could also be explained by type Ia supernovae contributions.

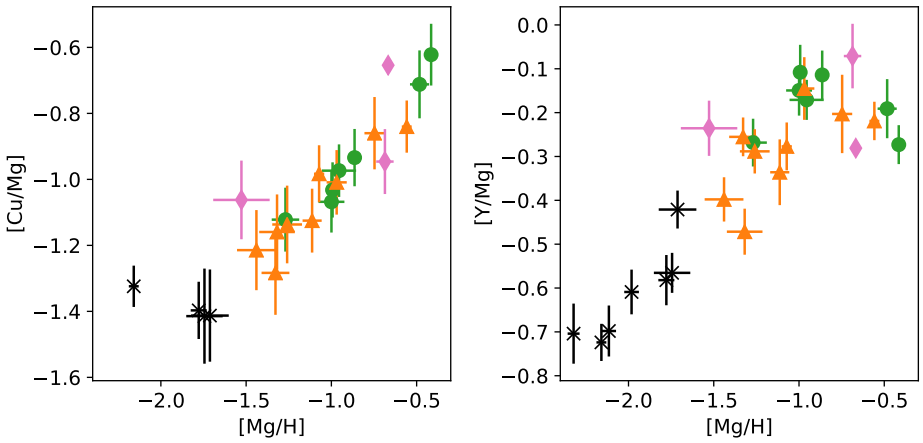

Figure 5.16 Abundance trends of Cu and Y as a function of [Mg/H].

For example, Na and Sc, which are not α-elements, are mostly synthesized by massive stars and ejected by type II supernovae having similar nucleosynthesis origins as α-elements. On the other hand, some other elements, especially neutron-capture elements, could have different nucleosynthesis origins, which would deliver independent information.

Figure 5.15 shows abundance ratios between neutron capture elements (see also Fishlock et al., 2017). Y is a light neutron capture element, which is considered to be formed by weak s-process in massive stars (e.g., Pignatari et al., 2010). Y abundance are generally low in low-α population (see [Y/Fe] in Figure 5.12, and [Y/Ba], [Y/s], and [Y/Eu] in Figure 5.15), which suggests underproduction of Y in low-α population. We here discuss reason of the Y underproduction together with Cu abundances, since Cu is also considered to be formed through the weak s-process (e.g., Romano & Matteucci, 2007).

The ^{22}Ne(α,n)^{25}Mg reaction is the source of neutrons in the weak s-process. Since the ^{22}Ne is produced from CNO elements through H burning and α captures to ^{14}N, this process is dependent on CNO abundance and only efficient at [C,N,O/H]$\gtrsim -2$ (e.g., Prantzos et al., 1990). Hence, the products of weak s-process like Cu and Y have secondary nature. Figure 5.16 shows chemical evolution of these two elements in relation to Mg. We here choose Mg instead of Fe because both CNO and Mg are mostly produced by type II supernovae, whereas Fe is also produced by type Ia supernovae. Figure 5.16 demonstrates that Cu and Y abundances show tighter correlations when they are studied relative to Mg than when studied relative to Fe. In addition, the abundance difference between low-/high-α populations becomes almost absent. These results suggest that the low Cu and Y abundances of the low-α population are because of their low yield in

the weak s-process, which is caused by the low CNO and Mg abundances at a given [Fe/H]. Therefore, we conclude that star formation timescale of the low-/high-α populations, and Cu and Y abundance differences in Figure 5.12 and 5.15, are not directly related but could be indirectly related through different [C,N,O/Fe] abundances.

Eu is an almost pure r-process element. Eu appears enhanced relative to Y or Mg in the low-α population (Figure 5.15). Recent studies have been collecting evidence that the dominant production site of r-process elements is neutron star merger (Wanajo et al., 2014b). Since it takes time for two neutron stars to merge, we expect delay time in r-process enrichments although it seems shorter than that of Type Ia supernovae (e.g., Ji et al., 2016; Hirai et al., 2015). The enhanced Eu abundance of the low-α population is explained by the delay time of r-process enrichments and longer star formation timescale of the population. This is an example that star formation timescale is constrained from elements whose origin is totally different from α-elements or Fe. Here, studies of two independent indicators, α-elements and Eu, reach the same conclusion: longer star formation timescale for low-α population.

The dominant nucleosynthesis site of heavy s-process elements, including Ba, La, Ce, and Nd, are considered to be low-to-intermediate mass AGB stars at solar metallicity (so-called main s). Since these AGB progenitors have long main-sequence life time, their contributions are expected to occur at late times. Abundances of these elements could consequently differ between systems with different star formation timescales. However, the heavy s-process element abundances, especially relative to Eu, do not show differences between our high-α/low-α populations (Figure 5.15). This suggests that AGB stars contribution would be small for both populations. Almost flat evolution of [s/Eu] among the whole target stars supports the lack of low-to-intermediate star contributions.

It is worth noting that the [s/Eu] ratio is slightly higher than the pure r-process ratio. This might indicate that massive stars contribute to the heavy s-process element enrichments. It has been suggested that massive stars with high rotation speed can produce a large amount of heavy s-process elements (e.g., Choplin et al., 2018).

It is surprising that s-process contribution is almost absent while type Ia supernovae already seems to have started contributing. It is true that the maximum initial mass of white dwarf progenitors is expected to be higher than that of AGB progenitors that produce significant amount of heavy s-process elements. However, type Ia supernovae would need additional time after the formation of first white dwarfs. Our results suggest that the delay time for white dwarfs to explode need to be very short.

Although the low-α population is considered to be an accreted massive dwarf galaxy, the behavior of s-process elements are different from dwarf galaxies currently around the Milky Way. They tend to show signatures of

heavy s-process enhancements (e.g., Hill et al., 2019; Letarte et al., 2010). This suggests that the low-α population have experienced faster evolution than those dwarf galaxies.

We have investigated contributions of type Ia supernovae, type II supernovae, weak s-process in massive stars, r-process, and heavy s-process in low-α and high-α populations. These give constraints on the star formation timescale of the halo populations. Firstly, type Ia supernovae need at least $\sim 100\,\mathrm{Myr}$ after star formation, which corresponds to the lifetime of the most massive white dwarf progenitor. This gives lower limit on the star formation timescale of the low-α population. The lack of main s contribution gives us a constraint as well. Heavy s-process elements are mainly produced by stars less massive than $\sim 3\,\mathrm{M}_\odot$ (Straniero et al., 2014). The lifetime of a $3\,\mathrm{M}_\odot$ star is $\sim 200 - 300\,\mathrm{Myr}$. Therefore, both the low-α and the high-α populations have to be evolved up to [Mg/H]~ -1 within a few $\times 100\,\mathrm{Myr}$ before $\sim 3\,\mathrm{M}_\odot$ stars start to contribute to the chemical evolution. This a few $\times 100\,\mathrm{Myr}$ is an upper limit on star formation timescale. In principle, the r-process enhancement of the low-α population can also give an independent constraint. However, since there is a large uncertainty in the delay time of r-process enhancements, we do not aim to put quantitative constraints from r-process abundances.

Based on these estimates, we conclude that star formation timescale τ can be constrained to $100 \lesssim \tau/\mathrm{Myr} \lesssim 300$ for the low-α population. Although the timescale is not well constrained well for the high-α population in the present study, it is clear that it has a shorter timescale ($\lesssim 100\,\mathrm{Myr}$).

Constraint from mass

Stellar age is a fundamental parameter when we retrieve the information about the Galaxy formation history from stars. Since we have systematic offsets in mass determination, we refrain from using age directly. However, as shown in Figure 5.14, the red giant mass does not depend on the metallicity significantly. Therefore, we here use stellar mass as an indicator of relative stellar age.

The overall average age of halo stars have been known to be old ($\gtrsim 10\,\mathrm{Gyr}$) from independent studies. However, the age distribution among halo stars, i.e., age dispersion or age difference between different halo populations, remains to be investigated. In this subsection we focus on age spread of halo stars and age differences between the two halo populations. These are equivalent to studying relative age among halo stars, which is feasible even in the presence of systematic offsets in estimated ages if internal precision is sufficiently high (see Section 5.6.2). In addition, this information from age estimates is complementary to chemical abundances since it does not rely on theoretical nucleosynthesis yields and since it enables us to discuss not only formation timescale but also formation epoch.

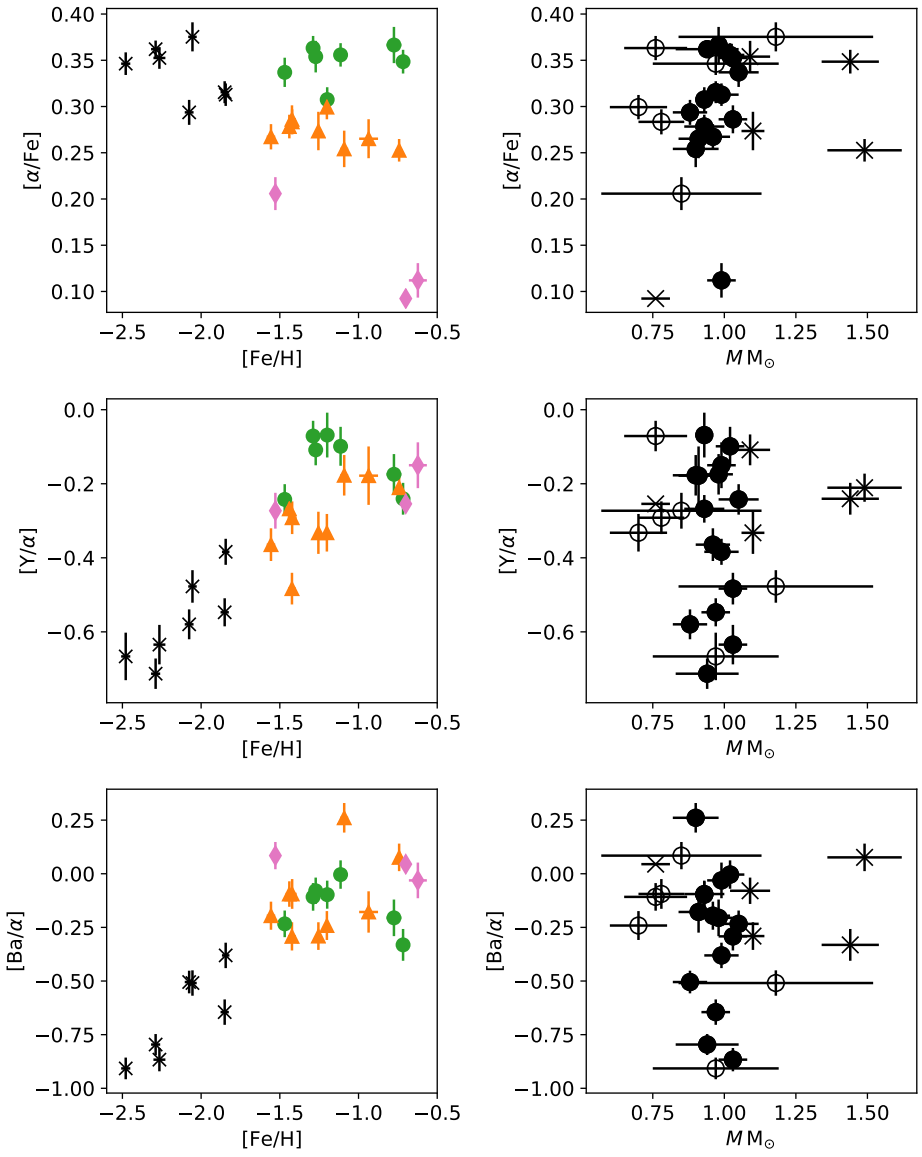

Figure 5.17 Investigation of correlations between mass and abundances. Symbols follow Figure 5.14.

Although chemical abundances and kinematics span over a significantly wide range with an amplitude much larger than measurement errors, we do not expect significant correlations between masses and other properties of stars since we did not find significant dispersion in mass. We have, in fact, explored possible correlations between masses and abundances, and those between masses and kinematics, and found no correlation. For example, abundance ratios such as [α/Fe], or [Y/Mg] are shown to show good correlations with stellar age for disk stars (da Silva et al., 2012; Nissen, 2016; Tucci Maia et al., 2016; Feltzing et al., 2017; Spina et al., 2018b). Figure 5.17 show the results of our investigation on [α/Fe], [Y/α], [Ba/α] [25]. The absence of correlation indicates that chemical evolution has to proceed fast, which is consistent with the discussion from chemical abundances.

Since our discussion is based on stellar mass, it is not possible to directly give an upper limit on the age dispersion. However, the lack of mass dispersion among the whole halo stars provides an upper limit on intrinsic mass dispersion, which can be translated into internal relative age dispersion. Currently the weighted sample standard deviation of the mass is $0.05\,\mathrm{M}_\odot$ (or 0.05% of the average mass) for all the 15 stars on the lower red giant branch phase. Since this dispersion can totally be explained by measurement errors (Section 5.6.2), intrinsic mass dispersion should be smaller than this value. Age of red giant branch stars is roughly proportional to $\sim M^{-3.5}$ in this metallicity and mass range. Therefore, we obtain an upper limit on relative age dispersion of $< 18\%$. Considering typical ages of halo stars provided in literatures, 18% corresponds to $\sim 2\,\mathrm{Gyr}$.

The age difference between our low-α and high-α stars is also insignificant ($\langle M \rangle = 0.962$ and $0.968\,\mathrm{M}_\odot$ respectively; $P = 0.87$). The 2σ upper limits on the age difference is $0.09\,\mathrm{M}_\odot$ (or 10% of the average). Following the same argument as for the dispersion, the relative age difference between the two populations is $< 3 - 4\,\mathrm{Gyr}$ (35%). This is consistent with the study of the age difference of halo stars but for nearby turn-off stars by Schuster et al. (2012).

The non-detection of age dispersion or age difference is due to the combined effect of limited age (mass) precision, the metallicity range of the targets, and limited sample size. Improvements in age precision are definitely desired. Although there is a room of improvements for the model of stellar oscillations as we saw in Section 5.6.2, it might be difficult to achieve revolutionary improvements in terms of precision. We note that most of the uncertainties in derived mass stems from the errors in oscillation frequencies. We used oscillation frequencies that are measured from the best available light curves obtained from the ~ 4 years of continuous observation by the *Kepler* mission. No near-future mission is planned to obtain similar

[25] Here we define α abundance as the average of Mg, Ca, and Ti. For Ti, we adopt the average of Ti I and Ti II.

long-term light curves. One of the ways to improve the mass measurement precision is to take luminosity into consideration. If the luminosity is measured with sufficiently high precision, it enables us to achieve ~ 2 times smaller uncertainty (Rodrigues et al., 2017). Although precise luminosity measurements are being made possible thanks to the Gaia mission, it is necessary to resolve the systematic mass offsets found in Section 5.6.2. Unless we confirm there is no systematic offsets, combining independent information does not necessarily lead to a narrower posterior distribution.

The metallicity range is another issue. In Schuster et al. (2012)'s results, the age difference between high-α and low-α stars is larger in higher metallicity bins. Since our targets are more on lower metallicity side compared to their study, age difference might be revealed using asteroseismology by focusing on the high metallicity end of the halo. Increasing the sample size would also allow us to reveal a small average age difference.

5.6.4 Peculiar objects

Na-enhanced stars

As noted in Section 5.5, there are three Na-enhanced objects. There is no anomaly in their elemental abundances except for possible low O abundances in two stars (Figure 5.18) and high *s*-process element abundance in one star (KIC8350894; Ba, La, Ce, and Nd abundances are 0.52, 0.53, 0.46, and 0.63 in [X/Fe]). The masses of the three stars are low (Figure 5.18), and two of them are in the red giant branch phase. Information about KIC6520576 is limited since its O abundance could not be measured due to the blending of the O absorption line with telluric lines and its evolutionary status is not provided in Yu et al. (2018). Note that there is no sign of radial velocity variation or C enhancements among the Na enhanced stars.

Large Na enhancements are sometimes seen in globular clusters (e.g., Carretta et al., 2009) and were used to search for metal-poor stars ejected from globular clusters (Pereira et al., 2019). Those Na enhanced objects in clusters usually accompany O deficiency (known as Na-O anti-correlation; Carretta et al., 2009). The possibly low O abundance of KIC5184073 and KIC8350894 might indicate their globular cluster origin. Further investigation on Mg-Al anti-correlation, Li, C, and N abundances are highly desired for these two stars.

Internal mixing might also cause Na-enhancements especially in AGB stars or in massive stars. However, there are no evidence for the presence of internal mixing among our Na-enhanced stars.

KIC6520576 resembles CD-23°16310, which was reported to have [Na/Fe]$=+1.09$ at [Fe/H]$=-1.93$ (Pereira et al., 2019). Both giants have large (~ 1 dex) Na enhancements at low metallicity, but do not show peculiar abundance pattern including C. The most notable difference is the luminosity

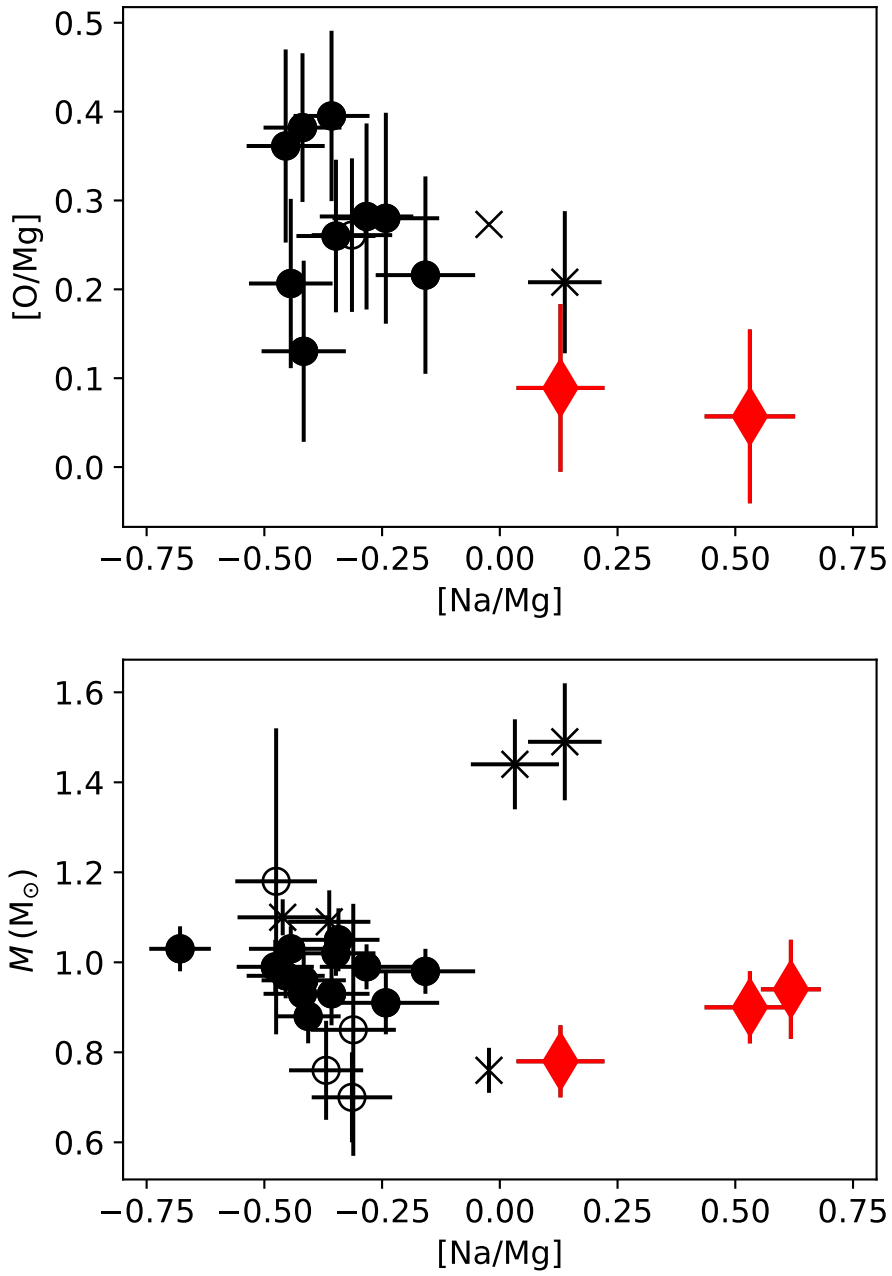

Figure 5.18 O-Na and mass-Na correlations. Na enhanced stars are shown with red diamonds while others are shown with black symbols. The shape of the symbols follow Figure 5.14.

or surface gravity; while KIC6520576 has $\log g = 2.17$, CD-23°16310 has $\log g = 0.9$. Pereira et al. (2019) suspect CD-23°16310 is in the early AGB phase. It is not yet clear at this stage if KIC6520576 can also be interpreted as in the early AGB phase.

Over-massive stars

Among our sample, two stars are obviously over-massive (KIC5446927 and KIC10096113). Even though these stars are on the metal-rich side in our halo stars, they are too metal-poor to have such high-mass. They also have super-solar [α/Fe] and large relative velocity to the Sun, suggesting their old age.

Therefore, these two stars are too massive for their chemical and kinematic properties. Similar stars have been found among the Galactic disk (so-called young α-rich stars; Chapter 3; Martig et al., 2015; Chiappini et al., 2015). The young α-rich stars are massive but their chemical abundance are just the same as normal old disk stars (Yong et al., 2016; Matsuno et al., 2018). Important property of the young α-rich stars is that they show high fraction of radial velocity variation (Jofré et al., 2016; Matsuno et al., 2018), suggesting binary interaction is the key for the formation of these stars. Theoretical work also supports this scenario (Izzard et al., 2018).

Radial velocity measurements of KIC5446927 and KIC10096113 do not reveal their binary nature at this stage (Table 5.1). KIC5446927 actually has precise radial velocity measurements by our observation, APOGEE, and Gaia, all of which perfectly agree. Although not every young α-rich star shows radial velocity variation, the absence of radial velocity variation might indicate the origin of these stars to be different from young α-rich stars. Further monitoring of radial velocities of these stars are, of course, welcomed to draw robust conclusion about the origin of these stars.

It is interesting to note that Na abundance of the two objects looks enhanced (Figure 5.18), although the level of the enhancements is not as significant as the three stars studied in the previous subsection considering the Galactic chemical evolution (Figure 5.9). Smiljanic et al. (2016) showed that massive giants have high Na abundance. However, they concluded that the effects appear in stars more massive than $2.0\,M_\odot$, which is larger than our two over-massive stars. Another interesting aspect of these stars is their evolutionary status; both of the two stars are red clump stars. Additional mixing at the tip of red giant branch might affect Na abundance of these stars.

5.7 Conclusion

We obtain precise stellar parameters and precise chemical abundances for 26 halo stars in the *Kepler* filed, for which asteroseismic information is

available. The sample is selected based on radial velocity and metallicity estimated from spectroscopic surveys. The kinematics of the selected stars are later investigated with the Gaia DR2 data, confirming that they have halo-like kinematics. Stellar parameters are determined precisely and accurately by adopting a differential abundance analysis and using standard stars with accurate $T_{\rm eff}$ and $\log g$. Subsequently we obtain precise chemical abundances.

Our study is by far the largest sample of low-metallicity stars with asteroseismic information and precise stellar parameters. We investigate the reliability of asteroseismic mass estimates at low metallicity with this large sample. The average mass obtained from asteroseismology is $1.03\,{\rm M}_\odot$ (without correction) and $0.96\,{\rm M}_\odot$ (with $\Delta\nu$ correction). This result indicates that, although correction to the $\Delta\nu$ scaling relation helps to reduce inconsistency between asteroseismic and expected masses ($\sim 0.8\,{\rm M}_\odot$), it is not capable of completely resolving the issue.

We also show that luminous red giant stars and red clump stars could suffer from systematic uncertainties. After excluding these stars, there is no significant mass dispersion among our sample. This fact indicates that, despite the systematic offset, the mass of halo stars can be estimated with high-precision if we focus on less-evolved red giants.

The precise chemical abundances allow us to separate our targets into high-α and low-α halo populations by the Mg abundance. The two populations also differ in other element abundances consistent with Nissen & Schuster (2010, 2011) and Fishlock et al. (2017). The low-α population shows low values of [X/Fe], where X is C, O, Na, Ca, Sc, Ti, V, Ni, Cu, Zn, and Y. Most of these elements are ejected from massive stars, and thus the low values are understood as a result of type Ia supernovae contribution. Y abundance in the low-α population is lower compared to heavy s-elements or Eu. This, together with Cu abundance, is understood as a result of their secondary nature in the production by the weak s-process. There is no significant difference in Eu-to-heavy s-process abundance ratio, indicating that the main s-process from low-to-intermediate mass AGB stars does not contribute significantly to neither of low-α or high-α populations. Eu abundance relative to Mg is enhanced in the low-α population, suggesting that the delay time of neutron star mergers plays a role.

These chemical abundances provide constraints on the timescale of star formation (τ). Since the low-α population is enriched from type Ia supernovae, τ should be longer than $\gtrsim 100\,{\rm Myr}$, which comes from the life time of the most massive star that leaves a white dwarf. The lack of the main s-process contribution, on the other hand, provides an upper limit on the timescale as $\tau \lesssim 300\,{\rm Myr}$. These indicate the low-α population formed with a timescale of $100 \lesssim \tau/{\rm Myr} \lesssim 300$, and the high-$\alpha$ population formed with a shorter timescale.

The asteroseismic information independently constrains the formation

time scale and additionally provides a constraint on the relative formation epochs of the two populations. The lack of significant mass dispersion among less luminous red giant branch stars gives an upper limit on the intrinsic mass dispersion of $< 0.05\,M_\odot$. This can be translated to age dispersion of $\lesssim 2\,$Gyr. The average mass of less luminous red giant branch stars is 0.962 and $0.968\,M_\odot$ for high-α and low-α populations. This difference is not significant and gives a relative age difference of $< 4\,$Gyr. These do not contradict with previous study (Schuster et al., 2012) or with chemical abundances.

Our study is the first study that combines chemical abundances and stellar mass (age) estimates for more than 10 field halo stars beyond the solar neighbourhood. However, we did not detect age spreads among our sample or age difference between populations unlike Schuster et al. (2012). The reason of the non-detection would be limited precision, metallicity range, and/or sample size. A factor of 2–3 improvements would make the precision comparable to the precision that was achieved for nearby turn-off stars (Schuster et al., 2012). This level of improvements might be achieved by incorporating luminosities into mass estimates (Rodrigues et al., 2017), after resolving the systematic offset in masses we obtained in this study. Instead, a study that focuses on the high metallicity end of the halo with a larger sample size might be able to reveal the age difference. Such sample will be provided by space-based photometric monitoring observations with a wider field coverage, such as K2, TESS, or PLATO.

This Chapter demonstrates that we are now able to extend the study of halo stellar populations with a chemically defined separation beyond the solar neighbourhood using asteroseismology. We indeed constrain the formation timescales and epochs using asteroseismology and precise chemical abundances, providing insights for the Galactic halo formation and for the Milky Way merging history.

Appendix 5.A Microturbulence prior as a function of $\log g$

Microturbulence is determined spectroscopically so that abundances derived from individual neutral iron lines do not show correlation with line strengths. However, due to the wide parameter range of our sample, microturbulent velocities do not converge well for some of the stars. Poorly constrained microturbulent velocity affects the precision of the temperature and the abundances. In order to mitigate this problem, we use non-flat prior on microturbulence during stellar parameter determination.

Here we describe how we chose the ξ prior (Figure 5.19). We first run

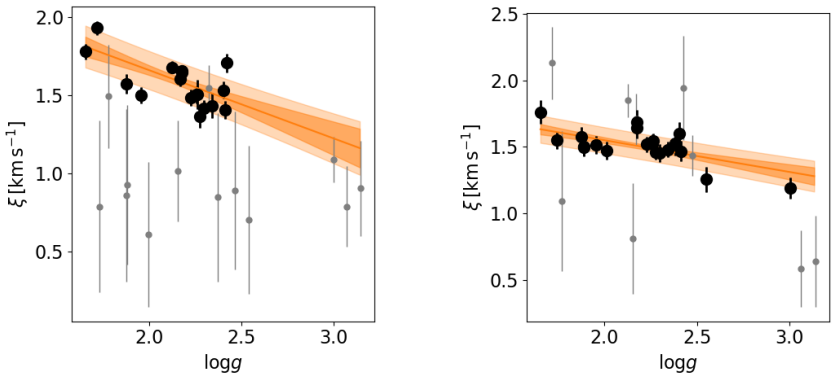

Figure 5.19 The relation between microturbulence and surface gravity. Black large symbols are used to determine the prior, and grey small circles are other objects. The orange solid line, thick filled region, and thin filled region are the best fit linear relation, uncertainties in the fit, and 1σ interval of the prior at given $\log g$. The left and right panel is for the analysis relative to HD122563 and that relative to KIC9583607, respectively.

stellar parameter determination processes with flat microturbulence prior. We then carry out a linear fit to the relation between the microturbulent velocity and the surface gravity using stars whose microturbulent velocity is determined with high precision ($\sigma(\xi) < 0.1\,\mathrm{km\,s^{-1}}$). Note that microturbulent velocity of the other stars with large uncertainties agree with the best fit linear relation at $< 2\sigma$ level in most cases. Based on this fit we put prior on ξ as

$$p(\xi|\log g) = \frac{1}{\sqrt{2\pi\sigma^2}} \exp(-(\xi - \mu(\log g))^2/2\sigma^2), \tag{5.4}$$

where $\mu(\log g)$ is the expected value of ξ at given $\log g$ from the linear fit, σ is obtained from $\sigma = \sigma^2_{\rm fit}(\log g) + \sigma^2_{\rm resid}$, and the $\sigma_{\rm fit}(\log g)$ is the expected standard deviation at given $\log g$ due to the uncertainties in the fitting parameters. The $\sigma_{\rm resid}$ is a constant expressed as $\sigma^2_{\rm resid} = \sum_i (\xi_i - \mu(\log g_i))^2/(N-\nu)$, where N and ν is the number of stars used for the fit and the degree of freedom ($\nu = 2$ in this case), respectively.

The inclusion of ξ prior does not affect stars whose ξ is determined precisely in the first step. For the other stars, it provides a better convergence in the stellar parameter determination.

Appendix 5.B Stellar parameters from analyses with different standard stars

In this study, we carried out two sets of the analyses with two reference stars, HD122563 and KIC9583607. Table 5.8 shows stellar parameters derived from each of the analyses. Final stellar parameters adopted for, e.g., mass estimates, are the combination of two results following the weights ($w_{\rm MP}$ and $w_{\rm MR}$) provided in the Table.

Table 5.8. Stellar parameters from the two analyses

Object	Analysis with HD122563 (MP)							Analysis with KIC958367 (MR)						
	$T_{\rm eff}$ (K)	$\sigma_{(T_{\rm eff})}$ (K)	ξ (km s^{-1})	$\sigma_{(\xi)}$ (km s^{-1})	[Fe/H]	$\sigma_{([{\rm Fe/H}])}$	$w_{\rm MP}$	$T_{\rm eff}$ (K)	$\sigma_{(T_{\rm eff})}$ (K)	ξ (km s^{-1})	$\sigma_{(\xi)}$ (km s^{-1})	[Fe/H]	$\sigma_{([{\rm Fe/H}])}$	$w_{\rm MR}$
KIC5184073	4894	51	1.600	0.056	-1.380	0.030	0.213	4856	54	1.576	0.054	-1.433	0.035	0.787
KIC5439372	4835	34	1.915	0.045	-2.479	0.029	1.000	4724	90	1.673	0.101	-2.591	0.094	0.000
KIC5446927	5175	53	1.519	0.071	-0.629	0.035	0.000	5102	37	1.530	0.047	-0.742	0.022	1.000
KIC5698156	4701	79	1.653	0.131	-1.274	0.053	0.085	4639	46	1.522	0.052	-1.290	0.017	0.915
KIC5858947	5154	69	1.089	0.140	-0.669	0.045	0.000	5105	72	1.221	0.117	-0.775	0.047	1.000
KIC5953450	5236	81	1.100	0.157	-0.457	0.067	0.000	5127	74	1.234	0.115	-0.623	0.057	1.000
KIC6279038	4761	31	1.784	0.044	-2.055	0.027	1.000	4719	50	1.713	0.064	-2.123	0.042	0.000
KIC6520576	4971	35	1.602	0.042	-2.289	0.029	1.000	4958	66	1.565	0.082	-2.320	0.059	0.000
KIC6611219	4719	90	1.728	0.142	-1.166	0.068	0.000	4652	45	1.566	0.052	-1.201	0.018	1.000
KIC7191496	4903	34	1.672	0.038	-2.076	0.028	1.000	4826	70	1.619	0.093	-2.179	0.067	0.000
KIC7693833	5094	46	1.664	0.061	-2.265	0.038	1.000	5034	81	1.493	0.096	-2.334	0.074	0.000
KIC7948268	5166	66	1.140	0.093	-1.135	0.033	0.000	5154	51	1.230	0.062	-1.199	0.028	1.000
KIC8350894	4854	92	1.626	0.119	-1.069	0.075	0.000	4797	45	1.491	0.054	-1.091	0.025	1.000
KIC9335536	4835	40	1.526	0.051	-1.493	0.027	0.347	4807	45	1.527	0.052	-1.547	0.037	0.653
KIC9339711	4928	39	1.497	0.046	-1.454	0.025	0.290	4940	43	1.514	0.048	-1.475	0.026	0.710
KIC9583607	5086	61	1.543	0.084	-0.618	0.039	0.000	5059	···	1.590	···	-0.700	···	1.000
KIC9696716	4962	43	1.433	0.049	-1.414	0.023	0.248	4962	52	1.460	0.052	-1.448	0.031	0.752
KIC10083815	4828	90	1.525	0.122	-0.890	0.066	0.000	4784	74	1.476	0.097	-0.936	0.060	1.000

Table 5.8 (cont'd)

Object	Analysis with HD122563 (MP)							Analysis with KIC958367 (MR)						
	$T_{\rm eff}$ (K)	$\sigma_{(T_{\rm eff})}$ (K)	ξ (km s^{-1})	$\sigma_{(\xi)}$ (km s^{-1})	[Fe/H]	$\sigma_{([{\rm Fe/H}])}$	$w_{\rm MP}$	$T_{\rm eff}$ (K)	$\sigma_{(T_{\rm eff})}$ (K)	ξ (km s^{-1})	$\sigma_{(\xi)}$ (km s^{-1})	[Fe/H]	$\sigma_{([{\rm Fe/H}])}$	$w_{\rm MR}$
KIC10096113	4943	80	1.417	0.116	-0.661	0.054	0.000	4948	48	1.443	0.070	-0.717	0.018	1.000
KIC10328894	5031	39	1.525	0.047	-1.832	0.031	0.771	4973	59	1.539	0.067	-1.912	0.048	0.229
KIC10460723	4938	49	1.412	0.068	-1.213	0.025	0.017	4922	41	1.467	0.047	-1.273	0.021	0.983
KIC10737052	4998	50	1.454	0.064	-1.190	0.029	0.000	4973	42	1.478	0.047	-1.255	0.021	1.000
KIC10992126	4386	93	1.702	0.112	-0.646	0.067	0.000	4253	90	1.571	0.096	-0.607	0.062	1.000
KIC11563791	4996	75	1.368	0.128	-1.070	0.046	0.000	4974	54	1.326	0.069	-1.114	0.023	1.000
KIC11566038	5002	45	1.417	0.052	-1.391	0.030	0.223	4998	47	1.461	0.057	-1.432	0.031	0.777
KIC12017985	4962	39	1.639	0.043	-1.823	0.028	0.770	4889	56	1.591	0.066	-1.914	0.044	0.230
KIC12017985-17	4947	38	1.646	0.038	-1.852	0.027	0.809	4868	61	1.601	0.076	-1.946	0.050	0.191
KIC12253381	4947	46	1.511	0.047	-1.519	0.027	0.380	4906	53	1.513	0.052	-1.579	0.040	0.620
HD122563[a]	4636	···	2.05	···	-2.599	···	···	4434	62	3.613	0.060	-2.851	0.029	···

[a]HD122563 is included for completeness. It is not used for the other figures.

Appendix 5.C Uncertainties of the stellar parameters of the standard stars

Abundances and stellar parameters are precisely determined in this study adopting differential abundance analyses. While the relative abundance/parameters among our sample should not be significantly affected by the uncertainties of stellar parameters of the standard stars, the absolute scale totally depends on the abundance/stellar parameters of the standard stars. In this section, we explore how the change in stellar parameters of the standard stars affects the absolute scale of our program stars. One has to take into account these effects when they try to quantitatively compare our results with different studies.

We re-carry out analyses for a subset of stars adopting stellar parameters of the standard stars with offsets that correspond to their uncertainties (Tables 5.9 & 5.10). We select three stars as the subset for each reference star to cover the wide metallicity range. It is clear that the absolute scale does depend on the adopted stellar parameters of the standard star. However, we emphasize that since the change is systematic, we are almost free from this effect as long as we discuss abundance trends among our sample. These effects are only important when one tries to compare our results with other studies.

Tables 5.9 and 5.10 also include the number of lines used to derive the abundance of the reference star and the scatter of abundances derived from individual lines. Readers may derive uncertainties of the abundance of the reference star by quadratically summing $\sigma_{\rm sct}/\sqrt{N_{\rm line}}$ and shifts in abundances caused by those in stellar parameters ("ref" columns). Since the abundance of the reference star determines our abundance scale, readers may add the obtained values to the reported uncertainties in Table 5.7 for a comparison purpose.

Table 5.9. Change of the stellar parameters/abundances due to the stellar parameters of HD122563

			$\Delta T_{\rm eff} = 36\,{\rm K}$[a]				$\Delta \log g = 0.007$[a]				$\Delta\xi = 0.08$[b]				Δ[Fe/H] $= 0.016$[b]			
	$n_{\rm line}$[c]	$\sigma_{\rm sct}$[c]	ref	(1)	(2)	(3)	ref	(1)	(2)	(3)	ref	(1)	(2)	(3)	ref	(1)	(2)	(3)
$T_{\rm eff}$			36	48	51	46	0	3	4	0	0	-5	-1	2	0	5	3	1
$\log g$			0.00	0.00	0.00	0.00	0.01	-0.00	0.00	0.00	0.00	0.00	0.00	0.00	0.00	0.00	0.00	0.00
ξ			0.00	0.00	0.01	0.02	0.00	0.00	0.01	0.00	0.08	0.09	0.06	0.06	0.00	0.00	0.00	0.00
[Fe/H]			0.00	0.01	0.00	0.00	0.00	0.00	0.00	-0.00	0.00	-0.00	-0.01	-0.01	0.02	0.02	0.02	0.02
BaII	3	0.08	0.02	0.03	0.02	0.02	0.00	0.00	0.00	0.00	-0.00	-0.02	-0.03	-0.03	0.00	0.01	0.01	0.01
CH	1	0.00	0.06	0.09	0.07	0.05	-0.00	0.00	0.01	-0.00	0.00	-0.01	-0.00	-0.01	0.01	0.02	0.01	0.01
CaI	28	0.07	0.03	0.03	0.03	0.04	0.00	0.00	0.00	0.00	-0.00	-0.00	-0.01	-0.01	0.00	0.00	0.00	-0.00
CeII	1	0.00	0.02	···	0.02	0.02	0.00	···	0.00	0.00	0.00	···	-0.01	-0.01	0.00	···	0.00	0.01
CoI	4	0.05	0.05	0.07	0.07	0.07	0.00	0.00	0.01	0.00	-0.01	-0.02	-0.02	-0.01	0.00	0.01	-0.00	0.00
CrI	13	0.10	0.05	0.06	0.06	0.06	-0.00	0.00	0.00	0.00	-0.00	-0.01	-0.01	-0.01	-0.00	0.00	0.00	-0.00
CrII	10	0.10	-0.01	-0.01	-0.01	-0.01	0.00	0.00	-0.00	0.00	-0.00	-0.00	-0.00	-0.01	0.00	0.00	0.00	0.00
CuI	1	0.00	0.05	···	0.06	0.06	0.00	···	0.00	0.00	0.00	···	-0.00	0.00	-0.00	···	0.00	0.00
EuII	1	0.00	0.02	0.03	0.03	0.02	0.00	0.00	0.00	0.00	-0.00	-0.00	-0.00	-0.00	0.00	0.01	0.01	0.01
FeI	158	0.12	0.04	0.05	0.05	0.05	0.00	0.00	0.00	0.00	-0.01	-0.02	-0.02	-0.02	0.00	0.00	0.00	0.00
FeII	35	0.05	-0.01	0.00	-0.01	-0.01	0.00	-0.00	-0.00	0.00	-0.00	-0.00	-0.01	-0.02	0.00	0.00	0.00	0.00
LaII	1	0.00	0.02	0.03	0.03	0.02	0.00	0.00	0.00	0.00	0.00	-0.01	-0.01	-0.01	0.00	0.01	0.01	0.00
MgI	4	0.09	0.02	0.03	0.03	0.02	-0.00	0.00	0.00	0.00	-0.01	-0.01	-0.01	-0.01	-0.00	0.00	0.00	-0.00
MnI	7	0.05	0.04	0.04	0.05	0.05	-0.00	0.00	0.00	-0.00	-0.00	-0.01	-0.00	-0.01	-0.00	0.00	0.00	0.00
NaI	1	0.00	0.02	···	0.03	0.03	0.00	···	0.00	0.00	-0.00	···	-0.00	0.00	0.00	···	0.00	0.00

Table 5.9 (cont'd)

			$\Delta T_{\rm eff} = 36$ K[a]			$\Delta \log g = 0.007$[a]				$\Delta\xi = 0.08$[b]				Δ[Fe/H] $= 0.016$[b]			
	$n_{\rm line}$[c]	$\sigma_{\rm sct}$[c]	ref	(1)	(2)	(3)	ref	(1)	(2)	(3)	ref	(1)	(2)	(3)	ref	(1)	(2)	(3)
NdII	2	0.01	0.02	···	0.03	0.02	0.00	···	0.00	0.00	-0.00	···	-0.00	-0.01	0.00	···	0.01	0.00
NiI	27	0.06	0.03	0.04	0.04	0.04	-0.00	0.00	0.00	0.00	-0.00	-0.01	-0.00	-0.00	-0.00	0.00	-0.00	0.00
ScII	14	0.10	0.01	0.03	0.01	0.01	0.00	0.00	-0.00	0.00	-0.00	-0.00	-0.01	-0.01	0.00	0.00	0.00	0.00
SiI	4	0.04	0.02	0.02	0.02	0.02	0.00	0.00	0.00	0.00	-0.00	-0.00	-0.00	-0.00	-0.00	0.00	0.00	0.00
SmII	1	0.00	0.02	···	0.02	0.02	0.00	···	0.00	0.00	0.00	···	-0.00	-0.00	0.00	···	0.00	0.01
TiI	46	0.08	0.06	0.07	0.07	0.07	0.00	0.00	0.01	-0.00	-0.00	-0.01	-0.01	-0.01	-0.00	0.00	0.00	-0.00
TiII	26	0.08	0.00	0.01	0.00	0.01	0.00	0.00	0.00	-0.00	-0.00	-0.01	-0.01	-0.01	0.00	0.00	0.00	0.00
VI	6	0.12	0.06	···	0.08	0.07	0.00	···	0.01	0.00	0.00	···	-0.00	0.00	-0.00	···	0.00	-0.00
YII	9	0.09	0.01	0.03	0.02	0.01	0.00	0.00	0.00	-0.00	0.00	0.00	-0.00	-0.01	0.00	0.00	0.00	0.00
ZnI	2	0.01	0.01	0.02	0.01	0.01	0.00	0.00	0.00	0.00	-0.00	-0.00	-0.01	-0.01	0.00	0.00	0.00	0.00

Note. — (1): KIC5439372 ([Fe/H] $= -2.53$), (2): KIC12017985 ([Fe/H] $= -1.87$), (3): KIC11566038 ([Fe/H] $= -1.36$). For the elemental abundances we show the results for [X/H].

[a]Karovicova et al. (2018) and Creevey et al. (2019).

[b]Derived in this study. We consider the effects of the uncertainties of the other parameters.

[c]The number of lines used and the scatter among abundances derived from individual lines.

Table 5.10. Change of the stellar parameters/abundances due to the stellar parameters of KIC9583607

			$\Delta T_{\rm eff} = 89$ K[a]				$\Delta \log g = 0.010$[b]				$\Delta\xi = 0.09$[b]				Δ[Fe/H] $= 0.065$[b]			
	$n_{\rm line}$[c]	$\sigma_{\rm sct}$[c]	ref	(1)	(2)	(3)	ref	(1)	(2)	(3)	ref	(1)	(2)	(3)	ref	(1)	(2)	(3)
$T_{\rm eff}$			89	85	84	79	0	5	1	9	0	6	-5	-2	0	-1	0	-5
$\log g$			0.00	0.00	0.00	0.00	0.01	0.00	0.00	0.00	0.00	0.00	0.00	0.00	0.00	0.00	0.00	0.00
ξ			0.00	0.00	0.02	-0.01	0.00	0.01	0.00	0.01	0.09	0.08	0.07	0.07	0.00	0.00	-0.00	-0.02
[Fe/H]			0.00	0.00	0.00	0.00	0.00	0.00	0.00	0.00	0.00	0.01	0.02	0.03	0.06	0.07	0.06	0.06
BaII	3	0.08	0.02	0.03	0.04	0.04	0.00	-0.00	0.00	0.00	-0.08	-0.06	-0.05	-0.06	0.01	0.02	0.03	0.02
CH	1	0.00	0.07	0.06	0.11	0.10	0.00	0.00	0.00	0.01	-0.00	0.01	0.01	0.01	0.04	0.06	0.04	0.03
CaI	25	0.14	0.08	0.09	0.08	0.06	0.00	0.00	0.00	0.01	-0.03	-0.02	-0.02	-0.00	-0.01	-0.01	-0.01	-0.01
CeII	4	0.10	0.02	0.03	0.04	0.03	0.00	0.00	0.00	0.01	-0.01	-0.01	0.01	0.01	0.02	0.02	0.02	0.01
CoI	4	0.06	0.11	0.11	0.12	0.11	0.00	0.01	0.00	0.01	-0.01	0.00	0.01	0.02	0.00	0.01	-0.01	-0.01
CrI	9	0.07	0.13	0.14	0.12	0.11	0.00	-0.00	0.00	0.01	-0.06	-0.05	-0.03	-0.01	-0.01	-0.01	-0.01	-0.01
CrII	11	0.24	-0.04	-0.04	-0.01	-0.03	0.00	0.00	0.00	-0.00	-0.03	-0.03	0.00	0.00	0.01	0.01	0.01	0.01
CuI	1	0.00	0.12	0.11	0.11	0.10	0.00	0.00	0.00	0.01	-0.03	-0.01	-0.01	-0.00	-0.00	0.01	-0.00	-0.01
EuII	3	0.08	-0.00	0.01	0.02	0.01	0.00	0.00	0.00	0.00	-0.00	0.00	0.01	0.01	0.02	0.02	0.02	0.01
FeI	121	0.14	0.10	0.10	0.10	0.09	0.00	0.00	0.00	0.01	-0.03	-0.02	-0.01	-0.00	-0.00	0.00	-0.00	-0.01
FeII	23	0.10	-0.03	-0.03	-0.01	-0.01	0.00	-0.00	0.00	-0.00	-0.03	-0.02	0.00	-0.01	0.01	0.02	0.02	0.01
LaII	3	0.04	0.02	0.03	0.04	0.03	0.00	0.00	0.00	0.01	-0.00	0.00	0.01	0.01	0.02	0.02	0.02	0.01
MgI	5	0.11	0.04	0.05	0.04	0.03	0.00	0.00	0.00	0.00	-0.00	0.01	0.01	0.00	0.00	0.01	-0.00	-0.01
MnI	6	0.07	0.10	0.11	0.09	0.10	0.00	0.00	0.00	0.01	-0.04	-0.02	0.00	0.01	-0.01	-0.00	-0.00	-0.01
NaI	1	0.00	0.06	0.08	0.06	0.04	-0.00	0.00	0.00	0.01	-0.02	-0.02	-0.01	-0.00	-0.00	0.00	-0.00	-0.00

Table 5.10 (cont'd)

			$\Delta T_{\rm eff} = 89$ K[a]			$\Delta \log g = 0.010$[b]				$\Delta\xi = 0.09$[b]				Δ[Fe/H] $= 0.065$[b]			
	$n_{\rm line}$[c]	$\sigma_{\rm sct}$[c]	ref	(1)	(2)	(3)	ref	(1)	(2)	(3)	ref	(1)	(2)	(3)	ref	(1)	(2)	(3)
NdII	6	0.07	0.03	0.04	0.05	0.04	0.01	-0.00	0.00	0.00	-0.01	-0.03	0.00	0.00	0.02	0.02	0.02	0.01
NiI	32	0.15	0.10	0.10	0.10	0.10	0.00	0.00	0.00	0.01	-0.03	-0.01	-0.01	0.00	-0.00	0.01	-0.01	-0.01
OI	1	0.00	0.02	0.02	0.04	···	0.00	0.00	0.00	···	-0.00	0.00	0.00	···	0.02	0.02	0.02	···
ScII	9	0.07	-0.01	-0.00	0.01	0.00	0.00	-0.00	0.00	0.00	-0.03	-0.02	-0.01	0.01	0.01	0.01	0.01	0.01
SiI	7	0.12	0.03	0.02	0.04	0.03	0.00	0.00	0.00	0.00	-0.01	-0.00	0.00	0.00	0.00	0.01	0.00	0.00
SmII	1	0.00	0.02	0.03	0.04	0.03	0.00	0.00	0.00	0.00	-0.01	-0.01	0.00	0.00	0.02	0.02	0.02	0.01
TiI	41	0.17	0.13	0.15	0.12	0.11	0.00	0.00	0.00	0.01	-0.02	-0.01	-0.01	0.01	-0.00	-0.00	-0.01	-0.01
TiII	12	0.17	0.00	0.01	0.02	0.01	0.00	-0.00	0.00	0.00	-0.02	-0.02	0.00	0.01	0.01	0.02	0.02	0.01
VI	10	0.16	0.13	0.14	0.12	0.11	0.00	0.01	0.00	0.01	-0.00	0.01	-0.00	0.01	-0.00	0.00	-0.01	-0.01
YII	6	0.09	0.01	0.02	0.02	0.01	0.00	-0.00	0.00	0.00	-0.06	-0.05	-0.00	-0.00	0.01	0.02	0.02	0.02
ZnI	2	0.01	-0.00	-0.01	0.02	0.01	0.00	-0.00	0.00	0.00	-0.04	-0.03	-0.01	-0.00	0.01	0.01	0.01	0.01

Note. — (1): KIC8350894 ([Fe/H] $= -0.85$), (2): KIC11566038 ([Fe/H] $= -1.36$), (3): KIC12017985 ([Fe/H] $= -1.87$)

[a]From APOGEE DR14 catalog.

[b]Derived in this study. We consider the effects of the uncertainties of the other parameters. For the elemental abundances we show the results for [X/H].

[c]The number of lines used and the scatter among abundances derived from individual lines.

Chapter 6

Conclusion & Outlook

We obtained the following implications about the stellar populations in the Galactic halo: i) Apparent inconsistency between chemical abundance and ages of some red giant stars is mainly due to binary interaction. This result confirms the validity of our standard understandings of chemical evolution (Chapter 3). ii) The high-energy retrograde kinematic substructure (the high-E retrograde halo) shows different chemical abundance than Gaia Enceladus or ω Centauri. This indicates that the high-E retrograde halo is caused by an accretion of a dwarf galaxy that is independent from Gaia Enceladus or ω Centauri. Its very low α-element abundances suggest its long star formation timescale (Chapter 4). iii) Asteroseismic mass estimates hold an internal consistency among less evolved red giant branch stars even for low metallicity stars, although there remains systematic offset. The formation time scale of the halo is constrained to < 2 Gyr from the lack of significant mass dispersion among halo stars. Chemical abundance constrains the formation timescale to $100 - 300$ Myr for the low-α halo population. Asteroseismic mass estimates additionally indicate that the average formation epochs do not differ more than 4 Gyr between the low-α and high-α halo populations. These estimates are for red giant branch stars beyond the solar neighbourhood but are consistent with the results obtained from nearby turn-off stars (Chapter 5).

Throughout this thesis, I have shown that stellar chemical abundance becomes even more powerful in understanding the stellar populations in the Galaxy when it is combined with other types of information, such as stellar kinematics or asteroseismology, and/or when it is derived with high-precision through a line-by-line abundance analysis. High-precision chemical abundance of elements having different nucleosynthesis origins enables us to identify stars having anomalous abundance and constrain their origin (Chapter 3 and 5). When chemical abundance is combined with stellar kinematics, even if the abundance is not determined precisely, a signature of a past galaxy accretion can be obtained (Chapter 4). The three types of the

information, abundance, kinematics, and asteroseismology, are combined for halo stars beyond the solar neighbourhood for the first time in Chapter 5. Even though Chapter 5 is still in the very early phase of applying asteroseismology to halo stars, we put a constraint on the timescale and epoch of star formation of halo stellar populations.

Now we are entering in the era of big surveys; GALAH and APOGEE have been providing precise chemical abundances for a large number of stars using multi-object spectrographs; Gaia is providing astrometric measurements for more than one billion stars with unprecedented precision; *CoRoT* and *Kepler* have enabled us to apply asteroseismology for a large number of red giant stars. This tendency looks going to continue; Gaia is going to improve the precision and start to provide metallicity estimates; additional multi-object high-resolution spectroscopic surveys such as WEAVE or 4MOST are going to start; TESS, PLATO, and WFIRST will provide data for which asteroseismic analysis can be carried out. These surveys will open a window to further extend the studies like those presented in this thesis.

The understanding of the Milky Way accretion history is experiencing revolution thanks to the Gaia mission. Currently most of the studies focus on analysis of stellar kinematics and, at most, metallicity and α-element abundances. However, chemical abundance information of more elements, such as s-/r-process elements, is necessary to make a complete picture of the Milky Way formation. As the number of identified building blocks increases, their average mass would become smaller. Such small building blocks would have experienced star formation quenching at the time of cosmic reionization. We might not be able to see α-elements abundance difference among them since Type Ia supernovae might have no time to contribute to the chemical evolution in any of such systems before the quenching. Nucleosynthesis processes that might occur with a shorter delay time, such as r-process elements production by neutron star mergers, would be necessary.

High-precision abundance on a carefully selected sample is also of great importance. Abundance difference between different building blocks could be very small as we showed in Chapter 4. Therefore, contamination or less-precise abundances would easily smear out any abundance signatures. Currently high-precision abundance have been provided only for the two major halo populations, but we need to explore other populations.

The ongoing spectroscopic surveys still have difficulties in deriving chemical abundances especially for low-metallicity stars mainly due to the limited wavelength coverage. Most of planned high-resolution spectroscopic surveys are in the planning phase and it is not yet clear if they observe sufficient number of stars for each subpopulation and if they can achieve high enough precision for low-metallicity stars. However, if the wavelength coverage and targets are carefully selected, it is in principle possible to achieve high precision, and hence the future surveys have a power to make another revolution

in this research field. This thesis is an example of studies showing the importance of high-precision abundance and its combination with Gaia data or asteroseismology to study stellar populations in the Milky Way. Such studies will have impacts on the strategy of the near future spectroscopic surveys and are needed before the surveys start.

Bibliography

Abbott, B. P., Abbott, R., Abbott, T. D., et al. 2017, ApJ, 848, L12, doi: 10.3847/2041-8213/aa91c9

Adams, T. F. 1976, A&A, 50, 461

Aerts, C., Christensen-Dalsgaard, J., & Kurtz, D. W. 2010, Asteroseismology

Aldenius, M., Lundberg, H., & Blackwell-Whitehead, R. 2009, A&A, 502, 989, doi: 10.1051/0004-6361/200911844

Alpher, R. A., Bethe, H., & Gamow, G. 1948, Physical Review, 73, 803, doi: 10.1103/PhysRev.73.803

Alpher, R. A., & Herman, R. C. 1948, Physical Review, 74, 1737, doi: 10.1103/PhysRev.74.1737

Amarsi, A. M., Asplund, M., Collet, R., & Leenaarts, J. 2016a, MNRAS, 455, 3735, doi: 10.1093/mnras/stv2608

Amarsi, A. M., Lind, K., Asplund, M., Barklem, P. S., & Collet, R. 2016b, MNRAS, 463, 1518, doi: 10.1093/mnras/stw2077

Amarsi, A. M., Nissen, P. E., & Skúladóttir, Á. 2019, A&A, 630, A104, doi: 10.1051/0004-6361/201936265

Anders, F., Chiappini, C., Rodrigues, T. S., et al. 2017, A&A, 597, A30, doi: 10.1051/0004-6361/201527204

Aoki, W., Barklem, P. S., Beers, T. C., et al. 2009, ApJ, 698, 1803, doi: 10.1088/0004-637X/698/2/1803

Aoki, W., Tominaga, N., Beers, T. C., Honda, S., & Lee, Y. S. 2014, Science, 345, 912, doi: 10.1126/science.1252633

Arentsen, A., Starkenburg, E., Martin, N. F., et al. 2020, MNRAS, 491, L11, doi: 10.1093/mnrasl/slz156

Argast, D., Samland, M., Thielemann, F.-K., & Qian, Y.-Z. 2004, A&A, 416, 997, doi: 10.1051/0004-6361:20034265

Arlandini, C., Käppeler, F., Wisshak, K., et al. 1999, ApJ, 525, 886, doi: 10.1086/307938

Asplund, M., Grevesse, N., Sauval, A. J., & Scott, P. 2009, ARA&A, 47, 481, doi: 10.1146/annurev.astro.46.060407.145222

Astropy Collaboration, Robitaille, T. P., Tollerud, E. J., et al. 2013, A&A, 558, A33, doi: 10.1051/0004-6361/201322068

Auvergne, M., Bodin, P., Boisnard, L., et al. 2009, A&A, 506, 411, doi: 10.1051/0004-6361/200810860

Aver, E., Olive, K. A., & Skillman, E. D. 2015, J. Cosmology Astropart. Phys., 7, 011, doi: 10.1088/1475-7516/2015/07/011

Bailer-Jones, C. A. L. 2015, PASP, 127, 994, doi: 10.1086/683116

Bailer-Jones, C. A. L., Rybizki, J., Fouesneau, M., Mantelet, G., & Andrae, R. 2018, AJ, 156, 58, doi: 10.3847/1538-3881/aacb21

Balashev, S. A., Zavarygin, E. O., Ivanchik, A. V., Telikova, K. N., & Varshalovich, D. A. 2016, MNRAS, 458, 2188, doi: 10.1093/mnras/stw356

Barbá, R. H., Minniti, D., Geisler, D., et al. 2019, ApJ, 870, L24, doi: 10.3847/2041-8213/aaf811

Bard, A., Kock, A., & Kock, M. 1991, A&A, 248, 315

Bard, A., & Kock, M. 1994, A&A, 282, 1014

Barklem, P. S., Stempels, H. C., Allende Prieto, C., et al. 2002, A&A, 385, 951, doi: 10.1051/0004-6361:20020163

Battistini, C., & Bensby, T. 2016, A&A, 586, A49, doi: 10.1051/0004-6361/201527385

Beers, T. C., & Christlieb, N. 2005, ARA&A, 43, 531, doi: 10.1146/annurev.astro.42.053102.134057

Belokurov, V., Erkal, D., Evans, N. W., Koposov, S. E., & Deason, A. J. 2018, MNRAS, 478, 611, doi: 10.1093/mnras/sty982

Belokurov, V., Sanders, J. L., Fattahi, A., et al. 2019, arXiv e-prints, arXiv:1909.04679. https://arxiv.org/abs/1909.04679

Belokurov, V., Zucker, D. B., Evans, N. W., et al. 2006, ApJ, 642, L137, doi: 10.1086/504797

Bensby, T., Feltzing, S., & Oey, M. S. 2014, A&A, 562, A71, doi: 10.1051/0004-6361/201322631

Bernard, E. J., Ferguson, A. M. N., Schlafly, E. F., et al. 2016, MNRAS, 463, 1759, doi: 10.1093/mnras/stw2134

Binney, J., Gerhard, O. E., Stark, A. A., Bally, J., & Uchida, K. I. 1991, MNRAS, 252, 210, doi: 10.1093/mnras/252.2.210

Binney, J., & Tremaine, S. 2008, Galactic Dynamics: Second Edition

Blackwell, D. E., Booth, A. J., Haddock, D. J., Petford, A. D., & Leggett, S. K. 1986, MNRAS, 220, 549, doi: 10.1093/mnras/220.3.549

Blackwell, D. E., Petford, A. D., & Shallis, M. J. 1979, MNRAS, 186, 657, doi: 10.1093/mnras/186.4.657

Blackwell, D. E., Petford, A. D., Shallis, M. J., & Simmons, G. J. 1980, MNRAS, 191, 445, doi: 10.1093/mnras/191.3.445

—. 1982a, MNRAS, 199, 43, doi: 10.1093/mnras/199.1.43

Blackwell, D. E., Petford, A. D., & Simmons, G. J. 1982b, MNRAS, 201, 595, doi: 10.1093/mnras/201.3.595

Bland-Hawthorn, J., & Gerhard, O. 2016, ARA&A, 54, 529, doi: 10.1146/annurev-astro-081915-023441

Blitz, L., & Spergel, D. N. 1991, ApJ, 379, 631, doi: 10.1086/170535

Bonaca, A., Conroy, C., Wetzel, A., Hopkins, P. F., & Kereš, D. 2017, ApJ, 845, 101, doi: 10.3847/1538-4357/aa7d0c

Bonifacio, P., Sbordone, L., Caffau, E., et al. 2012, A&A, 542, A87, doi: 10.1051/0004-6361/201219004

Booth, A. J., Blackwell, D. E., Petford, A. D., & Shallis, M. J. 1984, MNRAS, 208, 147, doi: 10.1093/mnras/208.1.147

Bovy, J. 2015, ApJS, 216, 29, doi: 10.1088/0067-0049/216/2/29

Bovy, J., Rix, H.-W., Schlafly, E. F., et al. 2016, ApJ, 823, 30, doi: 10.3847/0004-637X/823/1/30

Brogaard, K., Jessen-Hansen, J., Handberg, R., et al. 2016, Astronomische Nachrichten, 337, 793, doi: 10.1002/asna.201612374

Bromm, V. 2013, Reports on Progress in Physics, 76, 112901, doi: 10.1088/0034-4885/76/11/112901

Brown, T. M., Gilliland, R. L., Noyes, R. W., & Ramsey, L. W. 1991, ApJ, 368, 599, doi: 10.1086/169725

Buder, S., Asplund, M., Duong, L., et al. 2018, MNRAS, doi: 10.1093/mnras/sty1281

Buder, S., Lind, K., Ness, M. K., et al. 2019, A&A, 624, A19, doi: 10.1051/0004-6361/201833218

Burles, S., & Tytler, D. 1998a, ApJ, 499, 699, doi: 10.1086/305667

—. 1998b, ApJ, 507, 732, doi: 10.1086/306341

Caffau, E., Bonifacio, P., François, P., et al. 2011, Nature, 477, 67, doi: 10.1038/nature10377

Carollo, D., Beers, T. C., Lee, Y. S., et al. 2007, Nature, 450, 1020, doi: 10.1038/nature06460

Carollo, D., Beers, T. C., Placco, V. M., et al. 2016, Nature Physics, 12, 1170, doi: 10.1038/nphys3874

Carollo, D., Chiba, M., Ishigaki, M., et al. 2019, ApJ, 887, 22, doi: 10.3847/1538-4357/ab517c

Carretta, E., Bragaglia, A., Gratton, R. G., et al. 2009, A&A, 505, 117, doi: 10.1051/0004-6361/200912096

Casagrande, L., & VandenBerg, D. A. 2014, MNRAS, 444, 392, doi: 10.1093/mnras/stu1476

Casagrande, L., Silva Aguirre, V., Schlesinger, K. J., et al. 2016, MNRAS, 455, 987, doi: 10.1093/mnras/stv2320

Casamiquela, L., Carrera, R., Balaguer-Núñez, L., et al. 2018, A&A, 610, A66, doi: 10.1051/0004-6361/201732024

Casey, A. R., Kennedy, G. M., Hartle, T. R., & Schlaufman, K. C. 2018, MNRAS, 478, 2812, doi: 10.1093/mnras/sty1208

Castelli, F., & Kurucz, R. L. 2003, in IAU Symposium, Vol. 210, Modelling of Stellar Atmospheres, ed. N. Piskunov, W. W. Weiss, & D. F. Gray, A20

Castelli, F., & Kurucz, R. L. 2004, ArXiv Astrophysics e-prints

Cayrel, R., Hill, V., Beers, T. C., et al. 2001, Nature, 409, 691. https://arxiv.org/abs/astro-ph/0104357

Chaplin, W. J., & Miglio, A. 2013, ARA&A, 51, 353, doi: 10.1146/annurev-astro-082812-140938

Charbonnel, C., & Primas, F. 2005, A&A, 442, 961, doi: 10.1051/0004-6361:20042491

Chen, M. C., Herwig, F., Denissenkov, P. A., & Paxton, B. 2014, MNRAS, 440, 1274, doi: 10.1093/mnras/stu108

Chiaki, G., Tominaga, N., & Nozawa, T. 2017, MNRAS, 472, L115, doi: 10.1093/mnrasl/slx163

Chiappini, C., Anders, F., Rodrigues, T. S., et al. 2015, A&A, 576, L12, doi: 10.1051/0004-6361/201525865

Chiba, M., & Beers, T. C. 2000, AJ, 119, 2843, doi: 10.1086/301409

Choi, J., Dotter, A., Conroy, C., et al. 2016, ApJ, 823, 102, doi: 10.3847/0004-637X/823/2/102

Choplin, A., Hirschi, R., Meynet, G., et al. 2018, A&A, 618, A133, doi: 10.1051/0004-6361/201833283

Choplin, A., Tominaga, N., & Ishigaki, M. N. 2019, arXiv e-prints, arXiv:1910.01366. https://arxiv.org/abs/1910.01366

Clark, P. C., Glover, S. C. O., Klessen, R. S., & Bromm, V. 2011a, ApJ, 727, 110, doi: 10.1088/0004-637X/727/2/110

Clark, P. C., Glover, S. C. O., Smith, R. J., et al. 2011b, Science, 331, 1040, doi: 10.1126/science.1198027

Coc, A., Vangioni-Flam, E., Cassé, M., & Rabiet, M. 2002, Phys. Rev. D, 65, 043510, doi: 10.1103/PhysRevD.65.043510

Conselice, C. J. 2014, ARA&A, 52, 291, doi: 10.1146/annurev-astro-081913-040037

Cooke, R. J., Pettini, M., Jorgenson, R. A., Murphy, M. T., & Steidel, C. C. 2014, ApJ, 781, 31, doi: 10.1088/0004-637X/781/1/31

Cooke, R. J., Pettini, M., Nollett, K. M., & Jorgenson, R. 2016, ApJ, 830, 148, doi: 10.3847/0004-637X/830/2/148

Cooke, R. J., Pettini, M., & Steidel, C. C. 2018, ApJ, 855, 102, doi: 10.3847/1538-4357/aaab53

Cowan, J. J., Sneden, C., Lawler, J. E., et al. 2019, arXiv e-prints, arXiv:1901.01410. https://arxiv.org/abs/1901.01410

Creevey, O., Grundahl, F., Thévenin, F., et al. 2019, A&A, 625, A33, doi: 10.1051/0004-6361/201834721

Cui, X.-Q., Zhao, Y.-H., Chu, Y.-Q., et al. 2012, Research in Astronomy and Astrophysics, 12, 1197, doi: 10.1088/1674-4527/12/9/003

Cutri, R. M., Skrutskie, M. F., van Dyk, S., et al. 2003, VizieR Online Data Catalog, 2246

Cyburt, R. H., Fields, B. D., Olive, K. A., & Yeh, T.-H. 2016, Reviews of Modern Physics, 88, 015004, doi: 10.1103/RevModPhys.88.015004

da Silva, R., Porto de Mello, G. F., Milone, A. C., et al. 2012, A&A, 542, A84, doi: 10.1051/0004-6361/201118751

Das, P., Williams, A., & Binney, J. 2016, MNRAS, 463, 3169, doi: 10.1093/mnras/stw2167

De Cat, P., Fu, J. N., Ren, A. B., et al. 2015, ApJS, 220, 19, doi: 10.1088/0067-0049/220/1/19

Deason, A. J., Belokurov, V., Koposov, S. E., & Lancaster, L. 2018, ApJ, 862, L1, doi: 10.3847/2041-8213/aad0ee

Den Hartog, E. A., Lawler, J. E., Sneden, C., & Cowan, J. J. 2003, ApJS, 148, 543, doi: 10.1086/376940

Den Hartog, E. A., Lawler, J. E., Sobeck, J. S., Sneden, C., & Cowan, J. J. 2011, ApJS, 194, 35, doi: 10.1088/0067-0049/194/2/35

Di Matteo, P., Haywood, M., Lehnert, M. D., et al. 2018, arXiv e-prints, arXiv:1812.08232. https://arxiv.org/abs/1812.08232

Di Matteo, T., Springel, V., & Hernquist, L. 2005, Nature, 433, 604, doi: 10.1038/nature03335

Dotter, A. 2016, ApJS, 222, 8, doi: 10.3847/0067-0049/222/1/8

Drout, M. R., Piro, A. L., Shappee, B. J., et al. 2017, Science, 358, 1570, doi: 10.1126/science.aaq0049

Edvardsson, B., Andersen, J., Gustafsson, B., et al. 1993, A&A, 275, 101

Emerick, A., Mac Low, M.-M., Grcevich, J., & Gatto, A. 2016, ApJ, 826, 148, doi: 10.3847/0004-637X/826/2/148

Epstein, C. R., Elsworth, Y. P., Johnson, J. A., et al. 2014, ApJ, 785, L28, doi: 10.1088/2041-8205/785/2/L28

Feltzing, S., Howes, L. M., McMillan, P. J., & Stonkutė, E. 2017, MNRAS, 465, L109, doi: 10.1093/mnrasl/slw209

Fernández, V., Terlevich, E., Díaz, A. I., & Terlevich, R. 2019, MNRAS, 487, 3221, doi: 10.1093/mnras/stz1433

Fernández, V., Terlevich, E., Díaz, A. I., Terlevich, R., & Rosales-Ortega, F. F. 2018, MNRAS, 478, 5301, doi: 10.1093/mnras/sty1206

Fernández-Alvar, E., Fernández-Trincado, J. G., Moreno, E., et al. 2018, ArXiv e-prints. https://arxiv.org/abs/1807.07269

Feuillet, D. K., Bovy, J., Holtzman, J., et al. 2016, ApJ, 817, 40, doi: 10.3847/0004-637X/817/1/40

Fields, B. D. 2011, Annual Review of Nuclear and Particle Science, 61, 47, doi: 10.1146/annurev-nucl-102010-130445

Fields, B. D., Olive, K. A., Yeh, T.-H., & Young, C. 2019, arXiv e-prints, arXiv:1912.01132. https://arxiv.org/abs/1912.01132

Fishlock, C. K., Yong, D., Karakas, A. I., et al. 2017, MNRAS, 466, 4672, doi: 10.1093/mnras/stx047

Foreman-Mackey, D. 2016, The Journal of Open Source Software, 24, doi: 10.21105/joss.00024

Foreman-Mackey, D., Hogg, D. W., Lang, D., & Goodman, J. 2013, PASP, 125, 306, doi: 10.1086/670067

Frebel, A., Johnson, J. L., & Bromm, V. 2007, MNRAS, 380, L40, doi: 10.1111/j.1745-3933.2007.00344.x

Frebel, A., & Norris, J. E. 2015, ARA&A, 53, 631, doi: 10.1146/annurev-astro-082214-122423

Freeman, K., & Bland-Hawthorn, J. 2002, ARA&A, 40, 487, doi: 10.1146/annurev.astro.40.060401.093840

Fu, X., Bressan, A., Molaro, P., & Marigo, P. 2015, MNRAS, 452, 3256, doi: 10.1093/mnras/stv1384

Gaia Collaboration, Prusti, T., de Bruijne, J. H. J., et al. 2016a, A&A, 595, A1, doi: 10.1051/0004-6361/201629272

Gaia Collaboration, Brown, A. G. A., Vallenari, A., et al. 2016b, A&A, 595, A2, doi: 10.1051/0004-6361/201629512

—. 2018, A&A, 616, A1, doi: 10.1051/0004-6361/201833051

Gaulme, P., McKeever, J., Jackiewicz, J., et al. 2016, ApJ, 832, 121, doi: 10.3847/0004-637X/832/2/121

Gilliland, R. L., Brown, T. M., Christensen-Dalsgaard, J., et al. 2010, PASP, 122, 131, doi: 10.1086/650399

Gómez, F. A., & Helmi, A. 2010, MNRAS, 401, 2285, doi: 10.1111/j.1365-2966.2009.15841.x

Gottlöber, S., Klypin, A., & Kravtsov, A. V. 2001, ApJ, 546, 223, doi: 10.1086/318248

Gravity Collaboration, Abuter, R., Amorim, A., et al. 2018, A&A, 615, L15, doi: 10.1051/0004-6361/201833718

Gray, D. F. 2008, The Observation and Analysis of Stellar Photospheres

Green, G. M., Schlafly, E. F., Finkbeiner, D. P., et al. 2015, ApJ, 810, 25, doi: 10.1088/0004-637X/810/1/25

Green, G. M., Schlafly, E. F., Finkbeiner, D., et al. 2018, MNRAS, 478, 651, doi: 10.1093/mnras/sty1008

Greif, T. H., Springel, V., White, S. D. M., et al. 2011, ApJ, 737, 75, doi: 10.1088/0004-637X/737/2/75

Griest, K., Whitmore, J. B., Wolfe, A. M., et al. 2010, ApJ, 708, 158, doi: 10.1088/0004-637X/708/1/158

Grillmair, C. J. 2006, ApJ, 645, L37, doi: 10.1086/505863

Gustafsson, B., Edvardsson, B., Eriksson, K., et al. 2008a, A&A, 486, 951, doi: 10.1051/0004-6361:200809724

—. 2008b, A&A, 486, 951, doi: 10.1051/0004-6361:200809724

Hampel, M., Stancliffe, R. J., Lugaro, M., & Meyer, B. S. 2016, ApJ, 831, 171, doi: 10.3847/0004-637X/831/2/171

Hannaford, P., Lowe, R. M., Grevesse, N., Biemont, E., & Whaling, W. 1982, ApJ, 261, 736, doi: 10.1086/160384

Hawkins, K., Masseron, T., Jofré, P., et al. 2016, A&A, 594, A43, doi: 10.1051/0004-6361/201628812

Haywood, M., Di Matteo, P., Lehnert, M. D., et al. 2018, ApJ, 863, 113, doi: 10.3847/1538-4357/aad235

Hekker, S., & Johnson, J. A. 2019, MNRAS, 487, 4343, doi: 10.1093/mnras/stz1554

Hekker, S., Gilliland, R. L., Elsworth, Y., et al. 2011, MNRAS, 414, 2594, doi: 10.1111/j.1365-2966.2011.18574.x

Helmi, A., Babusiaux, C., Koppelman, H. H., et al. 2018, Nature, 563, 85, doi: 10.1038/s41586-018-0625-x

Helmi, A., Veljanoski, J., Breddels, M. A., Tian, H., & Sales, L. V. 2017, A&A, 598, A58, doi: 10.1051/0004-6361/201629990

Helmi, A., White, S. D. M., de Zeeuw, P. T., & Zhao, H. 1999, Nature, 402, 53, doi: 10.1038/46980

Hill, V., Skúladóttir, Á., Tolstoy, E., et al. 2019, A&A, 626, A15, doi: 10.1051/0004-6361/201833950

Hinkle, K., Wallace, L., Valenti, J., & Harmer, D. 2000, Visible and Near Infrared Atlas of the Arcturus Spectrum 3727-9300 A, Vol. 2 (ASP)

Hirai, Y., Ishimaru, Y., Saitoh, T. R., et al. 2015, ApJ, 814, 41, doi: 10.1088/0004-637X/814/1/41

Hirano, S., & Bromm, V. 2017, MNRAS, 470, 898, doi: 10.1093/mnras/stx1220

—. 2018, MNRAS, 476, 3964, doi: 10.1093/mnras/sty487

Hirano, S., Hosokawa, T., Yoshida, N., et al. 2014, ApJ, 781, 60, doi: 10.1088/0004-637X/781/2/60

Holtzman, J. A., Shetrone, M., Johnson, J. A., et al. 2015, AJ, 150, 148, doi: 10.1088/0004-6256/150/5/148

Holtzman, J. A., Hasselquist, S., Shetrone, M., et al. 2018, AJ, 156, 125, doi: 10.3847/1538-3881/aad4f9

Hosokawa, T., Hirano, S., Kuiper, R., et al. 2016, ApJ, 824, 119, doi: 10.3847/0004-637X/824/2/119

Hotokezaka, K., Beniamini, P., & Piran, T. 2018, ArXiv e-prints. https://arxiv.org/abs/1801.01141

Hubble, E. 1929, Proceedings of the National Academy of Science, 15, 168, doi: 10.1073/pnas.15.3.168

Huber, D., Ireland, M. J., Bedding, T. R., et al. 2012, ApJ, 760, 32, doi: 10.1088/0004-637X/760/1/32

Hunter, J. D. 2007, Computing in Science Engineering, 9, 90, doi: 10.1109/MCSE.2007.55

Ibata, R. A., Gilmore, G., & Irwin, M. J. 1994, Nature, 370, 194, doi: 10.1038/370194a0

Ishigaki, M. N., Tominaga, N., Kobayashi, C., & Nomoto, K. 2018, ApJ, 857, 46, doi: 10.3847/1538-4357/aab3de

Ishimaru, Y., Wanajo, S., & Prantzos, S. 2015, ApJ

Ishiyama, T., Sudo, K., Yokoi, S., et al. 2016, ApJ, 826, 9, doi: 10.3847/0004-637X/826/1/9

Ivans, I. I., Simmerer, J., Sneden, C., et al. 2006, ApJ, 645, 613, doi: 10.1086/504069

Iwamoto, N., Umeda, H., Tominaga, N., Nomoto, K., & Maeda, K. 2005, Science, 309, 451, doi: 10.1126/science.1112997

Izotov, Y. I., Thuan, T. X., & Guseva, N. G. 2014, MNRAS, 445, 778, doi: 10.1093/mnras/stu1771

Izotov, Y. I., Thuan, T. X., & Stasińska, G. 2007, ApJ, 662, 15, doi: 10.1086/513601

Izzard, R. G., Preece, H., Jofre, P., et al. 2018, MNRAS, 473, 2984, doi: 10.1093/mnras/stx2355

Jean-Baptiste, I., Di Matteo, P., Haywood, M., et al. 2017, A&A, 604, A106, doi: 10.1051/0004-6361/201629691

Ji, A. P., Frebel, A., & Bromm, V. 2014, ApJ, 782, 95, doi: 10.1088/0004-637X/782/2/95

Ji, A. P., Frebel, A., Chiti, A., & Simon, J. D. 2016, Nature, 531, 610, doi: 10.1038/nature17425

Jofré, E., Petrucci, R., García, L., & Gómez, M. 2015, A&A, 584, L3, doi: 10.1051/0004-6361/201527337

Jofré, P., Jorissen, A., Van Eck, S., et al. 2016, A&A, 595, A60, doi: 10.1051/0004-6361/201629356

Johnson, C. I., & Pilachowski, C. A. 2010, ApJ, 722, 1373, doi: 10.1088/0004-637X/722/2/1373

Jones, E., Oliphant, T., Peterson, P., et al. 2001–, SciPy: Open source scientific tools for Python. http://www.scipy.org/

Jurić, M., Ivezić, Ž., Brooks, A., et al. 2008, ApJ, 673, 864, doi: 10.1086/523619

Kallinger, T., Weiss, W. W., Barban, C., et al. 2010a, A&A, 509, A77, doi: 10.1051/0004-6361/200811437

Kallinger, T., Mosser, B., Hekker, S., et al. 2010b, A&A, 522, A1, doi: 10.1051/0004-6361/201015263

Käppeler, F., Gallino, R., Bisterzo, S., & Aoki, W. 2011, Reviews of Modern Physics, 83, 157, doi: 10.1103/RevModPhys.83.157

Karakas, A. I., & Lugaro, M. 2016, ApJ, 825, 26, doi: 10.3847/0004-637X/825/1/26

Karovicova, I., White, T. R., Nordlander, T., et al. 2018, MNRAS, 475, L81, doi: 10.1093/mnrasl/sly010

Kelleher, D. E., & Podobedova, L. I. 2008a, Journal of Physical and Chemical Reference Data, 37, 267, doi: 10.1063/1.2735328

—. 2008b, Journal of Physical and Chemical Reference Data, 37, 709, doi: 10.1063/1.2734564

—. 2008c, Journal of Physical and Chemical Reference Data, 37, 1285, doi: 10.1063/1.2734566

Kennicutt, Robert C., J. 1998, ApJ, 498, 541, doi: 10.1086/305588

Kilic, M., Bergeron, P., Dame, K., et al. 2019, MNRAS, 482, 965, doi: 10.1093/mnras/sty2755

Kilic, M., Munn, J. A., Harris, H. C., et al. 2017, ApJ, 837, 162, doi: 10.3847/1538-4357/aa62a5

Kim, Y. K., Lee, Y. S., & Beers, T. C. 2019, ApJ, 882, 176, doi: 10.3847/1538-4357/ab3660

Kirby, E. N., Cohen, J. G., Guhathakurta, P., et al. 2013, ApJ, 779, 102, doi: 10.1088/0004-637X/779/2/102

Kjeldsen, H., & Bedding, T. R. 1995, A&A, 293, 87. https://arxiv.org/abs/astro-ph/9403015

Klement, R., Rix, H.-W., Flynn, C., et al. 2009, ApJ, 698, 865, doi: 10.1088/0004-637X/698/1/865

Klessen, R. S., Glover, S. C. O., & Clark, P. C. 2012, MNRAS, 421, 3217, doi: 10.1111/j.1365-2966.2012.20544.x

Klose, J. Z., Fuhr, J. R., & Wiese, W. L. 2002, Journal of Physical and Chemical Reference Data, 31, 217, doi: 10.1063/1.1448482

Kobayashi, C., Umeda, H., Nomoto, K., Tominaga, N., & Ohkubo, T. 2006, ApJ, 653, 1145, doi: 10.1086/508914

Koch, D. G., Borucki, W. J., Basri, G., et al. 2010, ApJ, 713, L79, doi: 10.1088/2041-8205/713/2/L79

Kock, M., & Richter, J. 1968, ZAp, 69, 180

Koppelman, H., Helmi, A., & Veljanoski, J. 2018, ApJ, 860, L11, doi: 10.3847/2041-8213/aac882

Koppelman, H. H., Helmi, A., Massari, D., Price-Whelan, A. M., & Starkenburg, T. K. 2019a, arXiv e-prints, arXiv:1909.08924. https://arxiv.org/abs/1909.08924

Koppelman, H. H., Helmi, A., Massari, D., Roelenga, S., & Bastian, U. 2019b, A&A, 625, A5, doi: 10.1051/0004-6361/201834769

Kormendy, J., & Kennicutt, Robert C., J. 2004, ARA&A, 42, 603, doi: 10.1146/annurev.astro.42.053102.134024

Krauss, L. M., & Chaboyer, B. 2003, Science, 299, 65, doi: 10.1126/science.1075631

Kruijssen, J. M. D., Pfeffer, J. L., Reina-Campos, M., Crain, R. A., & Bastian, N. 2018, MNRAS, doi: 10.1093/mnras/sty1609

Kunth, D. 1981, in Cosmology and Particles - 16TH Moriond, ed. J. Audouze, P. Crane, T. Gaisser, D. Hegyi, & J. Tran Thanh Van, 241–251

Kusakabe, M., & Kawasaki, M. 2019, ApJ, 876, L30, doi: 10.3847/2041-8213/ab1a38

Laporte, C. F. P., Johnston, K. V., Gómez, F. A., Garavito-Camargo, N., & Besla, G. 2018, MNRAS, 481, 286, doi: 10.1093/mnras/sty1574

Lawler, J. E., Bonvallet, G., & Sneden, C. 2001a, ApJ, 556, 452, doi: 10.1086/321549

Lawler, J. E., & Dakin, J. T. 1989, Journal of the Optical Society of America B Optical Physics, 6, 1457, doi: 10.1364/JOSAB.6.001457

Lawler, J. E., Guzman, A., Wood, M. P., Sneden, C., & Cowan, J. J. 2013, ApJS, 205, 11, doi: 10.1088/0067-0049/205/2/11

Lawler, J. E., Sneden, C., & Cowan, J. J. 2015, ApJS, 220, 13, doi: 10.1088/0067-0049/220/1/13

Lawler, J. E., Sneden, C., Cowan, J. J., Ivans, I. I., & Den Hartog, E. A. 2009, ApJS, 182, 51, doi: 10.1088/0067-0049/182/1/51

Lawler, J. E., Sneden, C., Nave, G., et al. 2017, ApJS, 228, 10, doi: 10.3847/1538-4365/228/1/10

Lawler, J. E., Wickliffe, M. E., den Hartog, E. A., & Sneden, C. 2001b, ApJ, 563, 1075, doi: 10.1086/323407

Lawler, J. E., Wood, M. P., Den Hartog, E. A., et al. 2014, ApJS, 215, 20, doi: 10.1088/0067-0049/215/2/20

Lemaître, G. 1927, Annales de la Société Scientifique de Bruxelles, 47, 49

—. 1931, Nature, 127, 706, doi: 10.1038/127706b0

Letarte, B., Hill, V., Tolstoy, E., et al. 2010, A&A, 523, A17, doi: 10.1051/0004-6361/200913413

Li, T. S., Sheffield, A. A., Johnston, K. V., et al. 2017, ApJ, 844, 74, doi: 10.3847/1538-4357/aa7a0d

Lin, J., Dotter, A., Ting, Y.-S., & Asplund, M. 2018, MNRAS, 477, 2966, doi: 10.1093/mnras/sty709

Lind, K., Asplund, M., Barklem, P. S., & Belyaev, A. K. 2011, A&A, 528, A103, doi: 10.1051/0004-6361/201016095

Lindegren, L., Hernandez, J., Bombrun, A., et al. 2018, ArXiv e-prints, 616, A2, doi: 10.1051/0004-6361/201832727

Liu, L., Gerke, B. F., Wechsler, R. H., Behroozi, P. S., & Busha, M. T. 2011, ApJ, 733, 62, doi: 10.1088/0004-637X/733/1/62

Lotz, J. M., Jonsson, P., Cox, T. J., et al. 2011, ApJ, 742, 103, doi: 10.1088/0004-637X/742/2/103

Luck, R. E. 1994, ApJS, 91, 309, doi: 10.1086/191940

Luo, Y., Kajino, T., Kusakabe, M., & Mathews, G. J. 2019, ApJ, 872, 172, doi: 10.3847/1538-4357/ab0088

Mackereth, J. T., Schiavon, R. P., Pfeffer, J., et al. 2018, ArXiv e-prints. https://arxiv.org/abs/1808.00968

—. 2019, MNRAS, 482, 3426, doi: 10.1093/mnras/sty2955

Maeder, A., Meynet, G., & Chiappini, C. 2015, A&A, 576, A56, doi: 10.1051/0004-6361/201424153

Magg, M., Klessen, R. S., Glover, S. C. O., & Li, H. 2019, MNRAS, 487, 486, doi: 10.1093/mnras/stz1210

Majewski, S. R., Schiavon, R. P., Frinchaboy, P. M., et al. 2017, AJ, 154, 94, doi: 10.3847/1538-3881/aa784d

Martell, S. L., Sharma, S., Buder, S., et al. 2017, MNRAS, 465, 3203, doi: 10.1093/mnras/stw2835

Martig, M., Rix, H.-W., Aguirre, V. S., et al. 2015, MNRAS, 451, 2230, doi: 10.1093/mnras/stv1071

Martig, M., Fouesneau, M., Rix, H.-W., et al. 2016, MNRAS, 456, 3655, doi: 10.1093/mnras/stv2830

Mathur, S., García, R. A., Huber, D., et al. 2016, ApJ, 827, 50, doi: 10.3847/0004-637X/827/1/50

Matsuno, T., Aoki, W., Beers, T. C., Lee, Y. S., & Honda, S. 2017a, AJ, 154, 52, doi: 10.3847/1538-3881/aa7a08

Matsuno, T., Aoki, W., & Suda, T. 2019, ApJ, 874, L35, doi: 10.3847/2041-8213/ab0ec0

Matsuno, T., Aoki, W., Suda, T., & Li, H. 2017b, PASJ, 69, 24, doi: 10.1093/pasj/psw129

Matsuno, T., Yong, D., Aoki, W., & Ishigaki, M. N. 2018, ApJ, 860, 49, doi: 10.3847/1538-4357/aac019

Mckinney, W. 2010

McMillan, P. J. 2017, MNRAS, 465, 76, doi: 10.1093/mnras/stw2759

McWilliam, A. 1998, AJ, 115, 1640, doi: 10.1086/300289

Meléndez, J., & Barbuy, B. 2009, A&A, 497, 611, doi: 10.1051/0004-6361/200811508

Meléndez, J., Casagrande, L., Ramírez, I., Asplund, M., & Schuster, W. J. 2010, A&A, 515, L3, doi: 10.1051/0004-6361/200913047

Michaud, G., Fontaine, G., & Beaudet, G. 1984, ApJ, 282, 206, doi: 10.1086/162193

Miglio, A., Chaplin, W. J., Brogaard, K., et al. 2016, MNRAS, 461, 760, doi: 10.1093/mnras/stw1555

Mihos, J. C., & Hernquist, L. 1996, ApJ, 464, 641, doi: 10.1086/177353

Momany, Y., Zaggia, S. R., Bonifacio, P., et al. 2004, A&A, 421, L29, doi: 10.1051/0004-6361:20040183

Monty, S., Venn, K. A., Lane, J. M. M., Lokhorst, D., & Yong, D. 2019, arXiv e-prints, arXiv:1909.11969. https://arxiv.org/abs/1909.11969

Myeong, G. C., Evans, N. W., Belokurov, V., Amorisco, N. C., & Koposov, S. E. 2018a, MNRAS, 475, 1537, doi: 10.1093/mnras/stx3262

Myeong, G. C., Evans, N. W., Belokurov, V., Sanders, J. L., & Koposov, S. E. 2018b, ApJ, 856, L26, doi: 10.3847/2041-8213/aab613

—. 2018c, ArXiv e-prints. https://arxiv.org/abs/1805.00453

—. 2018d, MNRAS, 478, 5449, doi: 10.1093/mnras/sty1403

Myeong, G. C., Vasiliev, E., Iorio, G., Evans, N. W., & Belokurov, V. 2019, MNRAS, 488, 1235, doi: 10.1093/mnras/stz1770

Nair, P. B., & Abraham, R. G. 2010, ApJ, 714, L260, doi: 10.1088/2041-8205/714/2/L260

Nandy, D. K., Singh, Y., Shah, B. P., & Sahoo, B. K. 2012, Phys. Rev. A, 86, 052517, doi: 10.1103/PhysRevA.86.052517

Ness, M., Hogg, D. W., Rix, H.-W., Ho, A. Y. Q., & Zasowski, G. 2015, ApJ, 808, 16, doi: 10.1088/0004-637X/808/1/16

Ness, M., Hogg, D. W., Rix, H. W., et al. 2016, ApJ, 823, 114, doi: 10.3847/0004-637X/823/2/114

Ness, M., Freeman, K., Athanassoula, E., et al. 2013, MNRAS, 432, 2092, doi: 10.1093/mnras/stt533

Nishimura, N., Sawai, H., Takiwaki, T., Yamada, S., & Thielemann, F. K. 2017, ApJ, 836, L21, doi: 10.3847/2041-8213/aa5dee

Nissen, P. E. 2016, A&A, 593, A65, doi: 10.1051/0004-6361/201628888

Nissen, P. E., Chen, Y. Q., Carigi, L., Schuster, W. J., & Zhao, G. 2014, A&A, 568, A25, doi: 10.1051/0004-6361/201424184

Nissen, P. E., & Schuster, W. J. 2010, A&A, 511, L10, doi: 10.1051/0004-6361/200913877

—. 2011, A&A, 530, A15, doi: 10.1051/0004-6361/201116619

Noguchi, K., Aoki, W., Kawanomoto, S., et al. 2002, PASJ, 54, 855, doi: 10.1093/pasj/54.6.855

Noguchi, M. 1988, A&A, 203, 259

—. 2018, Nature, 559, 585, doi: 10.1038/s41586-018-0329-2

Nomoto, K., Kobayashi, C., & Tominaga, N. 2013, ARA&A, 51, 457, doi: 10.1146/annurev-astro-082812-140956

Norris, J. E., & Da Costa, G. S. 1995, ApJ, 447, 680, doi: 10.1086/175909

O'Brian, T. R., Wickliffe, M. E., Lawler, J. E., Whaling, W., & Brault, J. W. 1991, Journal of the Optical Society of America B Optical Physics, 8, 1185, doi: 10.1364/JOSAB.8.001185

Olive, K. A., & Skillman, E. D. 2004, ApJ, 617, 29, doi: 10.1086/425170

Paxton, B., Bildsten, L., Dotter, A., et al. 2011, ApJS, 192, 3, doi: 10.1088/0067-0049/192/1/3

Pehlivan Rhodin, A., Hartman, H., Nilsson, H., & Jönsson, P. 2017, A&A, 598, A102, doi: 10.1051/0004-6361/201629849

Peimbert, A., Peimbert, M., & Luridiana, V. 2016, Rev. Mexicana Astron. Astrofis., 52, 419. https://arxiv.org/abs/1608.02062

Peimbert, M., Luridiana, V., & Peimbert, A. 2007, ApJ, 666, 636, doi: 10.1086/520571

Peimbert, M., & Torres-Peimbert, S. 1974, ApJ, 193, 327, doi: 10.1086/153166

Pereira, C. B., Holanda, N., Drake, N. A., & Roig, F. 2019, AJ, 157, 70, doi: 10.3847/1538-3881/aaf71e

Perryman, M. A. C., Lindegren, L., Kovalevsky, J., et al. 1997, A&A, 500, 501

Piau, L., Beers, T. C., Balsara, D. S., et al. 2006, ApJ, 653, 300, doi: 10.1086/508445

Pignatari, M., Gallino, R., Heil, M., et al. 2010, ApJ, 710, 1557, doi: 10.1088/0004-637X/710/2/1557

Pinsonneault, M. H., Elsworth, Y., Epstein, C., et al. 2014, ApJS, 215, 19, doi: 10.1088/0067-0049/215/2/19

Pinsonneault, M. H., Elsworth, Y. P., Tayar, J., et al. 2018, ApJS, 239, 32, doi: 10.3847/1538-4365/aaebfd

Planck Collaboration, Adam, R., Ade, P. A. R., et al. 2016, A&A, 594, A1, doi: 10.1051/0004-6361/201527101

Plez, B. 2012, Turbospectrum: Code for spectral synthesis. http://ascl.net/1205.004

Prantzos, N., Abia, C., Cristallo, S., Limongi, M., & Chieffi, A. 2019, MNRAS, 2748, doi: 10.1093/mnras/stz3154

Prantzos, N., Hashimoto, M., & Nomoto, K. 1990, A&A, 234, 211

Press, W. H., Flannery, B. P., Teukolsky, S. A., & Vetterling, W. T. 1992, Numerical Recipes in Fortran 77: The Art of Scientific Computing, 2nd edn. (Cambridge University Press)

Preston, G. W., Shectman, S. A., & Beers, T. C. 1991, ApJ, 375, 121, doi: 10.1086/170175

Qu, Y., Di Matteo, P., Lehnert, M. D., & van Driel, W. 2011, A&A, 530, A10, doi: 10.1051/0004-6361/201015224

Ramírez, I., Meléndez, J., Bean, J., et al. 2014, A&A, 572, A48, doi: 10.1051/0004-6361/201424244

Reggiani, H., Meléndez, J., Kobayashi, C., Karakas, A., & Placco, V. 2017, A&A, 608, A46, doi: 10.1051/0004-6361/201730750

Reid, M. J., & Brunthaler, A. 2004, ApJ, 616, 872, doi: 10.1086/424960

Richard, O., Michaud, G., & Richer, J. 2005, ApJ, 619, 538, doi: 10.1086/426470

Riemer-Sørensen, S., Kotuš, S., Webb, J. K., et al. 2017, MNRAS, 468, 3239, doi: 10.1093/mnras/stx681

Riemer-Sørensen, S., Webb, J. K., Crighton, N., et al. 2015, MNRAS, 447, 2925, doi: 10.1093/mnras/stu2599

Robin, A. C., Reylé, C., Derrière, S., & Picaud, S. 2003, A&A, 409, 523, doi: 10.1051/0004-6361:20031117

Rodrigues, T. S., Bossini, D., Miglio, A., et al. 2017, MNRAS, 467, 1433, doi: 10.1093/mnras/stx120

Rodriguez-Gomez, V., Pillepich, A., Sales, L. V., et al. 2016, MNRAS, 458, 2371, doi: 10.1093/mnras/stw456

Roederer, I. U., Hattori, K., & Valluri, M. 2018, AJ, 156, 179, doi: 10.3847/1538-3881/aadd9c

Roederer, I. U., Sneden, C., Thompson, I. B., Preston, G. W., & Shectman, S. A. 2010, ApJ, 711, 573, doi: 10.1088/0004-637X/711/2/573

Romano, D., & Matteucci, F. 2007, MNRAS, 378, L59, doi: 10.1111/j.1745-3933.2007.00320.x

Rosman, K. J. R., & Taylor, P. D. P. 1998, Journal of Physical and Chemical Reference Data, 27, 1275, doi: 10.1063/1.556031

Ruffoni, M. P., Den Hartog, E. A., Lawler, J. E., et al. 2014, MNRAS, 441, 3127, doi: 10.1093/mnras/stu780

Ryan, S. G., Norris, J. E., & Beers, T. C. 1999, ApJ, 523, 654, doi: 10.1086/307769

Salaris, M., Serenelli, A., Weiss, A., & Miller Bertolami, M. 2009, ApJ, 692, 1013, doi: 10.1088/0004-637X/692/2/1013

Sanders, J. L., & Binney, J. 2016, MNRAS, 457, 2107, doi: 10.1093/mnras/stw106

Santucci, R. M., Beers, T. C., Placco, V. M., et al. 2015, ApJ, 813, L16, doi: 10.1088/2041-8205/813/1/L16

Schmidt, M. 1959, ApJ, 129, 243, doi: 10.1086/146614

Schneider, R., Omukai, K., Bianchi, S., & Valiante, R. 2012a, MNRAS, 419, 1566, doi: 10.1111/j.1365-2966.2011.19818.x

Schneider, R., Omukai, K., Limongi, M., et al. 2012b, MNRAS, 423, L60, doi: 10.1111/j.1745-3933.2012.01257.x

Schönrich, R., Binney, J., & Dehnen, W. 2010, MNRAS, 403, 1829, doi: 10.1111/j.1365-2966.2010.16253.x

Schramm, D. N., & Turner, M. S. 1998, Reviews of Modern Physics, 70, 303, doi: 10.1103/RevModPhys.70.303

Schuster, W. J., Moreno, E., Nissen, P. E., & Pichardo, B. 2012, A&A, 538, A21, doi: 10.1051/0004-6361/201118035

Sestito, F., Longeard, N., Martin, N. F., et al. 2019, MNRAS, 484, 2166, doi: 10.1093/mnras/stz043

Sharma, S., Stello, D., Bland-Hawthorn, J., Huber, D., & Bedding, T. R. 2016, ApJ, 822, 15, doi: 10.3847/0004-637X/822/1/15

Sheffield, A. A., Price-Whelan, A. M., Tzanidakis, A., et al. 2018, ApJ, 854, 47, doi: 10.3847/1538-4357/aaa4b6

Sheth, K., Elmegreen, D. M., Elmegreen, B. G., et al. 2008, ApJ, 675, 1141, doi: 10.1086/524980

Shi, J. R., Gehren, T., Mashonkina, L., & Zhao, G. 2009, A&A, 503, 533, doi: 10.1051/0004-6361/200912073

Silva Aguirre, V., Bojsen-Hansen, M., Slumstrup, D., et al. 2018, MNRAS, 475, 5487, doi: 10.1093/mnras/sty150

Simpson, J. D. 2019, MNRAS, 488, 253, doi: 10.1093/mnras/stz1699

Skrutskie, M. F., Cutri, R. M., Stiening, R., et al. 2006, AJ, 131, 1163, doi: 10.1086/498708

Slipher, V. M. 1917, The Observatory, 40, 304

Smiljanic, R., Romano, D., Bragaglia, A., et al. 2016, A&A, 589, A115, doi: 10.1051/0004-6361/201528014

Smith, G. 1988, Journal of Physics B Atomic Molecular Physics, 21, 2827, doi: 10.1088/0953-4075/21/16/008

Smith, G., & Raggett, D. S. J. 1981, Journal of Physics B Atomic Molecular Physics, 14, 4015, doi: 10.1088/0022-3700/14/21/016

Smith, M. C., Evans, N. W., Belokurov, V., et al. 2009, MNRAS, 399, 1223, doi: 10.1111/j.1365-2966.2009.15391.x

Sneden, C. 1973, ApJ, 184, 839, doi: 10.1086/152374

Sneden, C., Cowan, J. J., & Gallino, R. 2008, ARA&A, 46, 241, doi: 10.1146/annurev.astro.46.060407.145207

Sneden, C., Preston, G. W., McWilliam, A., & Searle, L. 1994, ApJ, 431, L27, doi: 10.1086/187464

Sobeck, J. S., Lawler, J. E., & Sneden, C. 2007, ApJ, 667, 1267, doi: 10.1086/519987

Soderblom, D. R. 2010, ARA&A, 48, 581, doi: 10.1146/annurev-astro-081309-130806

Spergel, D. N., Verde, L., Peiris, H. V., et al. 2003, ApJS, 148, 175, doi: 10.1086/377226

Spina, L., Meléndez, J., Karakas, A. I., et al. 2018a, MNRAS, 474, 2580, doi: 10.1093/mnras/stx2938

—. 2018b, MNRAS, 474, 2580, doi: 10.1093/mnras/stx2938

Spite, F., & Spite, M. 1982a, A&A, 115, 357

Spite, M., & Spite, F. 1982b, Nature, 297, 483, doi: 10.1038/297483a0

Stacy, A., & Bromm, V. 2013, MNRAS, 433, 1094, doi: 10.1093/mnras/stt789

Stacy, A., Bromm, V., & Lee, A. T. 2016, MNRAS, 462, 1307, doi: 10.1093/mnras/stw1728

Stacy, A., Bromm, V., & Loeb, A. 2011, MNRAS, 413, 543, doi: 10.1111/j.1365-2966.2010.18152.x

Stacy, A., Greif, T. H., Klessen, R. S., Bromm, V., & Loeb, A. 2013, MNRAS, 431, 1470, doi: 10.1093/mnras/stt264

Stello, D., Huber, D., Bedding, T. R., et al. 2013, ApJ, 765, L41, doi: 10.1088/2041-8205/765/2/L41

Stephens, A., & Boesgaard, A. M. 2002, AJ, 123, 1647, doi: 10.1086/338898

Stewart, K. R., Bullock, J. S., Wechsler, R. H., Maller, A. H., & Zentner, A. R. 2008, ApJ, 683, 597, doi: 10.1086/588579

Straniero, O., Cristallo, S., & Piersanti, L. 2014, ApJ, 785, 77, doi: 10.1088/0004-637X/785/1/77

Suda, T., Yamada, S., Katsuta, Y., et al. 2011, MNRAS, 412, 843, doi: 10.1111/j.1365-2966.2011.17943.x

Suda, T., Katsuta, Y., Yamada, S., et al. 2008, PASJ, 60, 1159, doi: 10.1093/pasj/60.5.1159

Suda, T., Hidaka, J., Aoki, W., et al. 2017, PASJ, 69, 76, doi: 10.1093/pasj/psx059

Susa, H. 2019, ApJ, 877, 99, doi: 10.3847/1538-4357/ab1b6f

Susa, H., Hasegawa, K., & Tominaga, N. 2014, ApJ, 792, 32, doi: 10.1088/0004-637X/792/1/32

Tajitsu, A., Aoki, W., & Yamamuro, T. 2012, PASJ, 64, 77, doi: 10.1093/pasj/64.4.77

Takahashi, K., Umeda, H., & Yoshida, T. 2014, ApJ, 794, 40, doi: 10.1088/0004-637X/794/1/40

Takeda, Y. 2019, A&A, 622, A107, doi: 10.1051/0004-6361/201834857

Takeda, Y., & Tajitsu, A. 2017, PASJ, 69, 74, doi: 10.1093/pasj/psx057

Ting, Y.-S., Conroy, C., Rix, H.-W., & Cargile, P. 2019, ApJ, 879, 69, doi: 10.3847/1538-4357/ab2331

Tominaga, N., Iwamoto, N., & Nomoto, K. 2014, ApJ, 785, 98, doi: 10.1088/0004-637X/785/2/98

Toomre, A., & Toomre, J. 1972, ApJ, 178, 623, doi: 10.1086/151823

Tsujimoto, T., Matsuno, T., Aoki, W., Ishigaki, M. N., & Shigeyama, T. 2017, ApJ, 850, L12, doi: 10.3847/2041-8213/aa9886

Tsujimoto, T., Nomoto, K., Yoshii, Y., et al. 1995, MNRAS, 277, 945, doi: 10.1093/mnras/277.3.945

Tucci Maia, M., Ramírez, I., Meléndez, J., et al. 2016, A&A, 590, A32, doi: 10.1051/0004-6361/201527848

Turk, M. J., Abel, T., & O'Shea, B. 2009, Science, 325, 601, doi: 10.1126/science.1173540

Ulrich, R. K. 1986, ApJ, 306, L37, doi: 10.1086/184700

Umeda, H., & Nomoto, K. 2003, Nature, 422, 871, doi: 10.1038/nature01571

Valenti, J. A., & Piskunov, N. 1996, A&AS, 118, 595

Valentini, M., Chiappini, C., Bossini, D., et al. 2019, A&A, 627, A173, doi: 10.1051/0004-6361/201834081

Valerdi, M., Peimbert, A., Peimbert, M., & Sixtos, A. 2019, ApJ, 876, 98, doi: 10.3847/1538-4357/ab14e4

van den Bosch, F. C. 2002, MNRAS, 331, 98, doi: 10.1046/j.1365-8711.2002.05171.x

van der Walt, S., Colbert, S. C., & Varoquaux, G. 2011, Computing in Science & Engineering, 13, 22, doi: 10.1109/MCSE.2011.37

van Leeuwen, F. 2007, A&A, 474, 653, doi: 10.1051/0004-6361:20078357

Vasiliev, E. 2019, MNRAS, 482, 1525, doi: 10.1093/mnras/sty2672

Venn, K. A., Irwin, M., Shetrone, M. D., et al. 2004, AJ, 128, 1177, doi: 10.1086/422734

Villalobos, Á., & Helmi, A. 2008, MNRAS, 391, 1806, doi: 10.1111/j.1365-2966.2008.13979.x

Vogt, S. S., Allen, S. L., Bigelow, B. C., et al. 1994, in Proc. SPIE, Vol. 2198, Instrumentation in Astronomy VIII, ed. D. L. Crawford & E. R. Craine, 362, doi: 10.1117/12.176725

Wagoner, R. V., Fowler, W. A., & Hoyle, F. 1967, ApJ, 148, 3, doi: 10.1086/149126

Wanajo, S., Sekiguchi, Y., Nishimura, N., et al. 2014a, ApJ, 789, L39, doi: 10.1088/2041-8205/789/2/L39

—. 2014b, ApJ, 789, L39, doi: 10.1088/2041-8205/789/2/L39

Wetzel, A. R., Tollerud, E. J., & Weisz, D. R. 2015, ApJ, 808, L27, doi: 10.1088/2041-8205/808/1/L27

Winget, D. E., & Kepler, S. O. 2008, ARA&A, 46, 157, doi: 10.1146/annurev.astro.46.060407.145250

Wood, M. P., Lawler, J. E., Sneden, C., & Cowan, J. J. 2013, ApJS, 208, 27, doi: 10.1088/0067-0049/208/2/27

—. 2014, ApJS, 211, 20, doi: 10.1088/0067-0049/211/2/20

Yamada, S., Suda, T., Komiya, Y., Aoki, W., & Fujimoto, M. Y. 2013, MNRAS, 436, 1362, doi: 10.1093/mnras/stt1652

Yong, D., Casagrande, L., Venn, K. A., et al. 2016, MNRAS, 459, 487, doi: 10.1093/mnras/stw676

York, D. G., Adelman, J., Anderson, Jr., J. E., et al. 2000, AJ, 120, 1579, doi: 10.1086/301513

Yu, J., Huber, D., Bedding, T. R., et al. 2018, ApJS, 236, 42, doi: 10.3847/1538-4365/aaaf74

Yuan, Z., Myeong, G. C., Beers, T. C., et al. 2019, arXiv e-prints, arXiv:1910.07538. https://arxiv.org/abs/1910.07538

Zavarygin, E. O., Webb, J. K., Dumont, V., & Riemer-Sørensen, S. 2018, MNRAS, 477, 5536, doi: 10.1093/mnras/sty1003

Zhang, L., Karlsson, T., Christlieb, N., et al. 2011, A&A, 528, A92, doi: 10.1051/0004-6361/201015226

Zinn, J. C., Pinsonneault, M. H., Huber, D., & Stello, D. 2019, ApJ, 878, 136, doi: 10.3847/1538-4357/ab1f66

Zong, W., Fu, J.-N., De Cat, P., et al. 2018, ApJS, 238, 30, doi: 10.3847/1538-4365/aadf81

Appendix A

Nucleosynthesis processes

A.1 Big Bang

The Big Bang nucleosynthesis determines the initial composition of the Universe as discussed in Section 1.1.1.

The standard Big Bang model with the latest cosmological parameters (Planck Collaboration et al., 2016) predict the primordial abundance (Cyburt et al., 2016) as shown in Table A.1. Table A.1 also provides results of observations (Cyburt et al., 2016).

Table A.1 The initial composition of the Universe (Cyburt et al., 2016)

Element	$N_{\rm D}/N_{\rm H}$	Y_p	$N_{^7{\rm Li}}/N_{\rm H}$
Prediction	2.579×10^{-5}	0.2470	4.648×10^{-10}
Observations	$(2.53 \pm 0.04) \times 10^{-5}$	0.2449 ± 0.0040	$(1.6 \pm 0.3) \times 10^{-10}$

Abundance measurements for these elements test the standard Big Bang nucleosynthesis. ^{7}Li is the only element whose abundance can be measured for stars, although D and ^{4}He abundances can be measured from high-redshift damped Lyman alpha systems and metal-poor galaxies, respectively. While D and ^{4}He show good agreements with the standard Big Bang nucleosynthesis, there remains significant discrepancy in ^{7}Li abundance (known as ^{7}Li problem). Metal-poor turn-off stars show ^{7}Li abundance of $A({\rm Li}) \sim 2.2$ on average (Charbonnel & Primas, 2005), which is ~ 0.5 dex lower than the value predicted by SBBN. Moreover, as we go toward lower metallicity, the average Li abundance seems to decrease, whereas we expect the Li abundance should be closer to the SBBN value at lower metallicity. However, these Li problems do not necessarily contradict with SBBN models because of the fragility of Li. Several models invoke Li depletion mechanisms that might operate between the Big Bang and the time of observation of metal-poor stars, i.e., current Universe. These models include atomic diffusion in stars (e.g., Michaud et al., 1984; Richard et al., 2005) and complete

destruction of ^{7}Li during pre-main sequence phase (e.g., Fu et al., 2015) (Li-destruction in the stars we observe now); chemical separation during the hierarchical structure formation by magnetic field (Kusakabe & Kawasaki, 2019) and Li-depletion due to first stars (Piau et al., 2006) (Li-destruction prior to the formation of the stars). Others also pointed out line-weakening due to the chromospheric activity (Takeda, 2019) as a possible source of systematic uncertainties in abundance measurements. There are, of course, attempts to modify the primordial Li abundance assuming non-standard cosmology such as Luo et al. (2019). There has been no robust conclusion, and we need better understandings of stellar evolution and star formation in order to conclude whether SBBN fit with observations.

A.2 Type II supernovae: explosion of massive stars

Massive stars are important source of elements from C to iron-peak elements. Starting from proton burning, which synthesize ^{4}He from H, heavier elements are successively synthesized in massive stars. Atoms having the same even number of proton and neutron, are called α-elements and synthesized through α captures. When massive stars end their lives with the explosion, large amounts of iron-peak elements are also synthesized. At the time of the explosion, most of the synthesized material come out of the star for the first time and are returned to the interstellar space. These explosions are often observed as type II supernovae from the Earth.

The abundance ratio of the ejected material depends on the property of the star and the explosion, such as mass of the star or explosion energy (Nomoto et al., 2013). Simulation of supernovae explosion requires extensive 3-dimensional calculation, and thus nucleosynthesis calculation from the first principle is still limited. Therefore, the abundance pattern of the ejected material is usually calculated by assuming additional free parameters. Predicted abundance patterns have been calculated over a wide range of parameters and used in theoretical chemical evolution models after averaged over initial mass function (e.g., Kobayashi et al., 2006). Since abundances of the type II supernovae products are easily measured in stars, these theoretical calculations have been compared with observations to test our understanding of chemical evolution and nucleosynthesis.

When the Galactic chemical evolution matters, only averaged abundance pattern is important in most cases. However, there are exceptions in which we are able to get information about individual supernovae. One of the examples is when we look at extremely low-metallicity stars, which are considered to reflect a single or a few supernova explosion(s) of first stars. Therefore, by comparing abundance pattern of those low-metallicity stars and theoretical chemical abundance pattern of supernova ejecta, the mass can be estimated for first stars (Ishigaki et al., 2018). The estimated masses

are then compared to predictions from simulation of first star formation and can be used to test our understanding of the formation of first stars. An important property of extremely metal-poor stars is that a large fraction of them shows carbon excess (Beers & Christlieb, 2005), which is considered to be related to a property of first stars. The carbon excess is usually attributed to low explosion energy or high rotation velocity, although it is still debated what aspect of first stars plays a dominant role.

A.3 Type Ia supernovae: explosion of white dwarfs

Explosions of white dwarfs produce large amount of iron-group elements (e.g., Tsujimoto et al., 1995). Even though it is still debated if the explosion involves one or two white dwarfs, low-to-intermediate stars have to die before the explosion in either case. The highest mass star that leaves a CO white dwarf is estimated to be $\sim 5.5\,\mathrm{M}_\odot$, which has a life time of $\sim 100\,\mathrm{Myr}$ (Chen et al., 2014). Therefore, type Ia supernovae start to occur after star formation with a delay time.

The large iron production and the delay time of type Ia supernovae have a significant impact on the chemical evolution of galaxies. In the early phase of the chemical evolution, the chemical composition is mostly determined by type II supernovae. Type Ia supernovae later start to contribute to the chemical evolution ejecting materials with a different abundance ratio from type II supernovae. As a result, abundance ratio in the galaxy gradually approaches type Ia supernovae value from type II supernovae value.

The abundance ratio between α-elements and Fe is usually used as a diagnostics of the type Ia supernovae contribution. While type II supernovae produce both Fe and α-elements, type Ia supernovae mostly produce iron, which leads to [α/Fe] reduction with time. Stars with a high [α/Fe] ratio are interpreted to have formed shortly after the onset of the star formation, i.e., the star is old. Correlation between stellar ages and [α/Fe] has, in fact, been observed (e.g., Bensby et al., 2014).

These properties of type Ia and II supernovae enable us to quantitatively discuss the timescale of star formation in a system with α-elements and Fe without detailed chemical evolution modelling. The onset of type Ia supernovae marks a "knee" in [α/Fe]–[Fe/H] plane and the knee metallicity is an indicator of star formation time scale. If the system experiences bursty star formation, type II supernovae would produce a large amount of metals before type Ia supernovae start to occur. Therefore, [α/Fe] is kept high even at high metallicity, which indicates the knee is located at high metallicity.

As we have discussed, α elements and Fe abundances are an important tool to study stellar ages and chemical evolution of galaxies. In addition, abundances of α-elements and Fe are easily measured from stellar spectra. These two facts lead to extensive use of its abundance ratio in the context of

the Galactic Archaeology. However, there are still dimensions where we have not explored very much. Here I will introduce a few other nucleosynthesis sites, which enables us to have additional dimensions to study the Galactic chemical evolution.

A.4 The *s*-process

Elements heavier than iron-group elements are not synthesized by supernovae; they are produced through neutron capture processes in neutron-rich environments. Asymptotic giant branch (AGB) stars provide environment where neutron capture process can proceed (Käppeler et al., 2011).

AGB stars repeatedly ignite hydrogen shell burning and helium shell burning. The region between the hydrogen burning and the helium burning shells is the place of neutron capture processes. In this region, the product of helium burning, ^{12}C, and a small amount of hydrogen co-exist, thanks to mixing inside of stars. Proton capture by the ^{12}C produces ^{13}C, which is then followed by the $^{13}\mathrm{C}(\alpha, n)^{16}\mathrm{O}$ reaction. This reaction is a main source of neutron in AGB stars. Another source of neutron is ^{22}Ne, which experiences the $^{22}\mathrm{Ne}(\alpha, n)^{25}\mathrm{Mg}$ reaction.

Although AGB stars contain enough neutrons for neutron capture processes to be activated, the neutron density achievable in AGB stars is not very high. The neutron capture process proceeds slowly and the process in AGB stars is called *s*-process. In the *s*-process, neutron captures proceed through the stable valley; if an atom has a short β-decay life time, then it experiences β decay before capturing another neutron.

AGB stars are final phase of low-to-intermediate mass stars. Therefore, their contribution to the galactic chemical evolution becomes important at later times in general. In fact, observations show that *s*-process elements show enhancements relative to α-elements at high metallicity and in younger stars (e.g., Spina et al., 2018a).

There are some metal-poor stars whose *s*-process elements are enhanced together with C abundance (so-called CEMP-*s* stars; Beers & Christlieb, 2005). Since most of these stars show radial velocity variation, these stars are considered to have been companions of more massive stars that are once AGB stars. Material processed in the more massive star and enhanced in *s*-process elements would have been transferred to the currently observed star through Roche lobe overflow or stellar wind, and then the massive star becomes a white dwarf. Abundance patterns of many of CEMP-*s* stars are well explained by theoretical *s*-process yields, supporting this idea. However this is not always the case; some stars have abundance patterns inconsistent with theoretical *s*-process calculation. Instead, abundances of these stars are described well with higher neutron density than typical *s*-process but lower than *r*-process, which will be discussed next. These stars suggest that

an "intermediate" neutron capture process seem to occur, but the site is still debated (Hampel et al., 2016).

The s-process explained above are called "main"-s. Observations of neutron capture element abundances revealed that we need additional s-process sites that only contribute to light neutron-capture elements ($Z \lesssim 38$). This process is called "weak"-s. The site is considered to be massive stars during its core He burning and shell C burning phases. The ^{22}Ne(α,n)^{25}Mg reaction is the source of neutrons in the weak s-process. Since the ^{22}Ne is produced from CNO elements through H burning and α captures to ^{14}N, the efficiency is dependent on CNO abundance(e.g., Prantzos et al., 1990). Since the site is massive stars, the expected timescale is short, which is indeed observationally supported.

A.5 The r-process

The r-process refers to a rapid neutron capture process (Cowan et al., 2019), in which subsequent neutron captures occur in a shorter time scale than β-decay time scales of atoms. The reaction goes through a region close to the neutron drip line, beyond which no bound neutrons can be added. The products then decay to stable isobars through β-decays after the reaction stops. As a result of the difference in the path between s- and r- processes, they produce elements/isotopes in different ratios. Therefore, by looking at abundance ratios of neutron capture elements in a star, we can infer the contribution of s- and r- processes in the star (e.g., Arlandini et al., 1999; Prantzos et al., 2019).

Some metal-poor stars in the Galaxy show high abundance of r-process elements (Sneden et al., 1994). Surprisingly, these stars show almost the same abundance pattern of the neutron-capture elements. This is called the universality of the r-process.

The site of r-process has long been debated. In order to capture neutrons rapidly, neutron density has to be extremely high. Such requirements are only met where neutron stars exist. Supernovae explosions were once considered to be the promising site for r-process. However, theoretical studies have shown that it is difficult for supernovae to reproduce the universal r-process abundance pattern. In addition, the large scatter in r-process abundance at low-metallicity including existence of r-process rich stars indicate that r-process nucleosynthesis is rather rare, which is incompatible with supernova explosions.

On the other hand, neutron-star mergers has gained evidence of being the main r-process in the last ten years. Theoretical calculation showed that neutron star mergers can reproduce the universality (Wanajo et al., 2014b). Strong observational support was gained by the observation of the gravitational wave event GW 170817 (Abbott et al., 2017), which is a merger of two

neutron stars. Optical-infrared follow-up observations of this event revealed there is a kilonova, which is brighter in infrared than usual supernovae. Its spectral energy distribution and the light curve are consistent with r-process rich material being ejected by the merger.

Since r-process is a rare event, and thus each event should produce a large amount of r-process elements. These properties introduce stochasticity in the chemical evolution, which are most visible in small systems, such as dwarf galaxies. Whereas almost all the ultra faint dwarf galaxies $M_\star < 10^4\,\mathrm{M}_\odot$ around the Milky Way have very low r-process element abundances, Ji et al. (2016) discovered that many stars in an ultra faint dwarf galaxy, Reticulum II (Ret II), show very high r-process abundances like r-rich stars in the Galactic halo. These results are interpreted as follows. The r-process events are so rare that the expected number of the events is less than 1 for those low-mass systems. However if one event happens, the large r-process enrichment by the single event pollute the entire galaxy and brings r-process abundances very high. Although Ji et al. (2016) is the first example in which we capture a single r-process enrichment event, Tsujimoto et al. (2017) also captures a signature of a single event in a more massive dwarf galaxy, Draco.

It is natural to consider that the large variation of r-process element abundances at low metallicity in the Galactic halo is introduced by the rarity of the r-process events. However, it is still unclear if the reason of the scatter is that the Galactic halo is made up of many building blocks with different amount of r-process abundances or that each building block already has a scatter due to inhomogeneous mixing of r-process materials with interstellar material in the galaxy. Roederer et al. (2018) provides a support for the first scenario by suggesting that a fraction of r-rich stars are kinematically associated with each other and share similar metallicity. If this is the case, r-process abundances are capable of providing a way to find stars having the same progenitor galaxy.

A.6 Red giant branch stars

Although much nucleosynthesis does not happen during the red giant branch (RGB) phase of low mass stars, understandings of the nucleosynthesis reactions and mixing in RGB stars are needed to interpret stellar chemical abundances. This is because RGB stars are so luminous that we can observe up to a large distance and hence important tracers of the chemical evolution of the entire Galaxy. While surface abundances of most of the elements are unchanged, those of some light elements are already affected by the internal nucleosynthesis. Therefore, it is not possible to retrieve the information about the Galactic chemical evolution unless we understand how the abundances of these elements are affected.

While the stellar surface preserves the chemical composition of the natal

gas from which the star was born, the interior contains processed materials. These materials are processed during the pre-main sequence phase when a convective core is large and the central temperature is high. The main reactions are the conversion of C to N and the destruction of D and Li through a proton capture. Although the processed material is kept inside of stars while the star is on the main-sequence phase with thin convective envelope, the first dredge-up brings it to the surface. That is the reason why we see a change in abundances of these elements after the first dredge up. Observationally, abundances of these elements are shown to further change along the red giant branch, suggesting the existence of extra mixing.

Although it is true that these internal processing complexes the interpretation of abundances of the light elements in red giants, they instead tell us about the property of the star itself. One of the important applications is mass estimate of red giants through the C/N ratio (Martig et al., 2016; Ness et al., 2016). As we discuss later, masses of red giants are necessary for age estimates. Therefore, measurements of C/N ratio of red giants could be a way to get stellar ages for a large number of giants.